TUNING OF MICROSTRUCTURE AND MECHANICAL PROPERTIES IN ADDITIVELY MANUFACTURED METASTABLE BETA TITANIUM ALLOYS

Mohan Sai Kiran Kumar Yadav Nartu, B. S., M.S.

Dissertation Prepared for the Degree

DOCTOR OF PHILOSOPHY

UNIVERSITY OF NORTH TEXAS

May 2022

APPROVED:

Rajarshi Banerjee, Advisor
Narendra Dahotre, Co-Advisor/Committee Member
James C. Williams, Committee Member
Srinivasan G. Srivilliputhur, Committee Member
Brandon Mc. Williams, Committee Member
Vijay Vasudevan, Chair of the Department of Materials Science and Engineering
Hanchen Huang, Dean of the College of Engineering
Victor Prybutok, Dean of the Toulouse Graduate School

Nartu, Mohan Sai Kiran Kumar Yadav. *Tuning of Microstructure and Mechanical Properties in Additively Manufactured Metastable Beta Titanium Alloys.* Doctor of Philosophy (Materials Science and Engineering), May 2022, 125 pp., 8 tables, 40 figures, 2 appendices, 224 numbered references.

The results from this study, on a few commercial and model metastable beta titanium alloys, indicate that the growth restriction factor (GRF) model fails to interpret the grain growth behavior in the additively manufactured alloys. In lieu of this, an approach based on the classical nucleation theory of solidification incorporating the freezing range has been proposed for the first time to rationalize the experimental observations. Beta titanium alloys with a larger solidification range (liquidus minus solidus temperature) exhibited a more equiaxed grain morphology, while those with smaller solidification ranges exhibited columnar grains.

Subsequently, the printability of two candidate beta titanium alloys containing eutectoid elements (Fe) that are prone to beta fleck in conventional casting, i.e., Ti-1Al-8V-5Fe (wt%) or Ti-185, and Ti-10V-2Fe-3Al (wt%) or Ti-10-2-3, is further investigated via two different AM processing routes. These alloys are used for high-strength applications in the aerospace industry, such as landing gears and fasteners. The Laser Engineered Net Shaping and Selective Laser Melting (the two AM techniques) results show that locally higher solidification rates in AM can prevent the problem of beta fleck and potentially produce β-titanium alloys with significantly enhanced mechanical properties over conventionally cast/forged counterparts. Further, the detailed investigation of microstructure-mechanical property relationships indicates that the precipitation or formation of non-equilibrium secondary phases like α or ω in these commercial systems can be advantageous to the mechanical properties. The influence of process parameters on the evolution of such secondary phases within the β matrix grains has also been rationalized using a FEM-based multi-physics thermo-kinetic model that predicts the multiple heating-cooling cycles experienced

by the layers during the LENS deposition. Overall, the results indicate that Ti-1-8-5 and Ti-10-2-3 are promising β-Ti alloys for AM processing. Further, the results also demonstrate the ability to tune the microstructure (secondary phase precipitation and grain size) via changes in the process parameters to achieve desirable mechanical properties, obviating the need for any secondary post-processing.

The understanding obtained through this work can be coupled with the concept of β-phase stability prediction, via parameters like bond order (Bo), the energy level of metal d-orbital (Md), Mo equivalency, etc., to design novel beta titanium alloys with the desired microstructures tailored via AM for structural applications.

ACKNOWLEDGMENTS

First of all, I would like to thank my advisor, Rajarshi Banerjee, for providing me with an opportunity to work with him. I strongly express my gratitude to him for giving me the freedom to pursue the topics of my interest during my Ph.D. research. His passion for research will always be an inspiration to me. I also especially thank Narendra Dahotre. I had a wonderful experience working in collaboration with him. His invaluable suggestions and comments have helped me tackle and overcome various challenges during my research.

I also thank my other committee members Srinivasan G. Srivilliputhur (Srini), Jim Williams, and Brandon McWilliams, for their insights and recommendations. I thank Rajiv Mishra for providing me access to the mechanical testing facilities, a crucial part of my dissertation. I am greatly indebted to Srini, Tom Scharf, Jim Williams, and Nigel Shepherd for teaching me the core concepts of materials science. I am thankful to Srikumar Banerjee and Hamish Fraser for stimulating discussions and invaluable help.

I extend my thanks to David Jaeger and Saul Sepulveda for their unlimited support with Materials Research Facility (MRF) instruments at UNT. I also thank Mangesh Pantawane and Shashank Sharma from the Dahotre research group at UNT, and Nevin Taylor and Brian Welck from the Fraser's research group at Ohio State University for their help with the research. At UNT, I especially thank Srinivas Aditya Mantri; he has been a great mentor, friend, and guardian to me all along.

I would like thank my brothers, Manoj and Santosh for their unconditional love and care. Last but not least, none of this would have been possible without the support of my parents. I cannot thank them enough for their constant backing and encouragement. I would like to dedicate this thesis to my parents, Purushottama Rao and Usha Rani.

TABLE OF CONTENTS

Page

LIST OF TABLES

Page

LIST OF FIGURES

Page

CHAPTER 1

INTRODUCTION

This chapter provides an outline of the overall work in this thesis.

Chapter 2 provides the background and a brief overview of relevant literature, including the current study's motivation. Additionally, each chapter also contains a section on the literature review specific to that chapter.

Chapter 3 provides the experimental procedure and techniques adopted in the current study. Additionally, each chapter also contains a section on experimental details specific to that chapter.

Chapter 4 analyzes the evolution of grain morphology and texture in a few commercial and model metastable beta titanium alloys processed using additive manufacturing. Analytical models based on the fundamentals of the solidification process, i.e., the Growth restriction factor (Q) model and the solidification range aspect from homogenous nucleation, are also discussed in this chapter to rationalize the experimental observations.

Chapter 5 discusses the additive manufacturing of Ti-1Al-8V-5Fe (all in wt%), focusing on the intra-granular α/ω precipitation and its impact on tensile properties. Additionally, the microstructure and mechanical properties from the conventionally processed counterpart, i.e., As-received + β-solutionized condition, are also presented to compare and contrast with the additively manufactured alloy.

Chapter 6 discusses the additive manufacturing of the Ti-10V-2Fe-3Al (all in wt %) alloy, emphasizing the influence of laser additive processing on the evolution of the $\beta+\omega$ and $\beta+\alpha$ microstructures and their attendant impact on deformation behavior. Secondly, an approach to recover the TRIP/TWIP effects and strain hardenability in the AM processed alloy via a β-solution treatment is also presented. Finally, the microstructure and mechanical properties of the

conventionally manufactured counterparts, i.e., As-received and As-received + β-solutionized conditions, are investigated to compare and contrast with the additively manufactured Ti-10-2-3.

Chapter 7 summarizes this work. A discussion on the future work has also been included.

CHAPTER 2

LITERATURE REVIEW

2.1 Introduction

The first part of the chapter provides a general understanding of titanium and its alloys, including certain aspects of titanium metallurgy like alloy classification, the effect of alloying addition on phase stability and possible phase transformations, etc. The second part discusses additive manufacturing techniques for titanium alloys, including the applicability and challenges.

2.2 History of Titanium

William Gregor from Cornwall, Great Britain, discovered titanium in 1791, called initially mechanite (named after the place where it was discovered). A German chemist, Klaproth, gave the name titanium (derived from Greek mythological deities, Titans), four years later to its first discovery. He independently synthesized titanium from rutile, a mineral found in Hungary. However, considerable amounts of titanium were only extracted after the invention of the Kroll process by Milhelm Justin Kroll in 1940. The original Kroll process utilized $TiCl_4$ and calcium to extract titanium. Later, a modified version was proposed during World War II replacing calcium with magnesium which is used today [1,2]. This modified version of Kroll process is shown below:

$$TiCl_4 \text{ (liquid)} + 2Mg \text{ (liquid)} \rightarrow 4Ti \text{ (solid)} + 2\ MgCl_2 \text{ (liquid)} \quad (1)$$

Titanium has two allotropes and five isotopes (Ti^{48} is the most abundant (73.8%)) and is the ninth most abundant element found on earth's crust [3,4]. However, due to the high free energy of formation, titanium has never been found in its pure state. Additionally, the extraction of titanium from its mineral ores is rather difficult and expensive compared to iron.

2.3 Physical Metallurgy

Titanium has an atomic number of 22 and a mass number of 47.867 and belongs to the Group IV transition metals (according to IUPAC nomenclature)[5]. It has an electronic configuration of $1s^2 2s^2 2p^6 3s^2 3p^6 3d^2 4s^2$, and the incomplete 3d-shell enables it to form a substitutional solid solution with most elements having a size difference of ±20%. It has a melting point of 1678 ^oC, higher than the most widely used structural metals such as aluminum, iron, and nickel. Besides, compared to these metals, it (titanium) exhibits the highest specific strength with a yield strength of 1GPa and a density of 4.5 gm/cc. It has relatively low electrical and thermal conductivity and is paramagnetic [6]. A comparison of some essential properties of a few generally used structural metals is shown in Table 2.1.

Table 2.1: Comparison of properties of commonly used structural materials

Metals	Melting Temp (^oC)	Allotropic Trans (^oC)	Crystal Structure	Room Temp E(GPa)	Yield Stress (GPa)	Density (gm/cc)	Corr Resist
Titanium	1670	882(α→β)	hcp→bcc	115	1	4.5	Very high
Iron	1538	912(α→γ)	bcc→fcc	215	1	7.9	Low
Nickel	1455	-	fcc	200	1	8.9	Medium
Aluminum	660	-	fcc	72	0.5	2.7	High

2.4 Phases

Titanium alloys can exist in different phases depending on temperature, pressure, cooling rates, and alloying elements. Depending on the thermal history, i.e., whether steady-state conditions have reached during thermal processing, these phases can be either equilibrium or non-equilibrium. While α and β phases are the two major equilibrium phases, the major non-equilibrium phases are α', α", ω, β' and the recently "discovered" O' phase. The following section provides a brief description of each of them.

2.4.1 Equilibrium Phases

2.4.1.1 Alpha (α)

Titanium exists as a hexagonal close-packed phase (hcp) in its pure form at ambient temperature and pressure conditions [7]. It exhibits the space group, $P6_3/mmc$, lattice parameters, a= 2.95Å, and c= 4.68Å. It has a c/a ratio of 1.567, which is lower than the ideal c/a ratio of 1.633 for the *hcp* systems. This deviation from ideal condition results in a change of primary slip system from traditional basal (0001) to the close-packed <11-20> direction on the prismatic plane {10-10}. The addition of alloying elements plays a significant role in the phase stability of the titanium alloys. Interstitial elements like C, O, Al, La, Ge, B, N, etc., are identified to increase the β transus stabilizing the α phase. Amongst the α stabilizers, oxygen and nitrogen form peritectic systems with titanium, while aluminum, boron, lanthanum, etc., form peritectoid systems. The effect of these α stabilizers is expressed in terms of aluminum equivalency by using the following equation[8]:

$$[Al]_{eq} = [Al] + 0.17[Zr] + 0.33[Sn] + 10[O] \quad (2)$$

The α phase can be further classified based on the morphology and size scale: (a) colony α, (b) basketweave α, (c) globular α. The colony type α phase is obtained via slow cooling while the basketweave type α phase is achieved via fast cooling. The critical difference is that the latter forms multiple variants while the former forms only a single variant. The Globular α phase doesn't form while cooling but can form when the system is thermomechanically processed. The α phase formed can also be distinguished based on the nucleation site. The alpha that nucleates at the prior beta grain boundary and grows alongside wetting the grain boundary is called grain boundary alpha[9].

In contrast, the alpha that nucleates at the grain boundary but extends into the beta grain is

intergranular alpha. The intergranular alpha is also known as Widmanstatten. Lastly, the alpha that nucleates either homogenously within the beta grains or heterogeneously at the defects such as vacancies or dislocations, or metastable phases such as omega and beta' is known as intragranular alpha. Each of the types above has a specific influence on the mechanical behavior of the alloys.

2.4.1.2 Beta (β)

Pure titanium exists as a bcc beta phase at high temperatures. As mentioned earlier, the allotropic transformation from the hcp alpha phase to the bcc beta phase occurs at 883 ^{o}C. It exhibits the space group Im-3m, the lattice parameter, a= 3.32Å, and can be envisaged by positioning two atoms at (0,0,0) and (½, ½, ½) locations in the unit cell. In contrast to the alpha phase, the beta phase is less densely packed with a packing factor of 68%, which results in a more severe vibration of atoms. Therefore the structure is stable at elevated temperatures[7].

The addition of certain alloying elements lowers the beta transus temperature of the titanium alloys and stabilizes the beta phase. Molybdenum, vanadium, niobium, iron, tantalum, chromium, nickel, etc., are currently being used as beta phase stabilizers. These transition elements, similar to titanium, have partially filled d-shells. Whether or not there is a eutectoid reaction existing at sufficient elevated temperatures, these alloying elements are further divided into beta-isomorphous (Mo, V, Nb, Ta, etc.) and beta eutectoid (Fe, Cr, Mn, etc.). Hydrogen falls under the beta eutectoid category with low eutectoid temperature and high diffusivity. Analogous to the alpha phase stability, the beta phase stability is expressed using the following equivalency equation and which is given in terms of molybdenum :

$$[Mo]_{eq} = [Mo] + [0.2]Ta + 0.28\,[Nb] + 0.4[W] + 1.25[Ni] + 1.7\,[Mn] + 0.67[V] + 1.25[Cr] + 1.7[Co] + 2.5[Fe] \quad (3)$$

There are six closest-packed {011} planes and four close-packed <111> directions in β Ti. Due to its metastability at room temperatures, measuring the room temperature elastic and shear moduli isn't easy. However, the elastic modulus can be measured as a function of composition by adding β stabilizers to retain the β phase at room temperature. The addition of β phase stabilizers lowers the elastic modulus of the titanium alloys. The {110}, {112}, and {123} planes with <111> burgers direction constitute the slip systems in β titanium, which is identical to the observed slip systems in common body-centered cubic metals. Besides, certain β titanium alloys deform via twinning. The {332}<113> and {112}<111> twin systems are most commonly observed twin systems [1,10].

2.4.2 Non-Equilibrium Phases

Non-equilibrium or metastable phases are typically formed when the time for long-range diffusion of atoms (to develop an equilibrium phase) is inadequate to reorganize themselves from one stable phase to another. Thus atoms instead rearrange themselves either by shear or shuffle leading to the formation of non-equilibrium phases. These phases are a result of a compromise between thermodynamics and the kinetics of the transformation. The following describes some of these non-equilibrium phases.

2.4.2.1 Alpha' (α') Martensite

The Ti alloys with low concentrations of beta stabilizers form the α' martensite phase upon quenching from the beta phase field. The α' martensite is an hcp phase exhibiting $P6_3/mmc$ space group. Depending upon the concentration of the solute elements, the morphology of this phase can differ from colonies to laths or lenticular or twinned structures. The transformation of the beta phase into the α' martensite starts at the α' martensite start temperature, i.e., Ms (α')), and finishes

with a 100% transformation at the α' martensite finish temperature (Mf (α')). These two lines, i.e., Ms and Mf, are typically close together in the phase diagram. The Ms temperature depends on the beta phase stability; It decreases with an increase in the beta phase stability[11–13].

2.4.2.2 Alpha" (α'') Martensite

The Ti alloys with low to medium concentrations of beta stabilizers such as Mo, Nb, Ta, and W, etc., exhibit the formation of the α'' martensite. Disparate to the α' martensite that only forms during the rapid quenching, the α'' martensite can also form due to applied external stress. Therefore, it is also termed stress-induced martensite (SIM). It exhibits an orthorhombic structure with a Cmcm space group. The α'' martensite exhibits an orthorhombic structure halfway between the hcp α and bcc β. The hexagonal structure could be visualized as a particular case of an orthorhombic structure where the a/c ratio equals $\sqrt{3}$. The addition of alloying elements increases the constraints for forming hexagonal structures, and thus, martensites with the orthorhombic structure are formed. The Ms for α'' martensite is lower than α' martensite and, therefore, is more challenging to develop during quenching. The surprising aspect is that the hardness of α'' is significantly lower than α' or even the β phase [8,14]**.**

2.4.2.3 Omega (ω)

The formation of omega phase in titanium alloys occurs under three main circumstances :

(a) At high enough concentrations of beta stabilizers, the alloy completely retains its β phase and does not form α'/α'' upon quenching from a beta phase field. However, the shear transformation leading to martensite is replaced by a shuffle reaction leading to ω phase formation. This is classified in the literature as *athermal or quenched-in ω.* It is difficult to resolve these fine-scale athermal ω precipitates using scanning electron microscope (SEM). However, they can be

detected using the selected area diffraction patterns obtained via transmission electron microscope (TEM)[15–17].

(b) When titanium alloys with a sufficient amount of beta stabilizers are subjected to an annealing heat treatment between the temperatures, 100℃ to 500℃, ω phase tends to precipitate within the beta matrix. This phase is more commonly known as *isothermal ω.* The size scale and morphology of isothermal ω are dependent on the temperature, hold time and the quench rate associated with the annealing heat treatment. It is observed that the size scale and volume fraction of isothermal ω increases with an increase in the hold time and a decrease in the quench rate. The beta stabilizers are continuously rejected into the beta matrix during the formation of isothermal ω , leading to a solid state compositional partitioning across the β/ω interface, which is not observed in the case of athermal ω [16,18,19].

(c) When certain titanium alloys are deformed at room temperature under high pressure, the ω phase forms within the beta matrix. Reports on metastable model β Ti alloys, Ti-Cr, and Ti-V, exhibited an increase in the phase fraction of ω phase upon deformation[20–22].

Table 2.2 summarizes the crystallographic information for the phases that are relevant to the present work.

Table 2.2: Crystallographic data of significant phases in titanium

Phase	Space Group	Structure	Lattice Parameters (Å)
α	$P6_3/mmc$	*hcp*	a=2.95 c=4.68
β	Im3m	*bcc*	a=3.32
ω	P6/mmm	*Hexagonal*	a=4.625 c=2.813
α"	Cmcm	*orthorhombic*	a=3.01 b=4.91 c=4.63
a’	$P6_3/mmc$	*hcp*	a=2.921 c=4.669

2.5 Classification of Titanium Alloys

Titanium alloys are broadly classified into α, α/β and β alloys based on the type and amount of alloying additions.

2.5.1 α Alloys

Pure titanium and its alloys with α stabilizers that exhibit stable hcp (α) crystal structure at room temperatures are classified as α alloys [9]. These alloys show reasonable yield strength, good toughness, and better high-temperature creep, oxidation resistance, and weldability. Besides, the absence of the ductile-brittle transformation makes them suitable for cryogenic applications. These are further classified into fully-α and near-α alloys. The commercially pure (c.p.) titanium and its alloys with Al, O, Sn, or Zr (e.g., Ti-O, Ti-5Al-2.5Sn) additions fall under the category of fully-α alloys. They exhibit a combination of equiaxed and widmanstätten α microstructure for moderate cooling rates. The higher cooling rates promote the formation of α′martensite. While the creep resistance of these alloys is superior, the yield strength and formability are inferior, which led to the development of near-α alloys[7]. The near α alloys contain small amounts (<2 wt%) of beta stabilizers like Mo, Nb, and V.etc. They also contain Si in minor quantities, mainly added to compensate for the loss of creep strength due to the small amounts of β phase. Ti-8Al-1Mo-1V, Ti- 6Al-5Zr-0.5Mo-0.25Si (IMI685), Ti-6Al-2Sn-4Zr-2Mo and Ti-11Sn-2.25Al-5Zr-1Mo-0.2Si (IMI679) are some of the commercially developed near- α alloys[13].

2.5.2 α/β Alloys

The alloys that typically exhibit dual-phase α+β microstructure upon cooling from a beta phase field are known as α/β alloys. Obtaining a single-phase β microstructure is impossible in these alloys, irrespective of the cooling rates. Various microstructures such as colony (where α

laths of single variants are formed), basketweave (where α laths of multiple variants are formed), and bimodal (where equiaxed α is formed) can be tailored in these alloys via thermomechanical processing. These alloys usually contain 4-6 wt% of beta stabilizers and possess the strength of α alloys and ductility of β alloys[23–25]. Therefore, their creep properties are in between α and β alloys. Ti-6Al-4V is the most widely used α/β alloy. This high-strength alloy is currently used for aircraft engine components like turbine blades and compressor spools. An extra-low interstitial version of the same. i.e., Ti64 ELI is used in orthopedic implants due to the low modulus and superior osseointegration characteristics. Generally, the α/β alloys are used for various armor, petrochemical, and biomedical industry applications [1].

2.5.3 β Alloys

β-Ti alloys typically contain sufficient concentrations of beta stabilizing elements like Mo, V, Cr, Fe, Mn, etc., to reduce the Ms below ambient temperature, and therefore retain their body-centered cubic (bcc, β) structure and do not form α' martensite when quenched from above the β-transus temperatures[26]. Depending on whether there is a eutectoid compound present at sufficient elevated temperatures, they are further classifications: (a) β-isomorphous alloys containing elements like Mo, V, Nb, Ta, etc. (b) β-eutectoid alloys containing elements like Fe, Cu, Cr, Mn, etc. These alloys are of widespread interest for many applications due to their lower elastic modulus, higher specific strength, enhanced fracture toughness, and augmented fatigue resistance compared to other α+β Ti alloys[27–29]. There are a number of different commercially available metastable β-Ti alloys like Ti-10V-2Fe-3Al (Ti-1023), Ti-1Al-8V-5Fe (Ti-185), Ti-13V-11C-3Mo, Ti-15Mo-3Al-3Nb-0.2Si (known as β-21S) and Ti-3Al-8V-6Cr-4Mo-4Zr (known as Beta-C). One of the main challenges in processing β-rich Ti alloys containing eutectoid

elements like Fe and Cu is the beta flecking. The segregation of the beta stabilizers (beta flecking) during the conventional processing (casting) deteriorates the mechanical properties [8,30–32]. Additive manufacturing techniques with rapid cooling rates can potentially prevent this problem [33].

2.6 Additive Manufacturing

Additive manufacturing, popularly known as 3D printing, is a technology used to manufacture parts by layer by layer deposition. It has grown and changed hugely in the past three decades since the first development of the process in 1986 [34]. The idea of AM of metals (commonly known as metal 3D printing) has been developed based on a technique where polymers are selectively melted layer by layer using a low-power laser to build a three-dimensional structure [35,36]. Though metal 3D printing techniques have made decent progress since then, issues like reproducibility of microstructure, processing conditions, development of feedstock materials, etc., have somewhat limited its applications. Understanding the various processes currently employed to 3D print metals and the associated challenges is critical for establishing AM as a successful tool in production. The first patented and copyrighted AM technique to print polymers using a powder bed feedstock is selective laser sintering (SLS). Manriquez et al. became the first to adopt the SLS technique to 3D print a metal alloy from powders in 1990 [37]. Today, the method to print metals based on a powder bed feedstock is more conveniently referred to as selective laser melting (SLM) as complete melting of the metal powders is achieved while printing. Shortly after SLS was patented, a group of researchers from MIT patented a process called ‘three-dimensional printing,’ which employs inkjet printing to deposit binder [38]. Since the word ‘3D printing’ became standard media to qualify all the various techniques under the umbrella of AM, the MIT method became popular as binder jetting.

Binder jetting can be also be used to manufacture metal parts, in addition to polymers. The directed energy deposition (DED) process is another class of printing, where the feedstock is directly deposited into the laser melt pool, unlike the SLM process. Some of the machines under this class (DED) work on the wire as feedstock, where the metal wire is constantly supplied to the melt pool. In 1995, Sandia National Laboratory developed a somewhat different way of depositing the feedstock; the metal feedstock in powders was blown into the laser melt pool [39]. This technique was commercialized and trademarked as Laser Engineered Net Shaping (LENS), a subset of DED [40]. Sheet lamination is the last major category of metal AM; metal feedstock in sheets is welded together to build a 3D part [41–43]. Several methods are employed to join the sheets together, like ultrasonic welding coupled with computer numerical control (CNC) milling, initially developed and patented by Dawn White in 1999[44].

ASTM F42 Committee defines additive manufacturing as “a process of joining materials to make objects from 3D model data, usually layer upon layer”, in contrast to subtractive manufacturing methodologies [45].

2.6.1 Classification

Many different methods are employed to manufacture metal 3D parts from various feedstock materials, like powder, sheets, or wires. Every technique, irrespective of the heating source used, must consolidate the feedstock into a solid part. This can be accomplished by either melting or solid-state joining of the feedstock. According to the ASTM F42 committee, there are seven classifications of the additive manufacturing process; out of them, four belong to metal manufacturing:

1. Powder bed fusion (PBF)
    - Selective laser melting (SLM)
    - Electron beam melting (EBM)

2. Direct energy deposition (DED)
    - Laser
        - Powder fed
        - Wire fed
    - Electron beam
        - Powder fed
        - Wire fed
3. Binder jetting
    - Infiltration
    - Consolidation
4. Sheet lamination
    - Ultrasonic additive manufacturing (UAM)

Amongst the above mentioned manufacturing techniques, the most popular ones are PBF and DED. In the powder bed fusion process (PBF), the feedstock is a static powder bed, and the primary heat sources can be either laser or electron beams. In comparison, a similar classification applies to the DED process as well. However, it is further subclassified based on the type of feedstock employed.

2.6.1.1 Powder Bed Fusion

The powder bed fusion techniques, as the name suggests, include all the processes where focused energy such as electron beam or laser beam is used to sinter or melt a layer of a powder bed selectively. Melting can be preferred over sintering for metals and alloys. The laser also melts parts of previous layers during the melting of the current layer, which improves the adhesion and overall build quality with less porosity. A schematic of the SLM process is shown in Figure 2.1 [46]. In the SLM process, the substrate provides mechanical support to the build material. It is bolted down to the piston head, which allows it to move in a negative Z direction as the part is built. The piston below the feed container moves in the positive Z direction providing excess

powders to be displaced over the substrate via recoater/rake blade as shown in the schematic. The substrate also plays a crucial role by providing a thermal path to dissipate the heat during the fabrication process. Like the DED process, the scan strategies and processing conditions such as laser power, laser scan speed, hatch spacing, and layer thickness affect the build quality and microstructure.

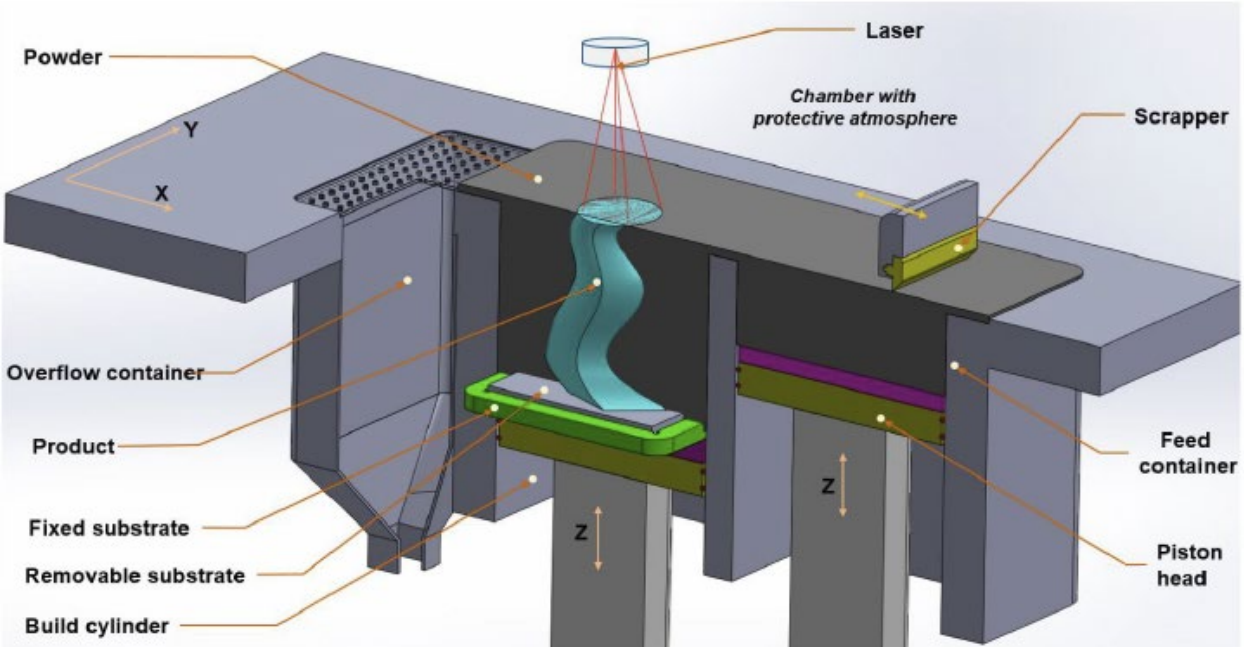

Figure 2.1: A schematic of SLM process [46]

2.6.1.2 Directed Energy Deposition

In the direct energy deposition (DED) process, as the name suggests, a feedstock of either wire or powder is deposited onto a melt pool, generated via an electron beam or a laser beam, or a plasma beam. The most commonly used DED technique is Laser Engineered Net Shaping (LENS™), the relevant equipment is manufactured, e.g., by Optomec Inc. EOS manufactures a direct metal laser sintering (DMLS) system [47]. A schematic of the LENS process is shown in Figure 2.2. The LENS process requires a powder feeder, a build platform with a substrate plate, and a system of lenses and mirrors to manipulate the laser beam. In this process, the powders are

transported by inert gases via nozzles onto the build platform. A melt pool is generated via the laser beam, and the powder flows through the nozzles, deposits on the substrate, or the previously deposited layer. This process is repeated to fabricate the final 3D components.

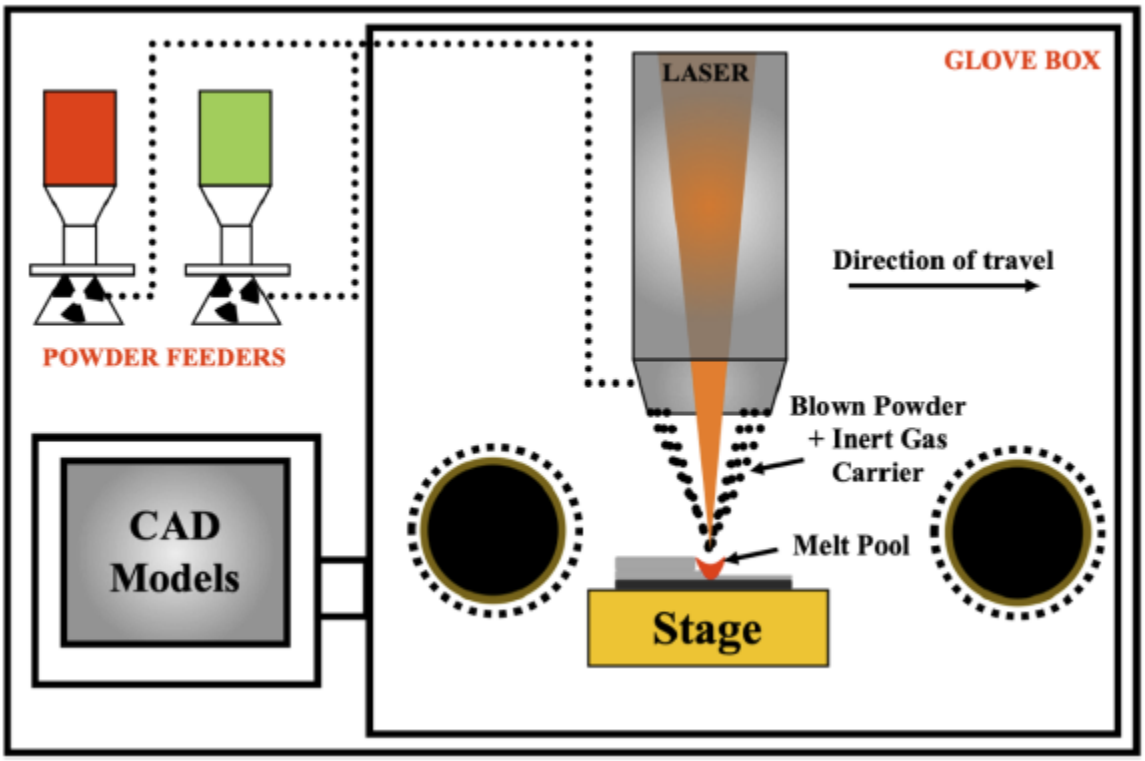

Figure 2.2: Schematic of LENS process

Besides, DEDs are also classified based on whether the deposition head moves while the workpiece is stationary or the deposition head is fixed, and the workpiece moves. This feature results in DED techniques having a significant advantage over PBF systems since they can fabricate large build volumes and refurbish damaged or worn parts[48–50]. The other primary advantage DED techniques, LENS to be specific, currently have over PBF techniques is that they can manufacture functionally/compositionally graded samples [51–57]. This is because of the ability to have two or more feeders of the feedstock material. By controlling the flow of the materials from different powder feeders at different rates, functionally/compositionally graded samples can be built.

2.6.2 Challenges Associated with Additive Manufacturing

One of the significant challenges of DED techniques is the poor surface finish. Post-processing, like filing/polishing, is required in almost all cases to enhance the surface finish before actual application. While SLM techniques can produce high-quality parts with an excellent surface finish, they are limited by the build dimensions and are significantly slower. Irrespective of the AM technique employed, the additively manufactured metal parts suffer from inherent issues like porosities, residual stresses, growth of columnar grains with significant texture along the build direction, .etc, which still need to be resolved before they can be applied on a large scale for fabrication[47,58]. Besides, the AM processed parts also exhibit inconsistent microstructures along the build direction and precipitation of non-equilibrium secondary phases that could either be advantageous or disadvantageous to the mechanical properties [59–61]. SEM images showing the lack-of-fusion pore and a gas pore are presented in Figure 2.3 [62]. A proper process parameter optimization can eliminate porosity and produce defect-free parts. However, the growth of columnar grains with significant texture along the build direction, as shown in Figure 2.4 [63], leads to anisotropy in properties, cannot be controlled entirely via process parameters, and remains an active research area.

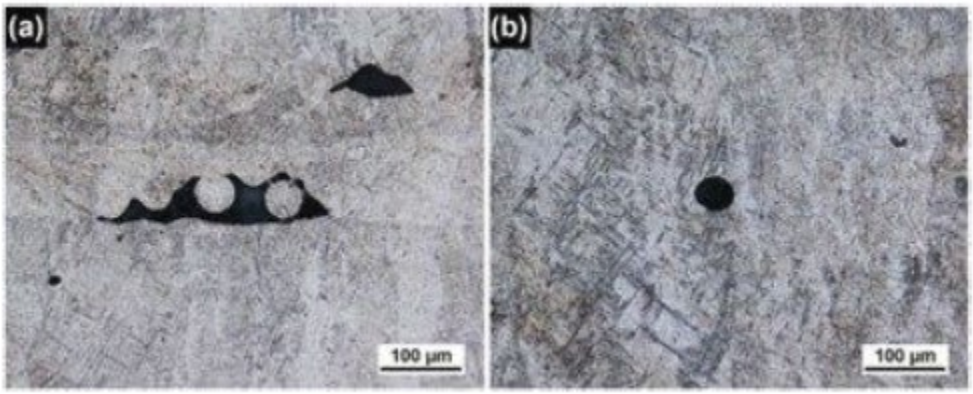

Figure 2.3: SEM images showing the two different kinds of porosity in AM parts [62]

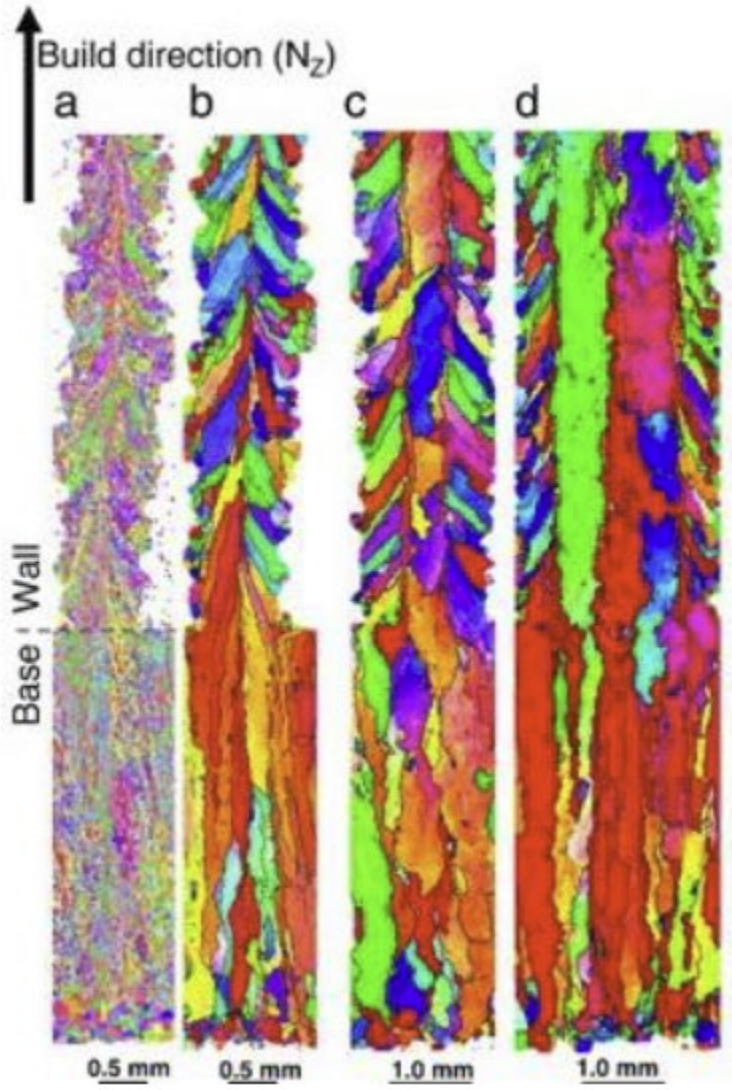

Figure 2.4: Columnar nature of beta grains in AM processed Ti-64 [63]

CHAPTER 3

EXPERIMENTAL AND PROCESSING METHODS

3.1 Introduction

This chapter briefly introduces the introduction of alloys, equipment used in the current study, and the experimental procedure followed.

3.2 Fabrication of Alloys

3.2.1 Selective Laser Melting (SLM)

A powder bed fusion (PBF) system, AconityMIDI, equipped with a 1KW laser, was used for fabricating Ti-10V-2Fe-3Al (all in wt.%). A schematic of the SLM process is shown in Figure 2.1. The scan strategy and the processing parameters employed for fabrication will be presented in the respective chapters.

3.2.2 Laser Engineered Net Shaping (LENS™)

The LENS™ 750 system by Optomec® was used to fabricate a few model (Ti-20wt%V and Ti-12wt% Mo) and commercial beta titanium alloys (TIMETAL18, TNZT, TIMETAL21S, Ti-185, Ti-1023). This is a powder feed system equipped with four powder feeders, a 1500W Yb Laser manufactured by IPG, and an Argon control system from RTI Products. The essential components of the LENS^{TM} can be seen in Figure 2.2. The specific compositions and the processing conditions used to fabricate the deposits will be presented in the respective chapters.

3.2.3 As Received Commercial Alloys

The majority of the fabrication shown in this work is performed using Optomec LENS™ 750 system. However, two commercial alloys, Ti-10V-2Fe-3Al, and Ti-1Al-8V-5Fe (all in wt.%) in forged condition have been obtained from ATI corporation for comparing the microstructures

and mechanical properties from conventional processing with the additively manufactured counterparts.

3.3 Processing Tools

This section provides a general overview of the tools used to make the samples, complete the heat treatments, and metallographic techniques for the microstructural investigation.

3.3.1 Electric Discharge Machine and Diamond Saw

The samples described in the previous section need to be of specific shape and size to perform mechanical tests or do particular heat treatments. As such, the diamond saw and an electric discharge machine (EDM) were used. A Mitsubishi FX-10 Wire EDM, KENT USA (WSI-200) EDM, and an Allied High Tech Products Inc. Techcut4TM diamond saw cut the additively and conventionally manufactured alloys into desired dimensions. The wire EDM cuts the sample by passing a high voltage through a thin brass wire that machines the piece with very low dimensional tolerances. The codes can be modified according to the final geometry that is desired. On the other hand, small coupons were cut using a low-speed diamond saw when sample size tolerances and sample geometry were not a limiting factor.

3.3.2 Heat Treatments

Heat treatments were done on select conditions to tailor specific microstructures. Further details of each heat treatment will be discussed in the respective chapters. Heat treatments were mainly done in an atmosphere of argon gas to prevent oxidation of the samples. Besides, the samples were wrapped in pure titanium foils to further minimize surface oxidation. After the aging treatment, samples were water quenched to get the required fast cooling rates: the samples were rapidly pulled out of the furnace and directly dropped into a bucket of water kept nearby.

3.3.3 Mechanical Polishing and Conventional Methods for SEM and TEM Sample Preparations

Standard metallographic techniques involving mechanical polishing using 120 to 1200 grit SiC abrasive paper were followed. The samples were then polished using 1 μm alumina solution followed by 0.05 μm colloidal silica solution on a cloth. Final polishing using 0.02 μm silica solution was carried out in Beuhler VibroMet2. After VibroMet polishing, the samples were cleaned in an ultra-sonicator using acetone to remove any debris on the surface from polishing.

3.4 Characterization Tools

Once the sample preparation was completed using the techniques above, the metallographic characterization was done using the various methods mentioned below.

3.4.1 X-Ray Diffraction

The preliminary analysis of the microstructure is performed by X-ray diffraction (XRD) using Rigaku Ultima X-ray diffractometer with 1.54 Å Cu-Kα radiation and scattering angle in the range of 20° to 90°. Additionally, synchrotron transmission X-ray diffraction experiments were performed on the 11-ID-C beam-line (105.5 keV, $\lambda = 0.1173$ Å) of the Advanced Photon Source (APS) at Argonne National laboratory (ANL) on select specimens with approximate dimensions 5 mm × 5 mm × 1 mm (thickness). A CeO_2 standard (NIST diffraction intensity standard set: 674a) was used to calibrate the distance between the sample and the 2D detector, the detector tilting angle, and the position of the beam center. The scattered radiation was collected on a Perkin Elmer 2D detector system. The 2D diffraction data were integrated and converted to an intensity vs. two-theta (2θ) plot using the program Fit-2D.

3.4.2 Scanning Electron Microscopy (SEM)

A FEI Nova NanoSEM 230 equipped with a field emission gun was used for the

microstructural analysis. The SEM is equipped with an Everhardt Thornley Secondary Electron Detector (ETD), a charged couple detector, and a detachable solid state backscattered electron detector (BSE). Furthermore, energy dispersive spectroscopy (EDS) with a SiLi detector was used to measure the chemical composition of the alloys. The SEM was also equipped with a Hikari Super Electron Backscattered Diffraction (EBSD) detector to get the orientation/crystallographic data of the samples. The sample is tilted to angle ~70^{o} before the camera is inserted to obtain the OIM^{TM} data. Data collection was done using the EDAX TEAM software, and all the analysis was performed using the TSL OIM^{TM}-8 software.

3.4.3 SEM-Focused Ion Beam (FIB)

An FEI DualBeam™ (FIB/SEM) Nova 200NanoLab with FEG source was chosen to prepare the TEM and 3-D Atom Probe specimens. The instrument has a Ga ion beam source for milling, an Omniprobe Autoprobe for the nanomanipulation, and a gas injection system (GIS) to deposit Pt. For TEM, a lift-out of dimensions ~15x2x5 mm was initially prepared with the help of the omniprobe micromanipulator in FIB. This 2 mm thick sample was subsequently thinned to dimensions ~50-100 nm in multiple steps by progressively reducing the voltage and/or current of the Ga ion beam in the dual-beam FIB. For APT, depending on the number of needles required, a lift-out of dimensions (12-20)x3x4 mm was prepared. This lift-out was then sectioned equally and deposited onto four to six Si microtips and subsequently milled to obtain conical needles with ~100 nm diameter at a depth of ~100 nm from the vertex.

3.4.4 Transmission Electron Microscopy (TEM)

For all alloys studied, a FEI™ Tecnai G2 F20 transmission electron microscope (TEM) with a Schottky field-emission gun operating at 200 kV was used to record selected area diffraction patterns (SADP), bright-field and dark-field images. In addition, scanning transmission electron

microscopy (STEM) analysis was conducted to investigate the microstructure of some samples. A high angle annular dark-field (HAADF) detector was used for STEM imaging.

3.4.5 3-D Atom Probe Tomography (3D-APT)

Cameca Local Electrode Atom Probe (LEAP 5000XS) instrument was used in the current study to obtain detailed compositional information. This instrument has a depth resolution of ~0.1 nm and a lateral resolution of 0.2 nm. The APT device was operated at a temperature of 30 K, pulse rate of 200 kHz, and a detection rate of 0.005-0.01 ion/pulse in laser mode with laser pulse energy of 50 nJ. IVAS 3.8.4 or AP Suite 6 software was used to analyze the APT data. The mass spectrum for APT reconstructions was calibrated based on the bulk compositions obtained from SEM-EDS. H and Ga contamination from APT chamber and FIB have not been indexed in the mass spectrum for comparison purposes.

3.5 Modeling Tools

3.5.1 Pandat™

PANDAT™ software (2016), from CompuTherm LLC, is an integrated computational tool to calculate phase diagrams and simulate solidification curves. Using PanEngine, Gibbs free energy of every phase can be calculated applying specific thermodynamics parameters. These parameters are used to fit the experimental data to fit the simulated models. The database that was used in this dissertation was PanTitanium, and the parameters were taken from the Scientific Group Thermodata Europe (SGTE) compilation by Dinsdale. In the current work, Pandat was used mainly in the following aspects:

1. Plot solidification curves for various beta titanium alloys presented in the dissertation
2. Calculate β transus temperatures for Ti-1Al-8V-5Fe and Ti-10V-2Fe-3Al (all in wt%)

3.5.2 COMSOL Multiphysics Modeling

The thermo-kinetic effects associated with DED-based LENS processed Ti-185, a multi-track multi-layer 3D thermal model was developed using the finite element method with a quiet/active element activation approach using commercial COMSOL Multiphysics® software. The 3D thermal model for LENS process is developed using following assumptions-

1. The thermo-physical properties related to substrate and powder are considered to be isotropic
2. Due to the lack of availability of temperature-dependent thermo-physical properties of Ti-185 in the open literature, its average temperature-dependent thermo-physical properties were considered by considering its constituent elements [64].
3. The powder addition during the deposition process is considered to be homogenous and approximated using a quiet/active element approach [65], in which addition of material is realized by activating a new group of elements at the beginning of new layer fabrication.

For the sake of simplicity, melt pool hydrodynamics (melt pool formation and the impact of powder particles on the melt pool) is disregarded in the present model. Detailed information on the same is provided in Chapter 5.

3.6 Mechanical Testing Tools

3.6.1 Mini-Tensile Tester

Tensile testing was performed on specimens with gauge length ~5 mm, width ~1.0 mm, and 0.7–1 mm thickness. All samples were polished as detailed in 3.3.3 and cleaned thoroughly before testing. The testing was performed using a customized mini tensile testing machine with a load cell capacity of 500 lbs and a linear variable displacement transformer (LVDT) extensometer. The tensile samples were tested at room temperature under quasi-static conditions at a strain rate of $10^{-3}s^{-1}$. The tensile tests were performed on at least three samples for each condition to ensure statistical accuracy.

CHAPTER 4

UNDERSTANDING THE EFFECT OF SOLUTE ELEMENTS ON THE EVOLUTION OF EQUIAXED AND COLUMNAR GRAINS IN AM PROCESSED BETA TITANIUM ALLOYS

4.1 Introduction

Metal additive manufacturing (AM) is one of the rapidly advancing processing techniques. The layer-by-layer processing and the use of fine metal powders in AM, make the fabrication of parts with complex designs simple, easy, and energy-efficient. The AM processed parts also show enhanced mechanical and functional properties compared to the conventionally processed counterparts [58,66–69]. The improved properties reported are due to unconventional and unique microstructures arising from extremely rapid thermo-kinetics associated with AM processes. The thermal gradients and cooling rates in these processes are significantly higher than conventional castings. Based on the type of AM process, the cooling rates and thermal gradients can vary from $10^2 \; to \; 10^6 \frac{K}{s} \; and \; 10^5 \; to \; 10^7 \frac{K}{m}$, respectively [58]. For instance, the cooling rate reported for the laser cladding process is $10^2 \frac{K}{s}$ [70]and for Laser Engineered Net Shaping (LENS) process is in between $10^3 \; and \; 10^6 \frac{K}{s}$ [58,71–73]. Further, the thermo-kinetics, i.e., cooling rates and thermal gradients associated with the melt pools (caused by laser/electron beam), can be modified by changing the process parameters, thereby providing scope for tuning the microstructures for desired mechanical and functional properties [68]. However, tuning the microstructure requires a comprehensive understanding of the mechanisms behind the microstructural evolution. While there are other interesting aspects of microstructural evolution, such as solid-state phase transformations leading to secondary phase precipitation that occurs during the reheating of previously deposited layers, this chapter mainly focuses on understanding the nucleation and evolution of equiaxed versus columnar grains during solidification (liquid-solid transformation) in

additively processed metastable β Ti alloys.

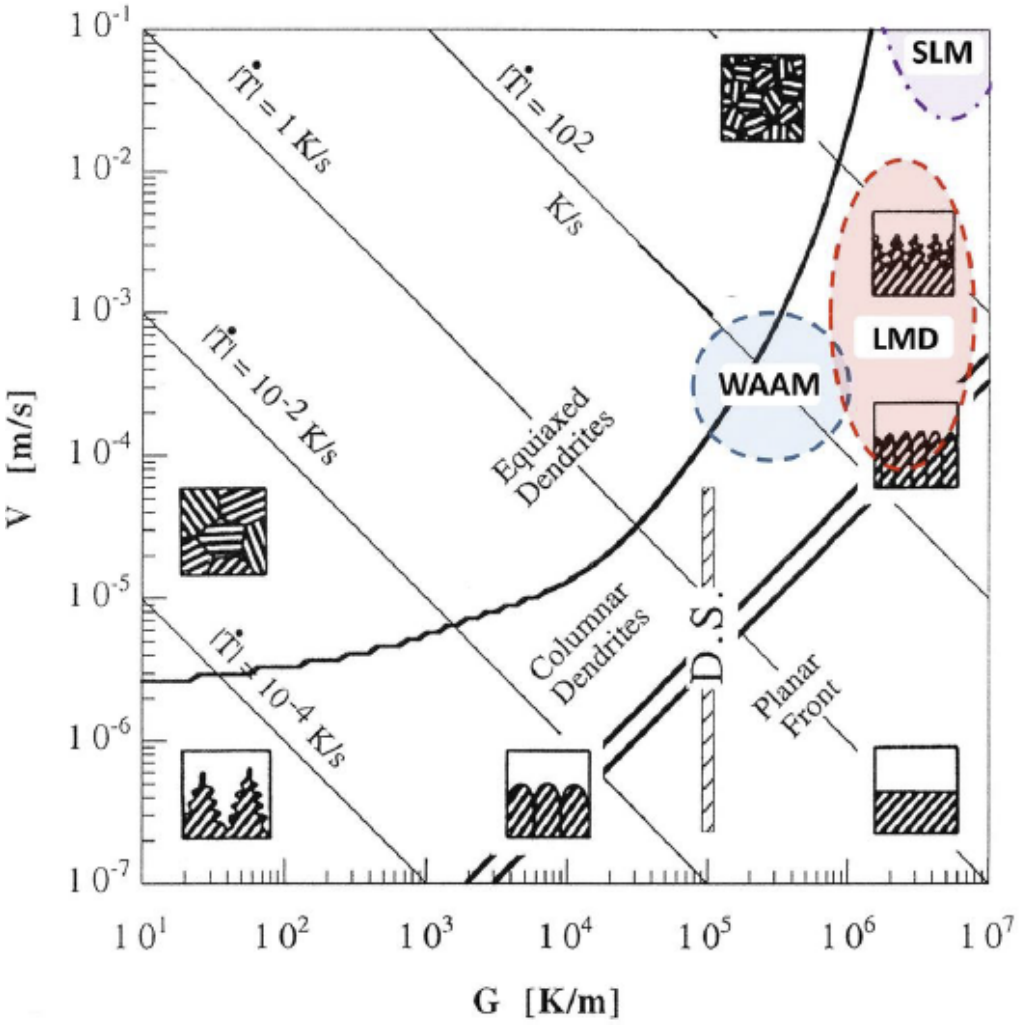

Figure 4.1: G vs V curve for various processing techniques [75]

It is believed that virtually all AM processes involving complete melting of the metal powders produce significantly textured (<001>) columnar grains along the build direction, which are deleterious to the mechanical properties [58,74]. Therefore, controlling the growth and texture of columnar grains becomes crucial for the AM processed alloys. The high cooling rates and thermal gradients are believed to be the factors that critically favor the formation of dendritic/columnar microstructures during solidification (Fig. 4.1) [75]. The epitaxial growth of the subsequent layers from the preceding layer, which is partially remelted due to the provided

energy density, further promotes the formation of columnar grains. Although theoretically, it may seem possible to achieve equiaxed dendrites by optimizing the process parameters, it is practically impossible as the condition of partial remelting of previous layers has to be met for proper fusion between layers for defect-free dense parts (Fig. 4.1).

The columnar to equiaxed transition (CET) of grains has been discussed for decades in the conventional casting of metallic alloys [76–83]. As per Interdependence Theory [84], (a) ΔT_n, critical undercooling required for nucleation; (b) ΔT_{CS}, the extent of constitutional supercooling ahead of solid-liquid interface; (c) x_{sd}, the average spacing between potential nucleation sites; determine the final size and morphology of the grains. It is intuitive that a small ΔT_n, large ΔT_{CS}, and a small x_{sd} favor the formation of refined equiaxed grains. However, among these factors, the rate of development of constitutional supercooling (ΔT_{CS}) is believed to have the most significant effect on grain refinement and therefore is discussed in detail in the following section [75].

During solidification of alloys, a differential partitioning of solute elements between solid and liquid phases occurs, leading to either accumulation or depletion of solute at the solid-liquid interface [85–89]. Such segregation around the growing solid nucleus results in constitutional supercooling (ΔT_{CS}) of the liquid ahead of the interface. Thus, the constitutional supercooling of the liquid results in the activation of many potent nucleation sites, furthering the nucleation of equiaxed dendrites. This leads to the Columnar to Equiaxed transition of the grains. Growth restriction factor (Q) has been proposed initially to quantify the extent of the constitutional supercooling developed due to the segregation of a single solute element in binary alloys [89–91] and is expressed by the following equation:

$$Q = mC_o(K - 1)$$

where m is the liquidus slope in a linear phase diagram, k is the equilibrium solute partition

coefficient, and C_0 is the solute content in the alloy melt.

The growth restriction factor (GRF) model has been significantly developed to evaluate aspects such as potency and shape of the inoculants, final grain size, etc. [87,88,92–95]. Recently, Qian et al. have proposed an analytical model based on Q for predicting the final grain size in conventionally cast ingots [96]. The estimation of Q in 'single solute element' systems (binary alloys) is straightforward and demonstrated successfully by many literature studies [87,88,97,98]. However, the same is not valid for 'multiple solute element' systems, and several different approaches have been discussed in the literature. Desnain et al. were the first to extend the GRF model to multi-component systems [99]. They express the Q for multi-component systems, $Q_{\sum bin}$, as a summation of binary Q values obtained for all solute (i) elements individually with respect to the solvent element.

$$Q_{\sum bin} = \sum Q_{bin,i} = \sum m_{bin,i}(k_{bin,i} - 1)C_{0,i}$$

This approach is crude and disputed by a few as it grossly overestimates the value of Q and disregards any multicomponent interaction between solute elements. A slightly better approximation of Q based on multi-component phase diagrams has been suggested by Quested et al. [100].

$$Q_{multi} = \sum m_i \ (k_i - 1)C_{0,i}$$

$$m_i = \left(\frac{\partial T_L}{\partial C_{0,i}}\right)_{(j \neq i)const.}$$

$$K_i = \frac{C_{S,i}}{C_{L,i}} \ ;$$

Since, composition gradient in the liquid near the interface is not known, $C_{L,i} \approx C_{0,i}$

In this approach, m_i values are directly obtained from the pseudo-binary phase diagrams simulated for each solute element (i), keeping other solutes constant $(j \neq i)$, i.e., the slope of the

liquidus line at $\underset{C0}{\rightarrow}$ for the solute element (i) is taken as m_i . Similarly, K_i values are also calculated from the pseudo-binary phase diagrams using the above expression. Though this approach appears to be more realistic than the method suggested by Desnain et al., it is cumbersome. It requires thermodynamic software and a reliable database for all the elements considered in the alloy system to simulate the multiple pseudo-binary phase diagrams. A more straightforward approach has been recently suggested by Schmid-Fetzer et al., in which they denote the multicomponent growth restriction factor as Q_{true} [101].

$$Q_{true} = \left(\frac{\partial(\Delta T_{CS})}{\partial f_s}\right)_{fs\to 0} = mC_o(K-1)$$

$$\Delta T_{CS} = m(C_0 - C_L)$$

The initial rate of development of constitutional supercooling with a fraction of solid formed (fs) has been derived and expressed as a true growth restriction factor, Q_{true}. Though the idea of using the initial rate of development of constitutional supercooling has been previously mentioned by Easton and St. John in their work [88], Schmid-Fetzer et al. were the first ones to practically demonstrate its applicability in Al and Mg alloys. They also claim that this approach can be extended to a wide range of alloy systems without any difficulties. It should be noted that the concept of GRF was initially proposed for alloys (both single-solute and multiple-solute elements) that are processed using conventional casting techniques where the cooling rates and thermal gradients are significantly lower compared to additive manufacturing (AM) techniques (Fig. 4.1).

Significant research in the last decade has been focused on extending the GRF model to predict the grain size and morphology in additively manufactured alloys [102–107]. Although

Schmid and Fetzer's approach seems more reliable, no reports have been found in AM literature using this approach. Surprisingly, Desnain's method, which is rudimentary and overestimates the value of Q, has been extensively used. This raises critical concerns regarding the applicability of the GRF model to interpret the nucleation and growth behavior of the grains in AM processed alloys. However, it should be noted that overall, the number of reports examining the effect of solute elements on grain morphology evolution in AM processed alloys is still scant. Therefore, there is a need to comprehensively understand and validate the GRF model for AM processed alloys. The current chapter analyses the evolution of grain morphology and texture in a few commercial and model metastable beta (β) titanium alloys. Growth restriction factors (Q) in each case have been determined using the abovementioned approaches. The results indicate that the Growth restriction factor (Q) model fails to interpret the grain growth behavior in the alloys considered. Alternatively, a method based on solidification range has been proposed for the first time to rationalize the same. Altogether, this paper provides insights into understanding the effect of solute elements on the evolution of equiaxed and columnar grains in AM processed beta titanium alloys.

4.2 Experimental Procedure

The elemental powders for Ti, V, Mo, C, Si, and B were procured from Alfa Aesar, USA and the pre-alloyed powders for commercial alloys, TIMETAL 18 (Ti-18), TNZT, Ti-185 and TIMETAL 21S (β-21S) were procured from TOSOH, SMD, USA. The compositions (in wt. %) of the nine different beta-Ti alloys that are additively manufactured are listed in Table 4.1.

Table 4.1: Composition in wt. % of the nine different beta-Ti alloys that are additively manufactured

Alloy	Composition
Ti-20V	Ti-20 wt.% V
Ti-12Mo	Ti-12 wt% Mo

Alloy	Composition
TIMETAL18 (Ti-18)	Ti-5.5 wt.%Al-5 wt.%Mo-5 wt.%V-2.4w.%Cr-0.75wt.%Fe-0.15wt.%O
TNZT	Ti-35 wt.%Nb-7 wt.%Zr-5 wt.%Ta
TIMETAL 21S (b-21S)	Ti-15 wt.%Mo-3 wt.%Nb-2.7 wt.%Al-0.2 wt.%Si
Ti-185	Ti-1 wt.%Al-8 wt.%V-5 wt.%Fe
Ti-18-0.5B	(Ti-18)- 0.5 wt.%B
Ti-18-0.5C	(Ti-18)- 0.5 wt.%C
Ti-18-0.5Si	(Ti-18)- 0.5 wt.%Si

The Optomec LENS-750 system equipped with IPG YLS-1500 fiber laser system (with a maximum power output of 1500 W) was used for the depositions in this study. They were carried out with a single powder hopper loaded with the feedstock powders listed in Table 4.1. The processing parameters used to fabricate these ten alloys were: 600 W laser power; 0.5 mm diameter laser beam on the sample surface; 12.7mm/s laser scan speed; 0.254 mm vertical layer spacing; 0.381 mm hatch width with 90° rotation in the hatch direction between layers. These combinations of laser parameters provided input energy fluence of 94.48 J/mm^2. The input energy fluence/energy density was calculated using the expression $E = P/V \times D$, where P is the laser power, V is the scan speed, and D is the laser beam diameter. The oxygen level in the glove box was maintained below 10 ppm to fabricate composite blocks of dimensions of 25.4 mm x25.4 mm x25.4 mm. The deposited builds were then separated from the Ti64-seed plate, and subsequently, two thin sections (parallel and perpendicular to the build direction) were sliced using a KENT USA (WSI-200) electric discharge machine (EDM) for microstructural analysis.

X-ray diffraction studies for the LENS deposited samples were performed using (1.54 CuKα) line of Rigaku Ultima III X-ray Diffractometer. The as-deposited samples were polished using standard metallographic techniques followed by the final polishing in 0.05-μm colloidal silica in a Buehler Vibromet2 for microstructural characterization. A FEI Nova NanoSEM 230 was used for the microstructure, phase, and compositional analysis of the as-deposited composites.

TSL-OIM™ software was used for generating inverse pole figure (IPF) and texture maps from the electron backscattered diffraction (EBSD) data. Thermodynamic modeling of the solidification curves (temperature versus the fraction of solid formed (fs)) was performed using PANDAT™ software (from CompuTherm) installed with a Ti database.

4.3 Results

EBSD scans were performed along the build direction on the as-deposited Ti-20V (model β Ti alloy) to determine the texture and morphology of the grains. The obtained inverse pole figure (IPF) maps and texture plots (bottom left inset) are shown in Figure 4.2(a). The IPF maps clearly show the presence of long-columnar grains along the build direction of the Ti-20V deposit. Besides, the texture plot (in the inset) reveals a significant <001> β type texture along the build direction in the columnar grains. The XRD spectra obtained from the top surface of the Ti-20V deposit is shown in Figure 4.2(b). Only one peak corresponding to (002)β has been indexed, which further corroborates with the EBSD data (indicating the presence of significant <001>/<002> β texture). Figure 4.2(c) shows the solidification curve for the Ti-20V alloy simulated using PANDAT™ software. The solidification range of Ti-20V alloy has been predicted to be ~10℃. Similarly, the IPF maps with texture plots (in the inset) and the solidification curves obtained for the as-deposited Ti-12Mo (model alloy) and Ti-18 (commercial alloy) are shown in Figure 4.3 (a & b), and (c & d), respectively. Both the alloys, Ti-12Mo and Ti-18 clearly exhibit long columnar grains with significant <001>β texture along the build direction. The solidification ranges were found to be ~110℃ in Ti-12Mo and ~125℃ in Ti-18. The impact of the solidification range on the evolution of grain morphology and texture is analyzed in the discussion section of this paper.

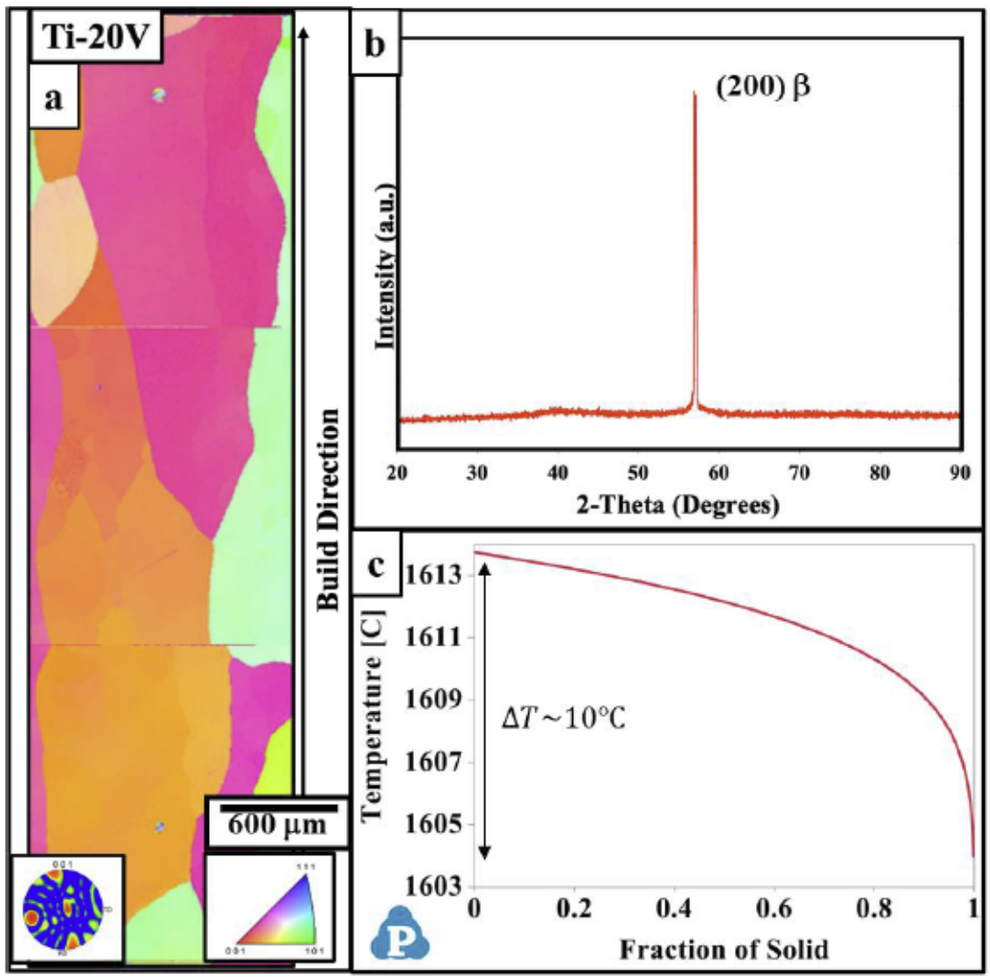

Figure 4.2: (a) IPF map with texture plot (in the inset) obtained along the build direction (b) XRD spectra obtained from the top surface (perpendicular to the build direction) of LENS processed Ti-20V. (c) Solidification curve for the same alloy simulated using PANDAT^{TM} software

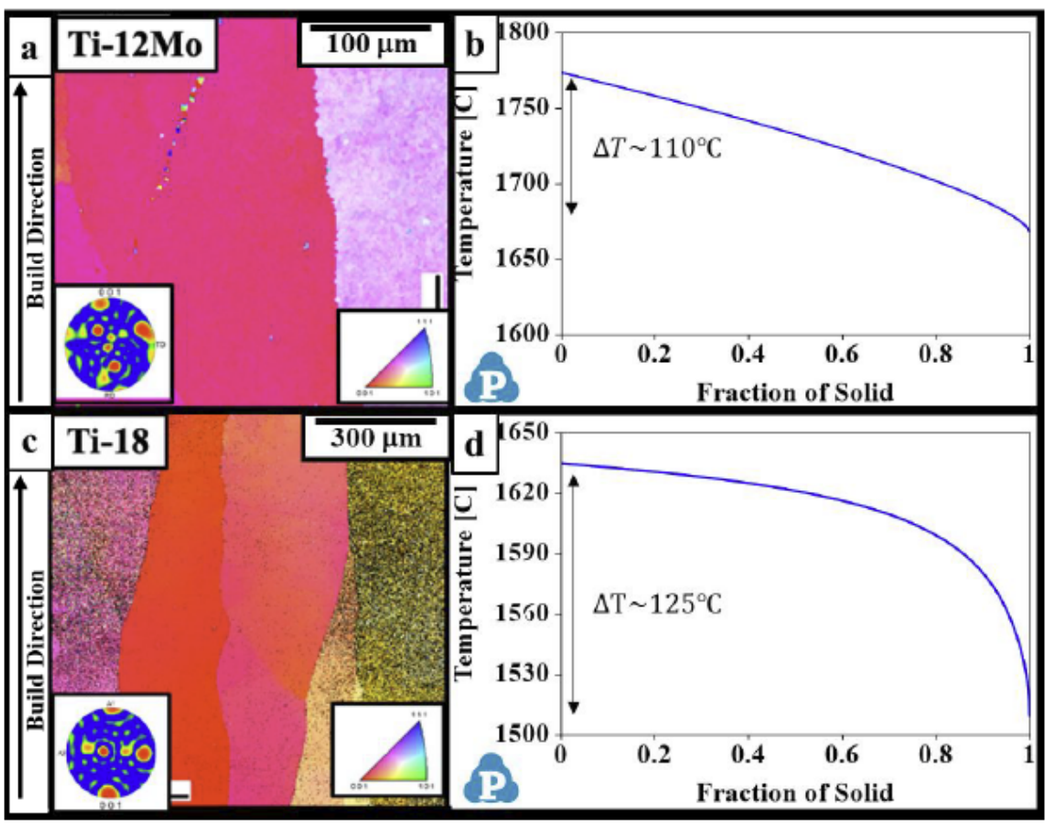

Figure 4.3: IPF map with texture plot (in the inset) obtained along the build direction for LENS processed (a) Ti-12wt%Mo (c) Ti-18 commercial alloy. Solidification curves simulated using PANDAT^{TM} software for (b) Ti-12wt%Mo (d) Ti-18 commercial alloy.

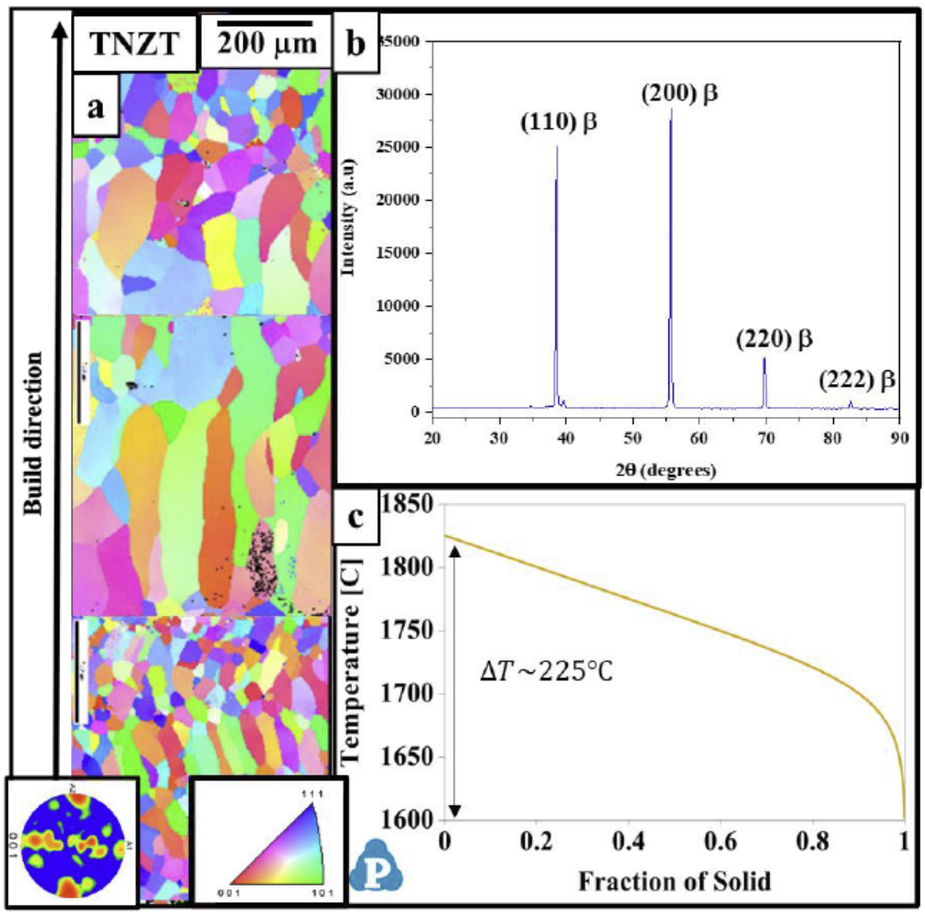

Figure 4.4: (a) IPF map with texture plot (in the inset) obtained along the build direction (b) XRD spectra obtained from the top surface (perpendicular to the build direction) of LENS processed TNZT alloy. (c) Solidification curve for the same alloy simulated using PANDAT^{TM} software

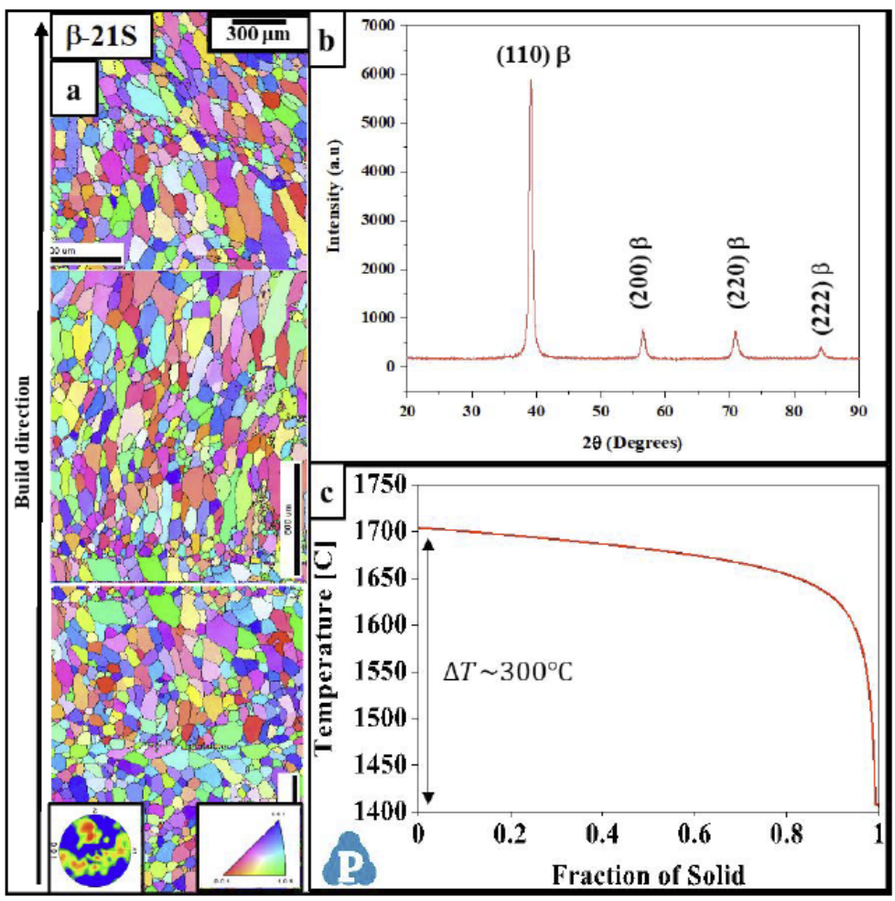

Figure 4.5: (a) IPF map with texture plot (in the inset) obtained along the build direction (b) XRD spectra obtained from the top surface (perpendicular to the build direction) of LENS processed b-21S alloy. (c) Solidification curve for the same alloy simulated using PANDAT^{TM} software.

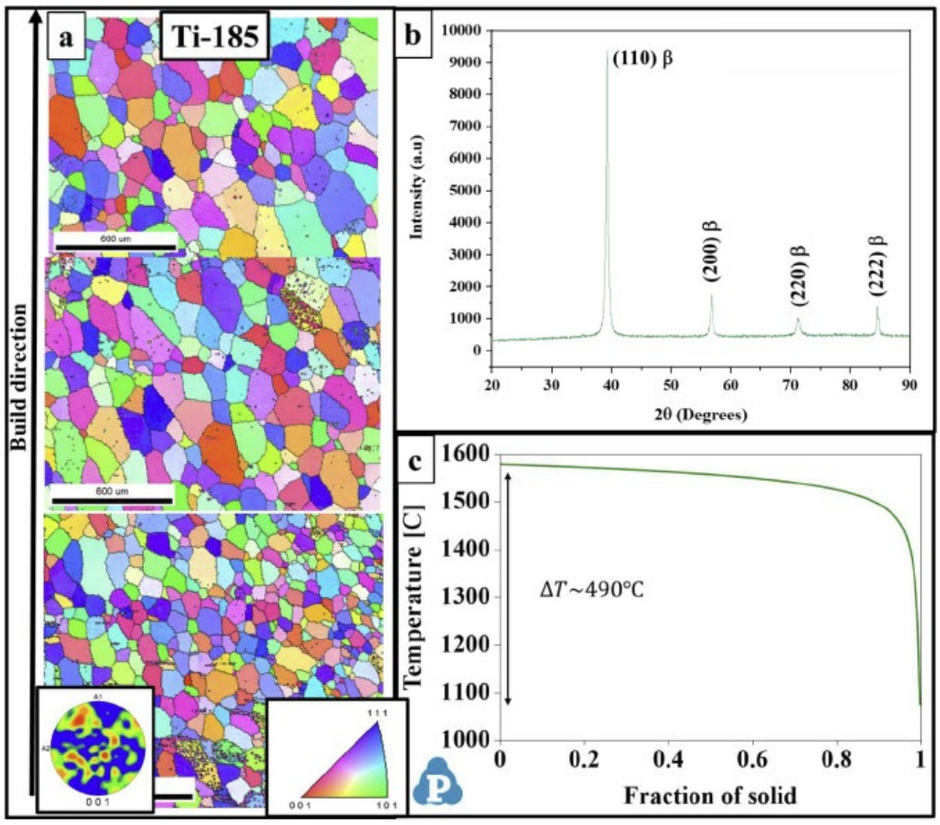

Figure 4.6: (a) IPF map with texture plot (in the inset) obtained along the build direction (b) XRD spectra obtained from the top surface (perpendicular to the build direction) of LENS processed Ti-185 alloy. (c) Solidification curve for the same alloy simulated using PANDAT^{TM} software

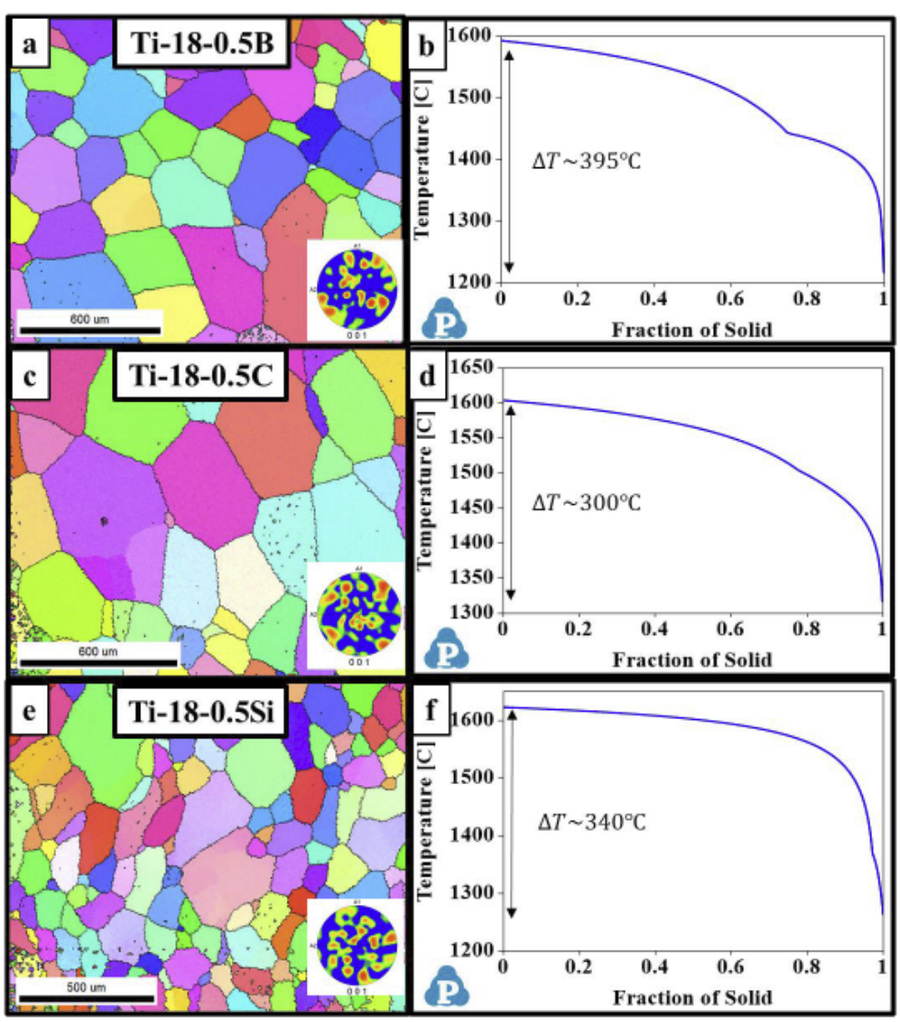

Figure 4.7: IPF map with texture plot (in the inset) obtained along the build direction for LENS processed (a) Ti-18-0.5B (c) Ti-18-0.5C (e) Ti-18-0.5Si. Solidification curves simulated using PANDAT^{TM} software for the LENS processed (b) Ti-18-0.5B (d) Ti-18-0.5C (f) Ti-18-0.5Si

The IPF maps with texture plot (bottom left inset) obtained along the build direction of as-deposited TNZT (commercial alloy) are shown in Figure 4.4(a). Unlike, Ti-20V, Ti-12Mo and Ti-18 which exhibit fully columnar grains, TNZT exhibits mixed columnar-equiaxed grains along the build direction. However, it should be noted that the grain sizes (at various regions along the build direction) observed in the TNZT is less than 350 μm which is significantly lower as compared to the grain sizes in the other three alloys, Ti-20V, Ti-12Mo and Ti-18 (grain size >1.5 mm). Additionally, the TNZT alloy exhibits moderate <001>β texture along the build direction, as revealed by the texture plot (inset in Fig. 4.4(a)). The XRD spectra obtained from the top surface of the deposit, shown in Figure 4.4(b) confirms the presence of the same, i.e., moderate <001>/<002>β type texture along the build direction. Figure 4.4(c) shows the solidification curve for the TNZT alloy simulated using PANDAT^{TM} software. The solidification range of TNZT alloy has been predicted to be ~225℃. The IPF maps with texture plot (bottom left inset) obtained along the build direction of as-deposited β-21S (commercial alloy) are shown in Figure 4.5(a). Similar to TNZT, β-21S exhibits mixed columnar-equiaxed grains along the build direction. However, the texture plot shown in Figure 4.5(a) (inset) and the XRD spectra obtained from the top surface of the deposit shown in Figure 4.5(b) do not reveal any significant <001>/<002>β type texture along the build direction. Figure 4.5(c) shows the solidification curve for the β-21S alloy simulated using PANDAT^{TM} software. The solidification range of β-21S alloy has been predicted to be ~300℃.

The IPF maps with texture plot (bottom left inset) obtained along the build direction of as-deposited Ti-185 (commercial alloy) are shown in Figure 4.6(a). Ti-185 alloy exhibited fully equiaxed grains along the build direction as opposed to mixed columnar-equiaxed grains observed in TNZT and β-21S alloys, and fully columnar grains in Ti-20V, Ti-12Mo and Ti-18 alloys. Further, the texture plot shown in Figure 4.6(a) (inset) and the XRD spectra obtained from the top surface

of the deposit shown in Figure 4.6(b) do not show any signs of <001>/<002>β type texture along the build direction. This is in sharp contrast with the observations in the other five alloys which showed moderate to high <001>β texture along the build direction. Figure 4.6(c) shows the solidification curve for the Ti-185 alloy simulated using PANDAT^{TM} software. The solidification range of Ti-185 alloy has been predicted to be ~490℃.

Further, to examine the effect of inoculants like carbon, boron and silicon in restricting the grain growth, 0.5 wt% of the same elements were individually added to Ti-18 commercial pre-alloyed powders prior to the deposition. The IPF maps with texture plots (bottom right inset) obtained from the middle region along the build direction of Ti-18-0.5B, Ti-18-0.5C and Ti-18-0.5Si are shown in Figure 4.7 (a), (c) and (e), respectively. All the three alloys clearly exhibit fully equiaxed grains without any significant <001>β texture along the build direction. It should be noted that, the grain morphology changes from fully columnar observed in Ti-18 (Fig. 4.3(c)) to fully equiaxed observed in the inoculant containing alloys, Ti-18-0.5B, Ti-18-0.5C and Ti-18-0.5Si indicating a significant effect of the inoculant elements in the grain refinement. Figure 4.7 (b), (d) and (f) show the solidification curves for the Ti-18-0.5B, Ti-18-0.5C and Ti-18-0.5Si alloys, respectively simulated using PANDAT^{TM} software. The solidification ranges for Ti-18-0.5B, Ti-18-0.5C and Ti-18-0.5Si alloys have been predicted to be ~395℃, ~300℃, and ~340℃, respectively.

4.3.1 Calculation of Growth Restriction Factors (Q)

Growth restriction factors for all the alloys considered in the study were calculated using two approaches: (a) Desnain's approach, referred as $Q_{\sum bin}$; (b) Schmid and Fetzer's approach, referred as Q_{true}.

4.3.1.1 Calculation of $Q_{\sum bin}$

As mentioned in the introduction section of the chapter, the growth restriction factor for multi-component systems, $Q_{\sum bin}$ is expressed as a summation of binary Q values obtained for all solute (i) elements individually with respect to the solvent element.

$$Q_{\sum bin} = \sum Q_{bin,i} = \sum m_{bin,i}(k_{bin,i} - 1)C_{0,i}$$

The $k_{bin,i}$ and $m_{bin,i}$ are directly obtained from the binary phase diagrams of solute element (i) with the solvent element which is Ti (in the current study). $C_{0,i}$ is taken as the weight percent of the solute element (i) in the alloy [99,101]. The values of m and K for various elements have been obtained directly from the literature and the product, $m_{bin,i}$ $(k_{bin,i} - 1)$ for each element (i) is listed in Table 4.2 [103]. The calculation of Growth Restriction Factors ($Q_{\sum bin}$) for all the alloys considered in the current study are shown in Table 4.3.

Table 4.2: Calculated m(k − 1) values for elements in titanium

Element (i)	$m_{bin,i}$ $(k_{bin,i} - 1)$
Al	0
V	0
Fe	3.8
Mo	4.5
Nb	2.5
Si	21.7
B	66
Ta	0
Zr	0.3
Cr	1.5
O	0
C	378

Table 4.3: Calculation of Growth Restriction Factor ($Q_{\sum bin}$) for all the additively processed alloys

Alloy	$Q_{\sum bin}$
Ti-20V	$Q_{\sum bin} = m_{bin,V}(k_{bin,V} - 1)C_{0,V}$ =0(20)=0
Ti-12Mo	$Q_{\sum bin} = m_{bin,Mo}(k_{bin,Mo} - 1)C_{0,Mo}$ =4.5(12)=54
TIMETAL18 (Ti-18)	$Q_{\sum bin} = m_{bin,Al}(k_{bin,Al} - 1)C_{0,Al} + m_{bin,Mo}(k_{bin,Mo} - 1)C_{0,Mo} + m_{bin,V}(k_{bin,V} - 1)C_{0,V} + m_{bin,Cr}(k_{bin,Cr} - 1)C_{0,Cr} + m_{bin,Fe}(k_{bin,Fe} - 1)C_{0,Fe} + m_{bin,O}(k_{bin,O} - 1)C_{0,O}$= 0(5.5) +5(4.5)+0(5)+1.5(2.4)+3.8(0.75)+0(0.15)=28.95
TNZT	$Q_{\sum bin} = m_{bin,Nb}(k_{bin,Nb} - 1)C_{0,Nb} + m_{bin,Zr}(k_{bin,Zr} - 1)C_{0,Zr} + m_{bin,Ta}(k_{bin,Ta} - 1)C_{0,Ta}$= 2.5(35)+0.3(7)+5(0) =89.6
TIMETAL 21S (b-21S)	$Q_{\sum bin} = m_{bin,Al}(k_{bin,Al} - 1)C_{0,Al} + m_{bin,Mo}(k_{bin,Mo} - 1)C_{0,Mo} + m_{bin,Si}(k_{bin,Si} - 1)C_{0,Si} + m_{bin,Nb}(k_{bin,Nb} - 1)C_{0,Nb}$= 2.7(0)+ 15(4.5)+3(2.5)+0.2(21.7) = 79.34
Ti-185	$Q_{\sum bin} = m_{bin,Al}(k_{bin,Al} - 1)C_{0,Al} + m_{bin,V}(k_{bin,V} - 1)C_{0,V} + m_{bin,Fe}(k_{bin,Fe} - 1)C_{0,Fe}$= 0(1)+0(8)+3.8(5)=19
Ti-18-0.5B	$Q_{\sum bin} = m_{bin,Al}(k_{bin,Al} - 1)C_{0,Al} + m_{bin,Mo}(k_{bin,Mo} - 1)C_{0,Mo} + m_{bin,V}(k_{bin,V} - 1)C_{0,V} + m_{bin,Cr}(k_{bin,Cr} - 1)C_{0,Cr} + m_{bin,Fe}(k_{bin,Fe} - 1)C_{0,Fe} + m_{bin,O}(k_{bin,O} - 1)C_{0,O} + m_{bin,B}(k_{bin,B} - 1)C_{0,B}$ = 0(5.5) +5(4.5)+0(5)+1.5(2.4)+3.8(0.75)+0(0.15)+0.5(66)=61.95
Ti-18-0.5C	$Q_{\sum bin} = m_{bin,Al}(k_{bin,Al} - 1)C_{0,Al} + m_{bin,Mo}(k_{bin,Mo} - 1)C_{0,Mo} + m_{bin,V}(k_{bin,V} - 1)C_{0,V} + m_{bin,Cr}(k_{bin,Cr} - 1)C_{0,Cr} + m_{bin,Fe}(k_{bin,Fe} - 1)C_{0,Fe} + m_{bin,O}(k_{bin,O} - 1)C_{0,O} + m_{bin,C}(k_{bin,C} - 1)C_{0,C}$ = 0(5.5) +5(4.5)+0(5)+1.5(2.4)+3.8(0.75)+0(0.15)+0.5(378)=217.95
Ti-18-0.5Si	$Q_{\sum bin} = m_{bin,Al}(k_{bin,Al} - 1)C_{0,Al} + m_{bin,Mo}(k_{bin,Mo} - 1)C_{0,Mo} + m_{bin,V}(k_{bin,V} - 1)C_{0,V} + m_{bin,Cr}(k_{bin,Cr} - 1)C_{0,Cr} + m_{bin,Fe}(k_{bin,Fe} - 1)C_{0,Fe} + m_{bin,O}(k_{bin,O} - 1)C_{0,O} + m_{bin,Si}(k_{bin,Si} - 1)C_{0,Si}$ = 0(5.5) +5(4.5)+0(5)+1.5(2.4)+3.8(0.75)+0(0.15)+0.5(21.7)=39.8

4.3.1.2 Calculation of Q_{true}

As previously mentioned, this approach of estimating Q is believed to be simpler and more realistic than the method suggested by Desnain et al. i.e., $Q_{\sum bin}$. In this approach the initial slope of development of constitutional supercooling (ΔT_{CS}) with respect to the fraction of solid formed is assumed to be the growth restriction factor, Q_{true}.

$$Q_{true} = \left(\frac{\partial(\Delta T_{CS})}{\partial f_s}\right)_{fs \to 0} = mC_o(K-1)$$

$$\Delta T_{CS} = m(C_0 - C_L)$$

The solidification curves simulated using PANDAT^{TM} provides the profile of liquidus temperature (T_L) with change in the fraction of solid formed (f_s) (e.g., Fig. 4.2(c)). ΔT_{CS} is the maximum available undercooling, which is the positive temperature difference to liquidus point (T_L) at C_0 [101]. Since the solidification curves are generated at C_0, the change in the range of constitutional supercooling ΔT_{CS} with increase in fs can be calculated directly from the raw data. It should be noted that ΔT_{CS} is maximum initially (at $f_s \rightarrow 0$) and slowly decreases with an increase in the fraction of solid formed (fs) and vanishes at $f_s \rightarrow 1$. For instance, the change in range of constitutional supercooling ΔT_{CS} with an increase in fs calculated for Ti-185 alloy is shown in Figure 4.8. The initial slope of this curve, i.e., slope determined for the region where $0 < fs < 0.01$ (at $f_s \rightarrow 0$) is the true growth restriction factor, Q_{true}, which is found out to be 29.387 in this alloy (Fig. 4.8). Similarly, the Q_{true} values have been determined for the rest of the alloys following this procedure, and the values have been listed in Table 4.4.

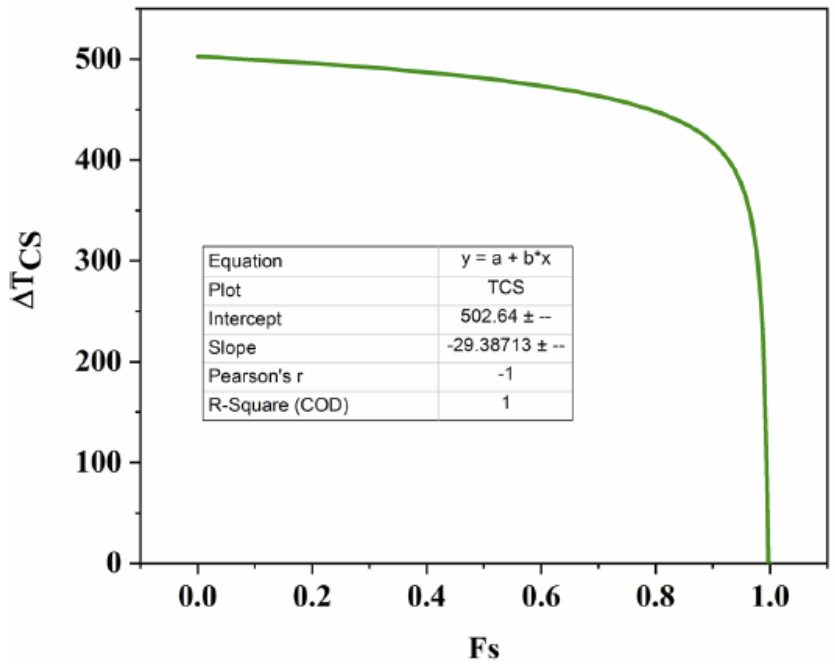

Figure 4.8: The change in range of constitutional supercooling ΔT_{CS} with increase in fs calculated for Ti-185 alloy

Table 4.4: Summary of the experimental observations and estimated Growth Restriction Factors (Q) for all the alloys that are additively manufactured in the present study

Alloy	Grain Morphology	Texture <001>b	Solidification Range	Growth Restriction Factor (Q)	
				$Q_{\sum bin}$	Q_{true}
Ti-20V	Long, columnar	Strong	~10℃	0	2.55
Ti-12Mo	Long, columnar	Strong	~110℃	54	75.92
Ti-18	Long, columnar	Strong	~125℃	28.95	18.53
TNZT	Columnar-equiaxed mixed	Moderate	~225℃	89.6	133.20
b-21S	Columnar-equiaxed mixed	Moderate	~300℃	79.34	42.23
Ti-185	Fully equiaxed	Weak	~490℃	19	29.38
Ti-18-0.5B	Fully equiaxed	Weak	~395℃	61.95	61.76
Ti-18-0.5C	Fully equiaxed	Weak	~300℃	217.95	47.60
Ti-18-0.5Si	Fully equiaxed	Weak	~340℃	39.8	26.13

4.4 Discussion

The experimental observations (grain morphology and texture) and the estimated Growth Restriction Factors (Q) for the nine alloys are summarized in Table 4.4. The alloys Ti-20V, Ti-12Mo, and Ti-18 exhibited long columnar grains with significant <001>β texture along the build direction. While TNZT and β-21S showed mixed columnar-equiaxed grains with moderate <001>β texture along the build direction. Among the nine alloys, Ti-185, Ti-18-0.5B, Ti-18-0.5C, and Ti-18-0.5Si are the only ones that exhibited fully equiaxed grains with randomized texture along the build direction. According to the GRF model, a high Q value indicates the formation of fine equiaxed grains, and a low Q value suggests the formation of long columnar grains in any given alloy. It is clear from the summary presented in Table 4.4 that the Q values estimated using both approaches do not explain the grain morphologies observed in the alloys considered in the present study. For instance, Ti-12Mo with a Q_{true} value of 75.92 and a $Q_{\sum bin}$ value of 54 exhibits long columnar grains along the build direction instead of the predicted equiaxed grains. Similarly,

Ti-185 alloy with relatively lower Q values exhibits fully equiaxed microstructure along its build direction.

GRF (Q) model analyzes the effect of solute elements in restricting the growth of already formed grains in conventionally cast ingots. In other words, this theory is entirely based on the assumption that there is some previously developed solid in the liquid melt, i.e., fs $\neq 0$ to begin with. It mainly focuses on the secondary nucleation events that occur due to the constitutional supercooling of the liquid ahead of the growing solid disregarding the aspects of primary nucleation resulting in the formation of the initial solid in the liquid melt. It should be noted that constitutional supercooling arises from the solute element segregation, which is profound in conventional casting due to the significantly slower cooling rates.

On the other hand, the highly rapid thermokinetics in the Additive manufacturing processes limit/arrest the segregation of solute elements by not providing enough time for the elements to diffuse across the solid-liquid interface. Therefore, the concept of the development of constitutional supercooling and subsequent secondary nucleation events that lead to equiaxed microstructures may not be valid for AM-processed alloys. In such cases, the final microstructure is determined mainly by the primary nucleation events that occur in the liquid melt, i.e., at fs = 0. It is understood from the fundamentals of solidification in metal/alloy systems that a critical level of undercooling (ΔT_c) is required to form a stable spherical solid nucleus within the liquid melt. To be specific, the solidification process occurs only when the regions in the liquid melt overcome the critical free energy barrier (ΔG^*) barrier. Based on homogenous nucleation theory [108], the critical free energy barrier (ΔG^*) barrier can be defined as shown below:

$$\Delta G^* = \frac{[16\pi(\gamma_{SL})^3(T_m)^2]}{3(\Delta T_c)^2(\Delta H_m)^2}$$

$$N \sim A \times exp\left(\frac{-\Delta G^*}{KT}\right)$$

where ΔG^* is the critical nucleation barrier; γ_{SL} is the liquid|solid interfacial free energy per unit area; $T_{(m)}$ is the melting temperature; ΔT_c is the critical undercooling; ΔH_m is the latent heat of fusion; N is the nucleation rate; A is a constant based on diffusivity;K is Boltzman constant; T is the temperature of the liquid metal/alloy

From the above expressions, it is evident that the critical barrier for nucleation (ΔG^*) decreases with an increase in the level of undercooling (ΔT_c), which in turn increases the rate of nucleation (N). A higher nucleation rate (N) leads to a higher number density of stable spherical nuclei. The hard impingement with the neighboring grains (growth of stable nuclei leads to the formation of grains) suppresses the extent of grain growth and results in an equiaxed microstructure. The solidification/freezing range of the alloy plays a crucial role in governing the primary nucleation behavior. The rapid cooling rates in AM processes provide scope for attaining higher levels of undercooling (ΔT_c) in alloys with large solidification/freezing ranges prior to the onset of the solidification process. This increases the propensity to form equiaxed microstructure in such alloys compared to those with smaller solidification/freezing ranges. The alloys in the present study that are characterized by small solidification ranges (< 150℃), i.e., Ti-20V, Ti-12Mo, and Ti-18, exhibit fully columnar grains with strong <001>β type texture along the build direction. While, the alloys with medium solidification ranges (150-300℃), i.e., β-21S and TNZT, exhibit mixed columnar-equiaxed grains with moderate <001>β type texture along the build direction. On the other hand, the alloys with large solidification ranges (> 300℃), i.e., Ti-185, Ti-18-0.5B, Ti-18-0.5C, and Ti-18-0.5Si, exhibit fully equiaxed grains without any noticeable texture along the build direction. It is worth mentioning that the addition of inoculant elements like

carbon, boron, and silicon has significantly increased the freezing/solidification range for Ti-18 alloy (Fig. 4.7) which led to the change in grain morphology from fully columnar in Ti-18 to fully equiaxed in Ti-18-0.5B, Ti-18-0.5C, and Ti-18-0.5Si alloys. Besides, it is also evident from the summary Table 4.4 that the texture developed in the AM processed alloys is entirely dependent on the grain growth, i.e., the long columnar grains tend to exhibit <001> β type texture as opposed to no preferred texture exhibited by finer equiaxed grains.

4.5 Conclusions

This chapter mainly investigates the effect of solute elements on the evolution of equiaxed and columnar grains in AM processed beta titanium alloys. Nine different alloys were chosen for this study and were fabricated using LENS process, a laser based DED technique. The microstructural aspects such as grain morphology and texture in the build direction were investigated for all the nine alloys. Ti-20V, Ti-12Mo, Ti-18 exhibited long columnar grains with significant <001>β texture in the build direction. TNZT, and β-21S exhibited mixed columnar-equiaxed grains with moderate <001>β texture. While Ti-18-0.5B, Ti-18-0.5C, Ti-18-0.5Si and Ti-185 revealed equiaxed grains with random texture along the build direction. The Growth restriction factor (Q) in each alloy has been determined using two approaches, (a) Schmid and Fetzer's approach (reliable) and (b) Desnain's approach (rudimentary), to understand the effect of alloying elements on the grain morphology and texture observed in these alloys. The results presented indicate that Growth restriction factors (Q) that are originally developed for conventional casting techniques (both the approaches) fail to interpret the grain growth behavior in the AM processed β-Ti alloys. Alternatively, an approach based on fundamentals of homogenous nucleation and freezing range has been proposed to rationalize the observations.

CHAPTER 5

ADDITIVE MANUFACTURING OF COMMERCIAL BETA TITANIUM ALLOY: Ti-1Al-8V-5Fe*

5.1 Introduction

Metastable β-Ti alloys, typically containing substantial amounts of one or more beta stabilizing elements like Mo, V, Cr, Fe, Cu, Mn, etc., are of widespread interest for many applications due to their lower elastic modulus, higher specific strength enhanced fracture toughness and augmented fatigue resistance as compared to other α+β Ti alloys [109–113]. There are a number of different commercially available metastable β-Ti alloys like Ti-10V-2Fe-3Al (Ti-1023), Ti-1Al-8V-5Fe (Ti-185), Ti-13V-11Cr-3Al, Ti-15Mo-3Al-3Nb-0.2Si (known as β-21S) and Ti-3Al-8V-6Cr-4Mo-4Zr (known as Beta-C) [27,114,115]. These alloys typically retain their body-centred cubic (bcc, β) structure and do not from α' martensite when quenched from above the β-transus temperatures. However, precipitation of other phases like α (alpha) and metastable ω (omega) within the β matrix is possible during ageing of these alloys below their β-transus temperature, which has been shown to further enhance their mechanical properties [14,109]. Ti-185 due to its high strength and fatigue life [8], is currently being utilized for fastener applications in the aerospace industry, with a microstructure consisting of grain boundary and intra-granular α precipitates within the β grains [114]. Although the commercial β Ti alloys like Ti-185 and Ti-1023 contain higher amounts of low-cost alloying elements like Fe, they are not extensively used due to the strong micro-segregation of Fe that occurs during conventional ingot casting [116–118].

---

* This chapter is reproduced in its entirety from M.S.K.K.Y. Nartu, S. Dasari, A. Sharma, S.A. Mantri, S. Sharma, M. V. Pantawane, B. McWilliams, K. Cho, N.B. Dahotre, R. Banerjee, Omega versus alpha precipitation mediated by process parameters in additively manufactured high strength Ti–1Al–8V–5Fe alloy and its impact on mechanical properties, Mater. Sci. Eng. A. (2021) 141627, https://doi.org/10.1016/j.msea.2021.141627 with permission from Elsevier.

This micro-segregation, also known as the beta-fleck effect [117], results in large variations in composition eventually leading to the precipitation of undesired brittle phases in these alloys. For instance, the yield strength and strain to failure of Ti-1023 alloys is shown to decrease from 1176 to 1036 MPa and 6% to 1%, respectively, due to the effect of β-flecks [119]. A slight increase in volume fraction or the size of β-flecks leads to a significant decrease in the low cycle fatigue (LCF) and strain to failure in these alloys [32]. The fracture toughness is also shown to be significantly affected by the presence of β-flecks [30,120,121]. The beta flecks once formed, are difficult to eliminate. Hot forging in the β-phase field is found to be ineffective in eliminating the chemical inhomogeneities arising during the conventional processing of these alloys [32]. Long-term annealing can be performed as an alternative to eliminate the β-flecks and to homogenize the metastable β-Ti alloys [109]. However, this additional post processing may increase the cost of fabrication considerably and therefore is not industrially viable.

Powder metallurgy (P/M) based routes have been successfully employed for processing Ti-185 reducing the beta fleck problem [122]. Though Joshi et al. [122] have reported an enormous tensile strength of 1655 MPa with 4-6% ductility, the processing is tedious and expensive. Devaraj et al. [123] demonstrated an innovative low cost thermo-mechanical processing route to achieve high strength in P/M fabricated Ti-185. Recently, Azizi et al. [124] have successfully fabricated Ti-185 via SLM (Selective Laser Melting, a powder-bed based laser additive manufacturing (AM) technique), without any significant Fe segregation and minimal porosity. Additionally, other β-Ti alloys, that suffer from the β-fleck problem during conventional processing, have been successfully processed using additive manufacturing techniques such as laser engineered net shaping (LENS) and Wire arc additive manufacturing (WAAM) [60,120,125]. Therefore, AM could be particularly attractive for fabricating β-Ti alloys (containing eutectoid elements) such as

Ti-185 [126], preventing the β-fleck problem, owing to the smaller meltpool inherently rapid solidification rates [127].

However, AM processed Ti alloys, including β-Ti alloys, often suffer from growth of columnar grains and development of a strong <001>β texture along the build direction [47,55,61,128–132]. This results in anisotropic mechanical properties [133–138]. Previous reports indicate that either by promoting the nucleation rates in the molten pool or by modifying the kinetics/thermodynamics of solidification, fine β grains with equiaxed morphology and randomized texture can be obtained, leading to better mechanical properties [59,139–149]. However, these investigations are rather limited in number and there is still a need to comprehensively understand the process-microstructure-property relationships for additively manufactured β-Ti alloys. The objective of this study is to evaluate the microstructure and mechanical properties of LENS processed Ti-185 focusing on the β grain morphology, intra-granular α/ω precipitation, and their impact on tensile properties.

5.2 Experimental Procedure

5.2.1 Materials and Methods

An Optomec LENS-750 was used for fabricating Ti-185 on a Ti-64 seed plate. In order to eliminate the problem of compositional differences arising due to elemental powder blends, pre-alloyed powders of Ti-185 were procured from Tosoh SMD, Inc. for this study. The pre-alloyed powder has been characterized in detail and the results are shown in Figure 5.1. Thus, Figure 5.1(a) shows a backscatter SEM image of the power particles, revealing the near perfect spherical morphology of these electrode induction melting inert gas atomization (EIGA) processed powders. Figure 5.1(b) shows the particle size distribution with an average size ~ 92μm. Figure 5.1(c) shows

the x-ray diffraction pattern from these powders establishing the single β phase in these powders prior to laser additive processing.

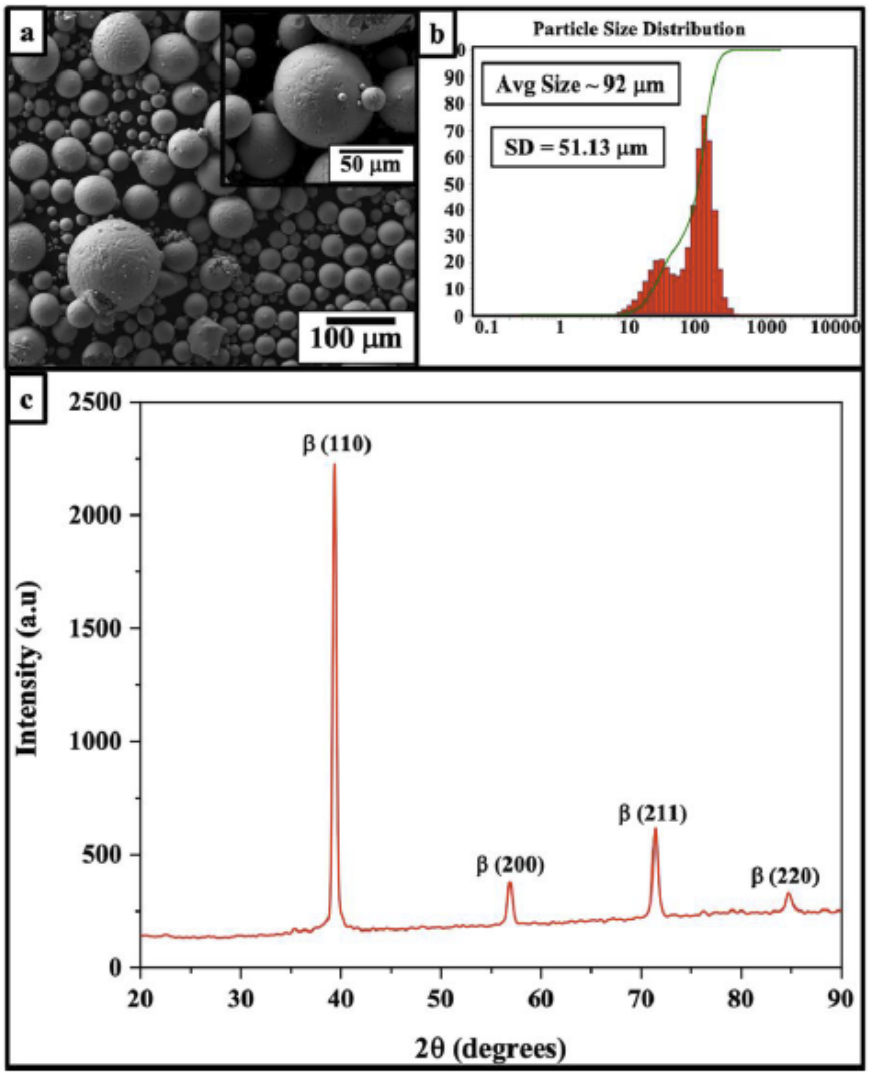

Figure 5.1: a) SEM of pre-alloyed Ti-185 powder with inset showing the higher magnification image, (b) particle size distribution, (c) XRD of Ti-185 powder showing single phase β-bcc peaks.

A 1500 W Nd: YAG laser that produces near-infrared radiation at a wavelength of 1.064 µm was used for the deposition. Three different laser powers, i.e. 300, 400 & 500 W were used for the fabrication. The other processing parameters were maintained unchanged and were: 0.5 mm laser beam on the sample surface; 12.7mm/s laser scan speed; 0.254 mm vertical layer spacing; 0.381 mm hatch width with 90° rotation in the hatch direction between layers. These combinations of

laser parameters provided input energy densities of 47.24 J/mm^2, 62.99 J/mm^2 & 78.74 J/mm^2 to fabricate blocks of dimensions of 25.4 mm x25.4 mm x25.4 mm. The oxygen level in the glove box was maintained below 10 ppm during deposition of the alloys. The deposited builds were then separated from the seed plate and subsequently sliced into two sections along the build direction using a KENT USA (WSI-200) electric discharge machine (EDM). One of the sections was utilized for machining specimens (perpendicular to the build direction) for tensile property measurements and the other section was utilized for microstructural analysis. The dimensions of the tensile specimens were: gauge length ~ 5 mm, width ~ 1 mm and thickness ~ 0.7–1 mm. Additionally, a bar of dimensions 50 mm length, 8 mm width, and about 9 mm height were sectioned from a conventionally cast/forged slab of Ti-185. The bar was encapsulated in quartz tube backfilled with argon and then solutionized at 900°C for 30 min and water quenched to room temperature; this condition will be hereafter referred to as bulk solutionized (BS) condition. Tensile specimens were machined from samples in the BS condition and the tests for both BS and LENS processed samples were performed at a strain rate of 10^{-3}/s. At least three tensile specimens were tested for each condition, the median values of tensile strength and ductility were reported.

The microstructures for both LENS processed and BS conditions were characterized using a FEI Nova NanoSEM 230, equipped with electron backscattered diffraction (EBSD) and energy dispersive spectroscopy (EDS) detector. OIM^{TM} software was used for generating texture plots from the EBSD data. Further, TEM foils for the selected conditions were prepared inside a FEI Nova 200 Nanolab dual-beam Focused ion beam (FIB/SEM) and were characterized using FEI Tecnai G2 F20 ST S/TEM, a transmission electron microscope (TEM operating at 200 kV) outfitted with a (scanning transmission electron microscopy–energy dispersive spectroscopy) STEM-EDS detector. Atom probe tomography was performed using Cameca LEAP 5000XS

operating at a temperature of 30 K, pulse rate of 200 kHz, and a detection rate of 0.005-0.01 ion/pulse in laser mode with laser pulse energy of 50 nJ. AP Suite 6 software was used to analyze the APT data. The mass spectrum for APT reconstructions was calibrated based on the bulk compositions obtained from SEM-EDS. Multiple APT reconstructions were used to measure the oxygen concentration. The AM processed Ti-185 alloys, reported in the present study, had an oxygen concentration in the range of 0.05- 0.13 wt.% which appears to be similar to that of conventionally processed Ti-185 (wherein the oxygen concentration is reported to be between 0.25 - 0.5 wt.% [7]). H and Ga contamination from APT chamber and FIB have not been indexed in the mass spectrum for comparing chemical composition of different phases. The frequency and radial distribution analysis of select element(s) were obtained from a volume of $30\times30\times40$ nm^3 exported from the original APT reconstruction.

5.2.2 Computational Process Modelling

In order to appraise the thermo-kinetic effects associated with DED-based LENS processed Ti-185, a multi-track multi-layer 3D thermal model was developed using the finite element method with a quiet/active element activation approach on commercial COMSOL Multiphysics® software. The 3D thermal model for LENS process is developed using following assumptions-

1. The thermo-physical properties related to substrate and powder are considered to be isotropic
2. Due to the lack of availability of temperature-dependent thermo-physical properties of Ti-185 in the open literature, its average temperature-dependent thermo-physical properties were considered by considering its constituent elements [64].
3. The powder addition during the deposition process is considered to be homogenous and approximated using a quiet/active element approach [65], in which addition of material is realized by activating a new group of elements at the beginning of new layer fabrication.
4. For the sake of simplicity, melt pool hydrodynamics (melt pool formation and the impact of powder particles on the melt pool) is disregarded in the present model.

The heat transport phenomenon was calculated using the energy conservation equation described below-

$$\rho C_p \frac{\partial T}{\partial t} = \frac{\partial}{\partial x}\left(k\frac{\partial T}{\partial x}\right) + \frac{\partial}{\partial y}\left(k\frac{\partial T}{\partial y}\right) + \frac{\partial}{\partial z}\left(k\frac{\partial T}{\partial z}\right) \quad (1)$$

where ρ is material density (kg/m3), C_p is specific heat (J/kg.K), k is thermal conductivity (W/m.K), and x, y, z are the coordinates in the reference system. The laser beam parameter and optical properties of the material are listed in Table 6. The above equation was solved on a 3D configuration, with the following thermal boundary conditions involving the following details. The heat imparted by the laser beam acts on the top surface, which is considered to be a boundary heat source (heat flux, q_{laser}), thus the thermal boundary condition for the top surface can be surmised by following equation [50].

$$k\left(\frac{\partial T}{\partial n}\right) = q_{laser} - h[T - T_{amb}] - \varepsilon\sigma[T^4 - T_{amb}^4] \quad (2)$$

On the rest of the boundaries, the convective heat transfer between substrate and air is considered by the following equation:

$$k\left(\frac{\partial T}{\partial n}\right) = -h[T - T_{amb}] \quad (3)$$

The initial boundary condition for the entire computational domain is described by the following equation:

$$T_0 = T_{amb} = 293\ K \quad (4)$$

Unlike SLM [150,151]in DED-based LENS process, the powder particles are entrained co-axially along the laser beam over the substrate surface [152]. In light of this, the following aspects are considered in choice of surface heat flux in the present manuscript-

1. Fraction of laser energy is absorbed by the inflight-powder particles and the rest is supplied to the substrate [152,153].
2. For the sake of simplicity, heat transfer due to molten/unmolten particle impact on melt pool has been disregarded.

3. Laser melt pool interaction at the substrate interface can be considered as a surface heat flux owing to sufficiently low optical penetration depth of liquid Ti (≈100 nm) for infrared laser beam (λ=1.06 μm) [154]

Therefore, laser heat flux in LENS process can be described as a boundary heat source according to the following equation [155,156]:

$$q_{laser} = \frac{2Q\eta}{\pi r_l^2} \exp\left(\frac{-2(x-v_s t)^2+y^2}{r_l^2}\right) \quad (5)$$

where Q represents the laser power, η corresponds to the fraction of total laser energy absorbed by the substrate. r_l represents the laser beam radius and v_s is the scanning speed of deposition head. The second term corresponds to convective heat transfer in which h is the heat transfer coefficient and T_{amb} is ambient temperature. The last term represents radiative losses where ε is the emissivity, σ is the Stephen-Boltzmann's constant (5.67×10^{-8} W/m/K^4).

In the present computational model, the element activation method employed a fixed mesh for both the substrate and deposited material for a given layer, in which the mesh elements were initially in-active, which were activated once the material deposition took place [40,157]. The in-active elements were assigned sufficiently low value of thermal properties to suppress heat transfer. The material deposition/activation was tracked through the position of laser beam. Once the laser beam passed through the centroid of a given element, the element was activated and its thermal properties were switched to actual properties of Ti-185. The above process was iterated to felicitate layer by layer fabrication. For the interest of space, additional extensive details regarding the thermal analysis of a multi-track multi-layer AM similar to what was employed in the present work are not included in this manuscript., however such details can be learned from the recent publications of the authors [158–160].

The above equations were solved on a 3D geometrical configuration using the values of the relevant parameters listed in Table 5.1 and with a fixed track length of 6 mm for each of the

experimental parameters mentioned earlier.

Table 5.1: Laser beam parameters and optical properties of the material

Parameters	Values
Laser beam diameter (μm)	500
Laser power (W)	300, 500
Laser scanning speed (mm/s)	12.7
Absorptivity	0.432
Emissivity	0.6
Heat transfer coefficient of air ($W/m^2.K$)	15

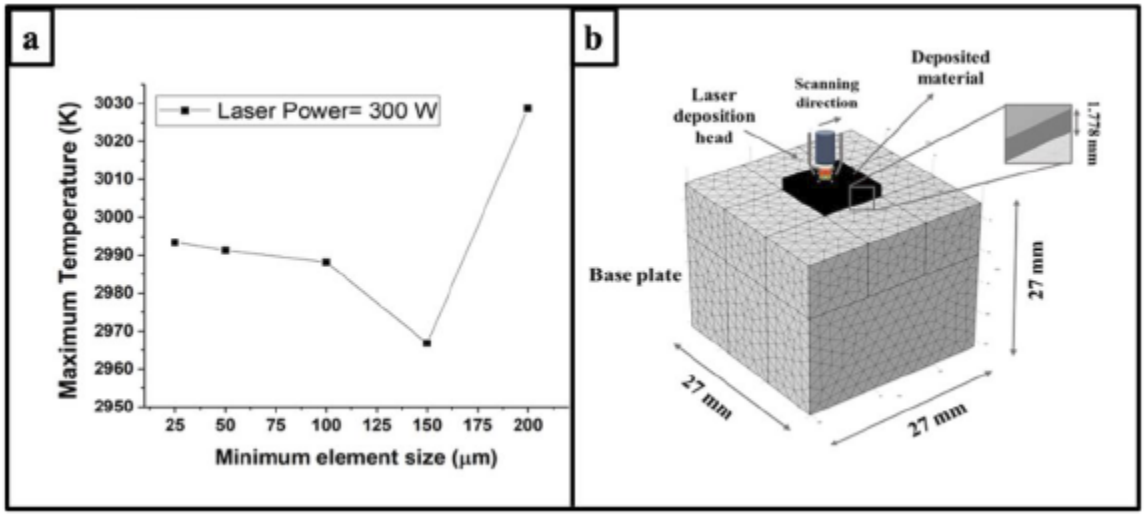

Figure 5.2: (a) Mesh sensitivity of the developed thermal model w.r.t minimum element size (b) meshed computational geometry employed for thermo-kinetic model

Each element in the computational domain was activated after its exposure to the moving laser beam, assuming homogenous layer addition in the DED process. To obtain realistic thermal evolution, the model considers the deposition of 5 tracks up to the 7^{th} layer. The 3D geometry is configured with free tetrahedral meshes with a minimum element size of 50 μm, and a temperature-dependent adaptive meshing approach is employed to maintain the computational time of less than 1 hour. Figure 5.2 illustrates a variation of maximum temperature with increasing minimum element size (Fig. 5.2(a)) along with the image of meshed computational domain (Fig. 5.2(b)). For

minimum element size of 25 and 50 μm, the temperature variation is less than 5K, hence 50 μm mesh size was selected for adequate computational time. The equations were solved using a direct PARADISO solver with relative and absolute tolerance as 10^{-2} and $10^{-4,}$ respectively. The model was computed on an Intel(R) Xeon (R) (Gold 6252 CPU @2.10 GHz-190 GB) processor.

5.3 Results and Discussion

5.3.1 Tensile Properties and Basic Microstructure/Phase Characterization Using SEM and XRD

The engineering stress-strain curves for the various conditions of Ti-185 are shown in Figure 5.3(a). The LENS processed, 300 W condition shows the highest yield strength (YS) of ~1230 MPa followed by 400 W (~1200 MPa) and then the 500 W (~1000 MPa) condition. Besides, all three LENS processed conditions exhibit tensile ductility in the range of 5-7%. For comparison, the same alloy was conventionally processed (cast and homogenized) followed by solution treatment in the single β phase field and water quenched. The tensile properties of this bulk solutionized condition are also shown in Figure 5.3(a), revealing a YS of ~960 MPa similar to the 500 W condition. All the LENS processed samples for different process parameters, exhibited mechanical properties as good as, if not better than the bulk solutionized condition of the conventionally processed Ti-185 alloy.

Low magnification SEM backscatter images of the LENS deposited 300 W and 500 W conditions as well as the BS condition are shown in Figure 5.3 (b), (d) and (f), respectively and the corresponding high magnification images are also shown in Figure 5.3 (c), (e) and (g), respectively. The microstructure in both LENS processed conditions appear to be largely a single (β) phase. No obvious signs of Fe segregation/β flecking are observed in any of these conditions. Further, the high magnification SEM image (Fig. 5.3(c)) shows fine scale (possibly α) precipitates in the grain interiors and a thin wetting layer of these precipitates (possibly α) along the grain

boundaries in case of the 300 W condition, while the microstructure of the 500 W condition (Fig. 5.3(e)) appears to be similar but with negligible amount of (α) phase in the grain interiors. The BS condition exhibits a single (β) phase microstructure (Fig. 5.3(f) and (g)).

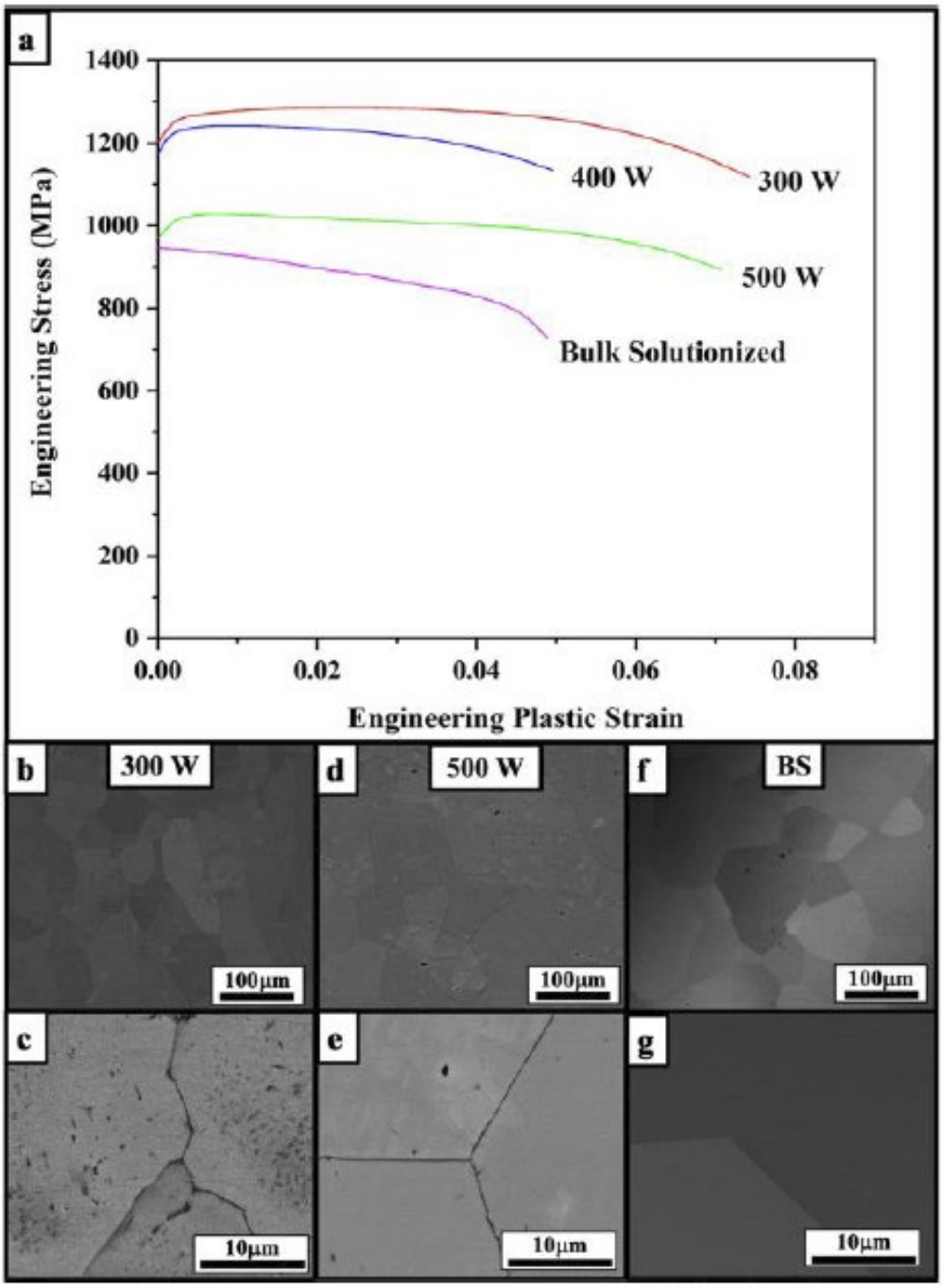

Figure 5.3: (a) Engineering stress-strain curves at room-temperature for the various conditions of Ti-185 alloy. SEM backscattered images showing the microstructures of (b,c) 300 W, (d,e) 500 W and (f,g) Bulk Solutionized (BS) conditions of the same alloy.

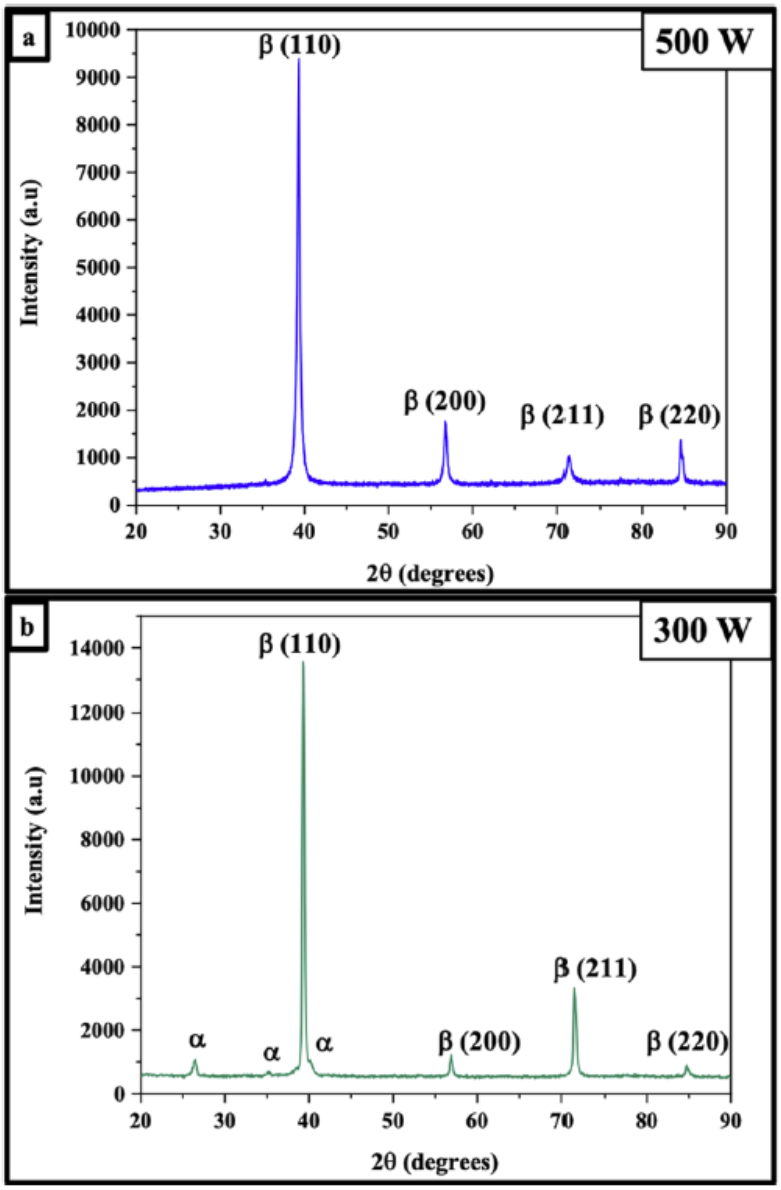

Figure 5.4: XRD patterns that have been acquired with the x-ray beam incident on the plane normal to the deposition/build axis of (a) 500 W and (b) 300 W conditions of LENS manufactured Ti-185 alloy.

X-ray diffraction (XRD) patterns from the 500 W and 300 W samples are shown in Figure. 5.4 (a) and (b) respectively. These XRD patterns have been acquired with the x-ray beam incident on the plane normal to the deposition/build axis of the LENS processed samples. The entire set of XRD peaks observed in case of the 500 W sample, shown in Figure 5.4(a), can be consistently indexed based a single β (BCC) phase. However, in case of the 300 W sample, in addition to the

principal XRD peaks corresponding to the β matrix, there are a number of additional smaller peaks corresponding to the α phase. These XRD results are consistent with the SEM observations. Additionally, it should be noted that the β peaks in both the 500 W and 300 W processed samples, have similar intensity ratios as observed in case of the XRD pattern acquired from the Ti-185 powders, shown in Figure 5.1(c). This establishes that the LENS processed samples do not exhibit any significant β texture.

With the objective of rationalizing the higher yield strength in case of the 300 W condition as compared to the 500 W condition, TEM and atom probe tomography (APT) analysis of both conditions was carried out. Foils for TEM analysis were made from the grip sections of the tensile specimens of both 500 and 300 W conditions and, the results are presented in Figures 5.5 and 5.7.

5.3.2 Detailed Microstructural Characterization of 500W Processed Condition

Figure 5.5(a) shows the selected area diffraction pattern (SADP) corresponding to the 500 W condition. This $[110]_{\beta}$ zone axis pattern clearly shows the presence of characteristic ω reflections at 1/3 and 2/3 $[112]_{\beta}$ locations. These ω reflections are an outcome of the orientation relation (OR) between ω and β, i.e. [2110]ω || [011]β and [0001]ω || [111]β. This is evident from the key figure corresponding to this diffraction pattern shown in (a) of Appendix A. A low magnification (Fig. 5.5(b)) and a high magnification (Fig. 5.5(c)) dark-field TEM image, recorded from the two variants visible in this diffraction pattern, as highlighted with the yellow circle in Figure 5.5(a), revealed the presence of ω precipitates of dimension ~5-10 nm. A high-resolution TEM image is shown in Figure 5.5(d) revealing the atomic scale ω and β structures, and the fully-coherent ω/β interface. The near complete collapse of the adjacent {111}BCC planes within the ω regions is visible similar to previous reports [15,161–164]. While these ω precipitates can form congruently (compositionally invariant with the β parent phase) during the quenching of the alloy,

since the LENS process involves multiple heating-cooling cycles of the same layer, it is likely that these precipitates undergo low temperature annealing, resulting in possible compositional partitioning between the ω precipitates and the β matrix. The possibility of such compositional partitioning between the β and ω phases in the 500 W condition has been investigated via APT. The APT reconstructions shown in Figure 5.6 (a) and (b), reveal a nearly homogeneous distribution of Ti and V atoms/ions, respectively. Additionally, a frequency distribution analysis was carried out by dividing this reconstruction into voxels of 100 ions, and the experimental distribution was compared with a simulated binomial distribution for the Ti ions/atoms, shown in Figure 5.6(c). Additionally, a radial distribution plot (RDF), constructed using Ti ion/atom at the center, shown in Figure 5.6(d), reveals a higher number of Ti-Ti like bonds close to the Ti center. This comparison reveals early stages of partitioning between the β and ω precipitates in the 500 W condition, though it is very difficult to quantitatively estimate the composition difference between these two phases. Based on the sharp change in slope at ~4 nm in radial distribution plot, the size of omega particles can be estimated to be ~8 nm, which is in agreement with the TEM results. This early stage of β/ω compositional partitioning is potentially responsible for the marginally higher tensile yield strength observed in case of the 500 W processed Ti-185 alloy as compared to a β solution treated and water-quenched condition of the same alloy processed via conventional processing (casting plus thermo-mechanical processing), as shown in Figure 5.3(a). Thus, the rejection of β stabilizing elements, such as V and Fe from the ω precipitates, could potentially lead to an increase in the elastic modulus and strength of these precipitates, leading to higher yield strength of the alloy. Such effects have been the subject of discussion in multiple recent publications on other β Ti alloys [165].

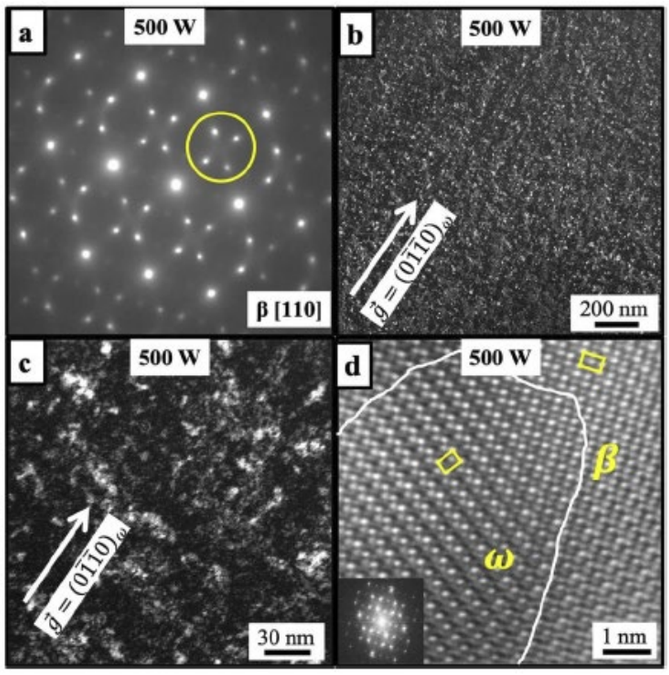

Figure 5.5: TEM of 500 W condition: (a) Selected area diffraction pattern (SADP) obtained via $[110]_\beta$ zone axis showing the presence of characteristic ω reflections at 1/3 and 2/3 $[112]_\beta$ locations. (b) Low magnification and (c) high magnification dark-field TEM images, recorded

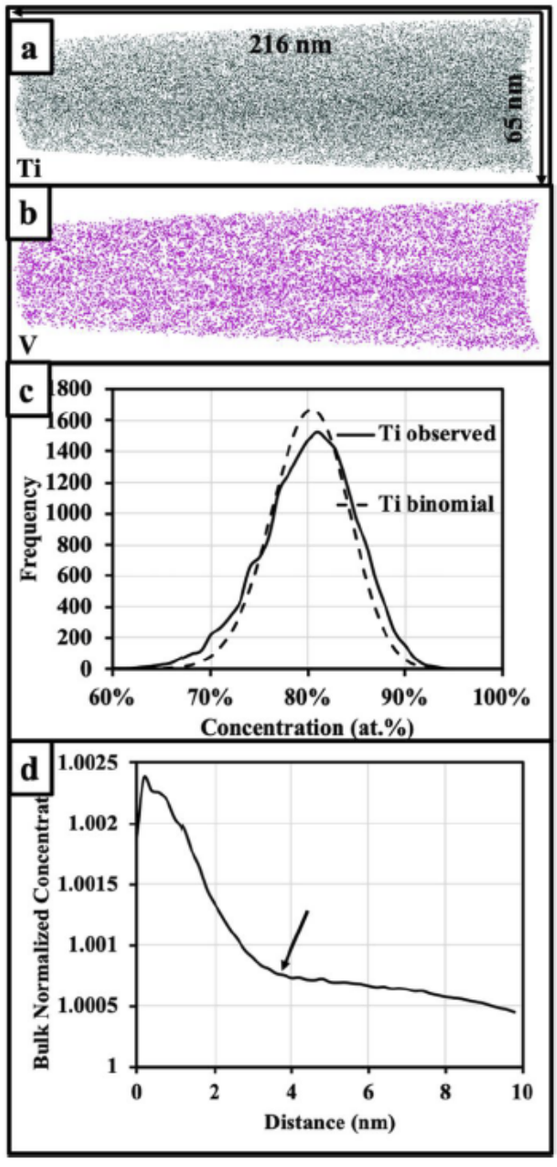

Figure 5.6: APT of 500 W condition: (a) Ti ion map (b) V ion map (c) Frequency distribution analysis of Ti comparing the observed distribution with binomial (d) Bulk normalized concentration vs distance plot for Ti, obtained using radial distribution function.

5.3.3 Detailed Microstructural Characterization of 300 W Processed Condition

Figure 5.7(a) shows a $[110]_{\beta}$ zone axis selected area diffraction pattern from the 300 W condition. Unlike the case of 500 W condition, the additional spots in this diffraction pattern do not lie along the 1/3 and 2/3 $[112]_{\beta}$ locations, and therefore do not correspond to ω precipitates. Rather these additional reflections correspond to multiple variants of α precipitates and attendant double diffraction effects. This is evident from the key figure corresponding to this diffraction pattern shown in (b) of Appendix A. A dark-field image shown in Figure 5.7(b), recorded from the set of reflections outline in Figure 5.7(a), clearly reveal the presence of fine scale α precipitates within this microstructure. These fine scale α precipitates are ~500 nm -1 μm in size. The expected Burgers orientation relationship, between α and β phases, [0001]α || [011]β and [1120]α || [111]β can be confirmed by the diffraction pattern shown in Figure 5.7(a). High-resolution TEM images of this microstructure are shown in Figure 5.7 (c), (d) and (e). Figure 5.7(c) shows the atomic structure of the α/β interface recorded along the [0001]α || [011]β viewing axis. Characteristic atomic scale ledges or steps are clearly visible along this interface, similar to those reported in case of these interfaces in other conventionally processed metastable β Ti alloys, such as Ti-5Al-5V-5Mo-3Cr (or Ti-5553)[166–169]. The atomic structure within the BCC β matrix, viewed along the [111] direction is shown in Figure 5.7(d), while the atomic structure of the HCP α phase, viewed along the [0001] direction is shown in Figure 5.7(e). The bright field TEM image, shown in Figure 5.7(f), captures a prior β grain boundary decorated with coarser grain boundary α precipitates (or allotriomorphs) and uniformly distributed finer scale α precipitates within the grains. The compositional partitioning between the α precipitates and the β matrix is shown via HAADF-STEM EDS maps in Figure 5.7(g). These maps clearly show that the α precipitates which are

largely depleted in both Fe and V, but only marginally enriched in Al.

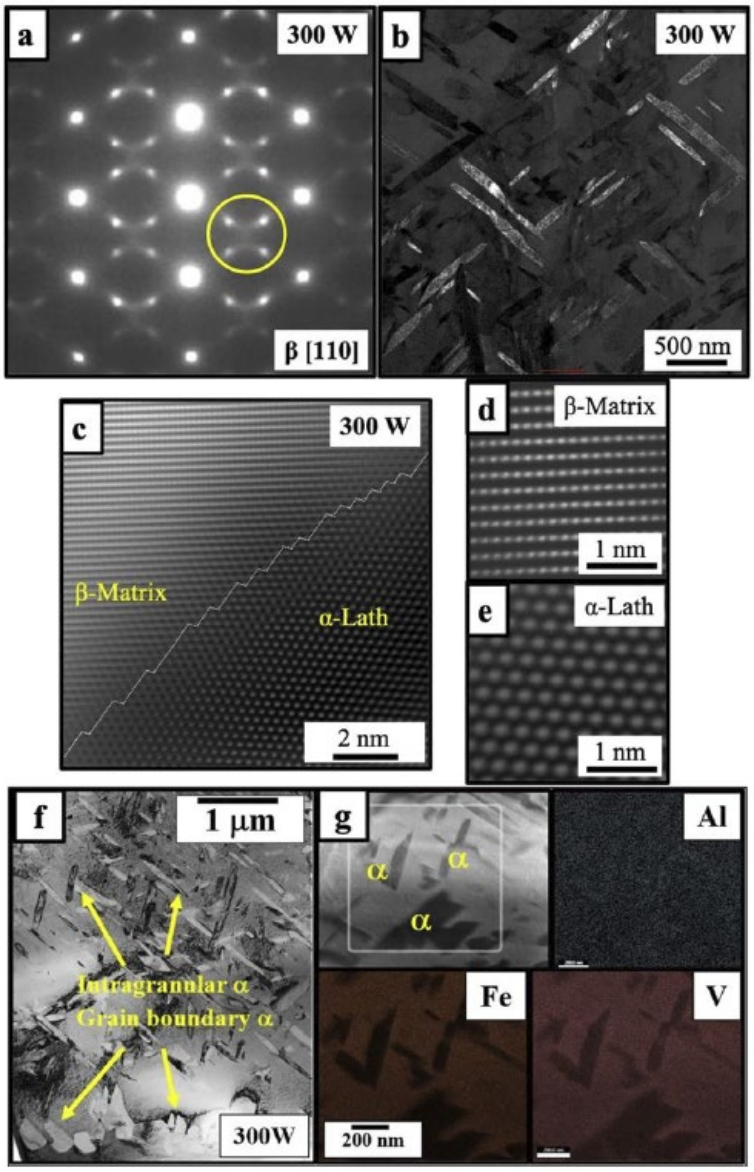

Figure 5.7: TEM of 300 W condition: (a) Selected area diffraction pattern (SADP) obtained via $[110]_{\beta}$ zone axis showing the presence of characteristic α reflections. (b) Dark-field image recorded from the set of reflections highlighted with yellow circle in (a). (c) High Resolution TEM image showing the atomic structure of the α/β interface recorded along the [0001]α || [011]β viewing axis. HR-TEM image showing the atomic structure within the (d) BCC β matrix, viewed along the [111] direction and within (e) HCP α phase, viewed along the [0001] direction. (f) Bright field TEM image and (g) HAADF-STEM EDS maps showing compositional partitioning between α precipitates and the β matrix.

Detailed APT analysis has been carried out on samples extracted from the 300 W condition, and the results are shown in Figure 5.8. Figure 5.8(a) shows a relatively higher magnification dark-

field TEM image, recorded using an α reflection in the diffraction pattern, and shows two distinct variants of α plates. Figure 5.8 (b) and (c) show high magnification views of sections of Figure 5.8(a), with two different boxes highlighted in these images. The box marked A in Figure 5.8(b) shows a broad face of an α plate in close proximity of the corner of a second α plate, while the box marked B in Figure 5.8(c) highlights the corner of another α plate with large ledges. Figure 5.8(d) shows an APT reconstruction capturing sections of two fine scale intra-granular α precipitates, which have been delineated with isoconcentration surfaces (or isosurfaces) constructed for V = 5 at%. This APT reconstruction appears to be quite similar to the region marked by box B in the TEM dark-field TEM image shown in Figure 5.8(b). The compositional profiles for V, Fe, Al, Si, and O, across the α/β interface on the left side of the reconstruction, corresponding to the broad face of the α plate, have been plotted as a proximity histogram (or proxigram) [170] in Figure 5.8(e). A second APT reconstruction is shown in Figure 5.8(f) reveals the corner of an α plate with large ledges, quite similar to the box marked B in the dark-field TEM image shown in Figure 5.8(c). The corresponding proxigrams for V, Fe, Al, Si, and O, across this α/β interface are shown in Figure 5.8(g).

Interestingly, there is a substantial difference in the local β compositions, adjacent to the α/β interfaces in case of both APT reconstructions. Thus, while the local V content in the β phase, adjacent to the α/β interface, for the broad face of the α plate (shown in Fig. 5.8 (d) and (e)) is approximately 13at% V, the same value in case of the corner of the α plate (shown in Fig. 5.8(f) and (g)) is approximately 10at% V. This large difference in the local equilibrium V content in the β phase can be rationalized based on the Gibb-Thompson effect, or the capillarity effect, arising from the small radius of curvature at the corner of the α plate. This effect can be easily visualized

by considering the schematic shown in Figure 5.9, depicting the free energy versus composition (G-X) plots for the β and α phases.

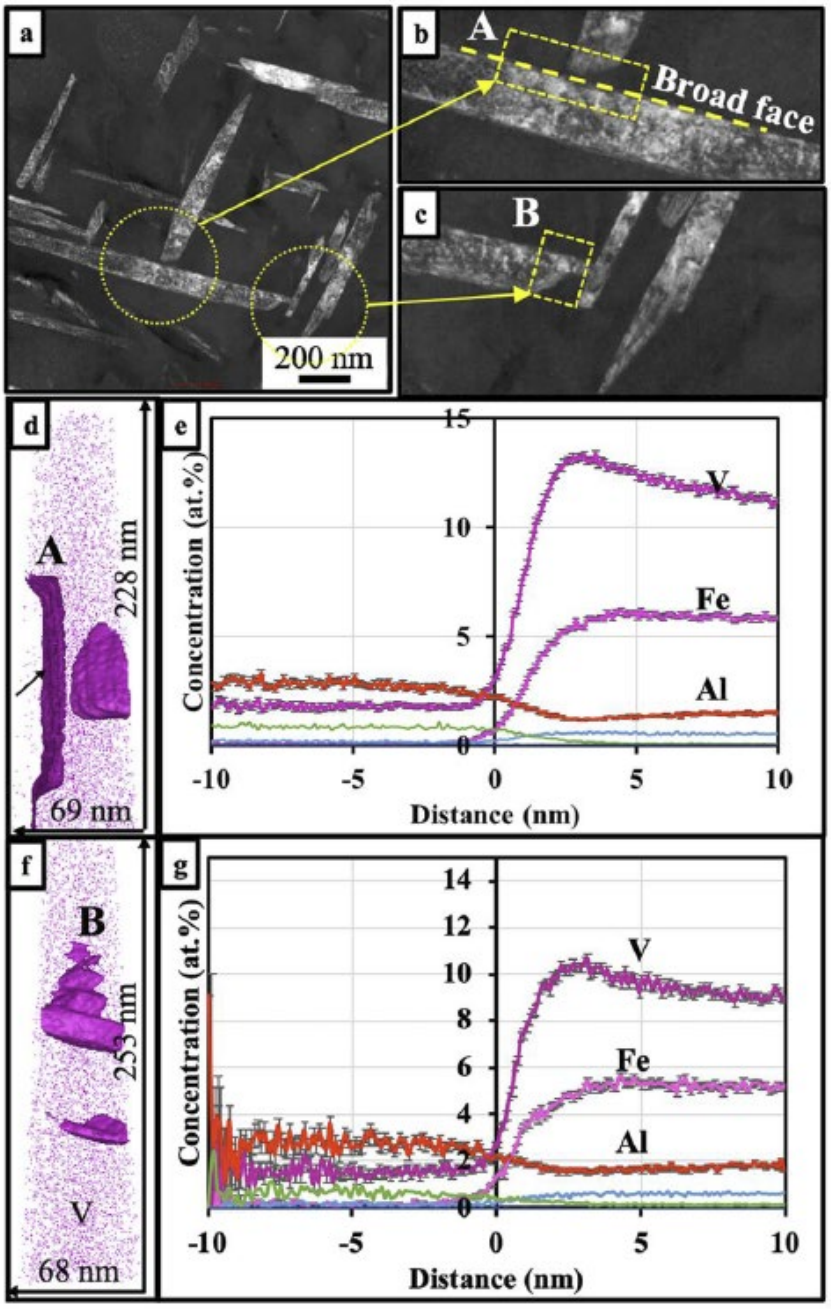

Figure 5.8: TEM and APT of 300 W condition: (a) Dark-field micrograph showing alpha laths in the beta matrix. High magnification dark-field micrographs showing the (b) broad face and (c) ledges at the corner of alpha laths (d) V 5 at.% iso-concentration surface with V ions showing the broad face of an alpha lath (indicated by black arrow). (e) Proxigram constructed across V 5 at.% iso-surface in (d). (f) V 4.3 at.% iso-surface with V ions showing the ledges at the corner of an alpha lath (g) Proxigram constructed across V 4.3 at.% iso-surface in (f).

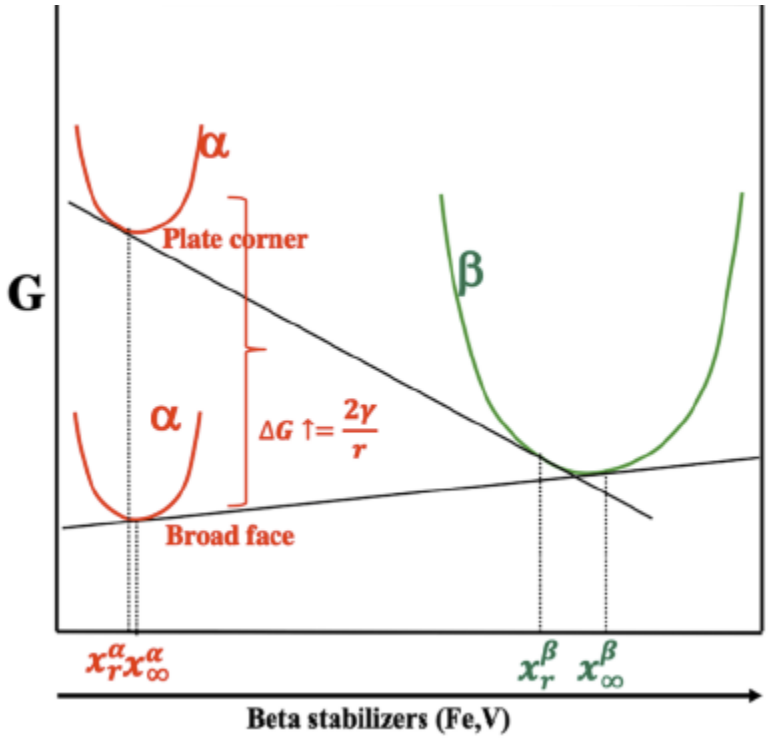

Figure 5.9: Schematic of G-X plots for α and β phases showing the Gibb-Thompson effect.

These schematic plots have been depicted with increasing content of β stabilizers (V and Fe in this case) along the X-axis. This, the β G-X plot is to the right with respect to the α G-X plots. There are two α G-X plots in this figure, with the lower curve corresponding to the broad face of the α plate and the upper plot corresponding to the corner of the α plate, which has a much smaller radius of curvature. The common tangents for both the α G-X plots and the β G-X plots have also been shown in Figure 5.9. Based on the points of common tangency, where the tangent touches the G-X plot, it is evident that the composition of β matrix in local equilibrium with the broad face of the α plate, is substantially enriched in β stabilizer content, as compared to the matrix in local equilibrium with the corner of the α plate. This explains the experimentally observed higher V content in the β matrix in local equilibrium with the broad face of the plate, as compared to the corner of the plate.

5.3.4 Rationale for Precipitation of α Plates in Case of the 300 W Processed Condition: Multi-Physics Modeling

As mentioned earlier, the fine-scale α phase precipitation was detected in the grain interiors of Ti-185 deposited at 300 W, whereas it was hardly exhibited by the sample deposited at 500 W (Figs. 5.3 and 5.4). This discrepancy was analyzed using a thermokinetic model presented earlier, which predicted the temporal and spatial distribution of temperature during DED fabrication. A location lying in the first laser track of first layer was probed for its temperature variation during the fabrication of the sample with multiple laser track deposition in each layer. Corresponding thermal history consisting of multiple thermal cycles at a given location is presented in Figure 5.10 (a) and (b) at laser power 300 W and 500 W, respectively. Under a given process-inherent thermal cycle treatment, the probed location melts (at 1580°C predicted using PANDAT^{TM} software) during fabrication of the first layer and does not remelt during successive thermal cycles. The peak temperature of the probed location (thermal cycle C1) during deposition of the first track of second layer reaches above the β transition temperature (737°C predicted using PANDAT^{TM} software) and again during fabrication of the first track of third layer (thermal cycle C2). The probed location during a cooling event of thermal cycle C2 experiences a cooling rate of 831°C/s and temperature drops to minimum 264°C before the next thermal cycle. Such thermokinetics is likely to cause the nucleation of the α phase in the interiors of β as the temperature, thereafter, oscillates around 350 °C during the fabrication of successive layers. On the other hand, the same probed location during fabrication at 500 W, reached β transition at several thermal cycles until fabrication of the 6th layer (Fig. 5.10(b)), which might have caused frequent precipitation and dissolution of α precipitates. In addition, during fabrication of the 7th layer, the temperature fluctuated around 650°C, and considering the heat accumulation effect seen with the thermal cycle (Fig. 5.10(b)), it is likely to retain a reduced fraction of α precipitates in 500 W, as seen earlier in

Figures 5.3(e) and 5.4(b).

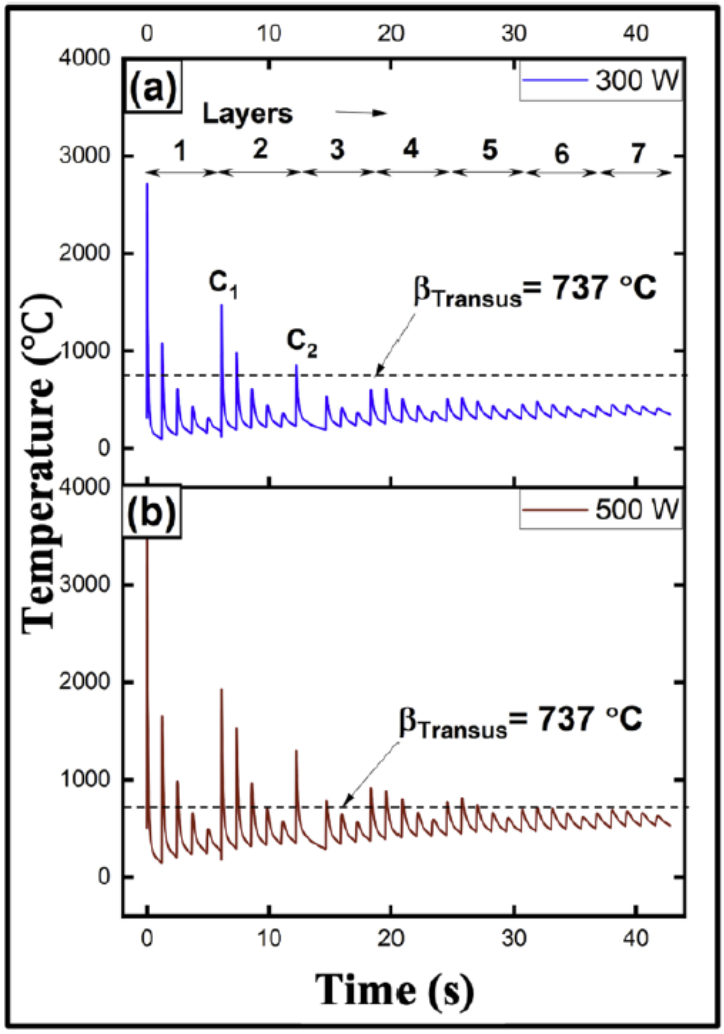

Figure 5.10: Thermal history consisting of multiple thermal cycles at a given location analyzed using a thermokinetic model for (a) 300 W and (b) 500 W condition of LENS manufactured Ti-185 alloy.

5.3.5 Origin of Higher Yield Stress in 300 W Processed Condition and Deformation Mechanisms

The higher YS observed in 300 W condition, as compared to the 500 W condition, can be primarily attributed to the presence of fine scale α precipitates in the 300 W condition. A TEM sample was extracted from the tensile tested Ti-185 300 W condition and the results are shown in Figure 5.11. The origin of this higher yield strength is a Hall-Petch type strengthening by α plates/laths which result in a shorter slip-length and hence dislocation pile-up at the alpha/beta

interface. The back-stress originating from such a pileup requires a higher resolved stress along the primary slip plane for continuing glide of dislocations, which translates into a higher yield strength. The commonly observed slip systems in these alloys are {110}β, {113}β and {123}β, all with ⟨111⟩β type burger vector. In the present case, a TEM sample was extracted from the Ti-185 300 W condition, tensile tested to fracture. A dark-field TEM image from this sample is shown in Figure 5.11(a) with a higher magnification image in Figure 5.11(b). Both these images indicate homogenous dislocation activity within the β matrix. Since the foil has been prepared from a fractured sample, considerable dislocation activity is evident. At this level of plastic strain, some dislocation activity within the α plates/laths is also evident, which is shown by a dark-field TEM image from one such plate, in Figure 5.11(d).

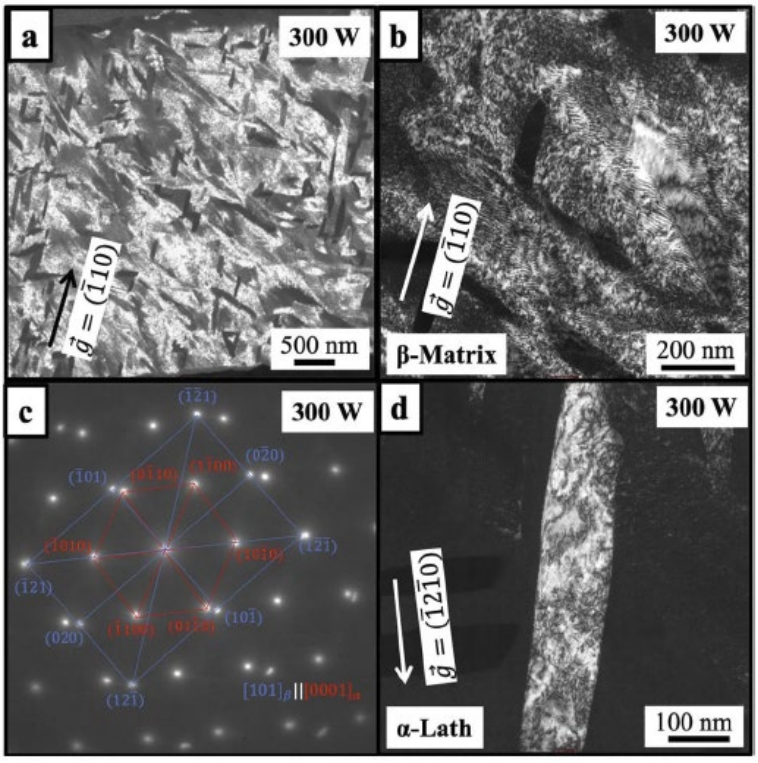

Figure 5.11: TEM of tensile tested 300 W condition: (a) Low magnification and (b) High magnification dark-field TEM images indicating homogenous dislocation activity within the β matrix. (c) Diffraction pattern showing orientation relationship between Beta matrix and alpha precipitates, $[110]_\beta \| [0001]_\alpha$. (d) High magnification dark-field TEM image showing the dislocation activity within the α plates/laths.

5.4 Conclusions

The directed energy deposition based LENS process was employed to successfully deposit a metastable β-Ti alloy prone to beta fleck effect, Ti-185, with three different deposition powers. The as-processed Ti-185 alloy did not exhibit any Fe segregation/β flecking for all three deposition powers. Besides, the as-processed conditions, exhibited very good tensile properties better than the conventionally cast/forged and solutionized counterparts. The key points of this paper have been briefly summarized below:

1. LENS processed Ti-185 exhibits a fine-grained equiaxed microstructure for a range of deposition powers (energy densities) which can be rationalized based on the alloy's large solidification range as compared to other Ti-V based alloys with smaller solidification ranges, exhibiting strongly developed columnar grains.

2. The size of the equiaxed β grains can be tuned via the LENS/AM process parameters, with lower laser power (or energy density) promoting finer scale grains as compared to higher powers.

3. Using a lower laser power (300 W) or energy density (47.24 J/mm^2), leads to fine scale intra-granular α precipitation within the equiaxed β grains, while a higher laser power (500 W) or energy density (78.74 J/mm^2) results in ω formation within the equiaxed β grains. This is a direct demonstration of the ability to tune α or ω precipitation within the grains of β Ti alloys, via systematic variations in the AM process parameters.

4. The ω precipitates forming in the 500 W condition are fully coherent with the β matrix and exhibit early stages of compositional partitioning with respect to the matrix. The fine scale α plates/laths forming in case of the 300 W condition are nanometer in size scale, homogeneously distributed, and exhibit a Burgers orientation relationship with the β matrix grains. Atomic scale

ledges are clearly visible at the β/α interfaces. Interestingly, both STEM-EDS as well as APT results indicate that while the α plates reject a substantial amount of V and Fe, there is a much lower degree of Al enrichment within these plates. Additionally, the APT results also revealed, for the first time, the influence of the Gibbs-Thompson effect (local curvature at the β/α interfaces) on the local equilibrium near the interface. Thus, the local V content within the β matrix, adjacent to the broad face of an α plate/lath was significantly higher as compared to the local V content adjacent to the corner of an α plate/lath.

5. The influence of process parameters on the nature of second phase formation within the β matrix grains, α or ω, has been rationalized using a multi-physics thermo-kinetic model which predicts the multiple heating-cooling cycles experienced by the layers during the LENS deposition.

6. The refined precipitation of α plates/laths within the equiaxed β grains result in a substantial enhancement in the yield and ultimate tensile strengths of the as-processed alloy, with the yield stress exceeding 1.2 GPa. The deformation microstructure reveals a high density of homogenous dislocation activity within the β matrix and some limited activity within the α plates/laths.

Overall, the results indicate that Ti-185 is a promising β Ti alloy for AM processing. Further, the results demonstrate the ability to tune the microstructure via changes in the process parameters, to achieve desirable tensile properties, obviating the need for any secondary post processing.

CHAPTER 6

ADDITIVE MANUFACTURING OF COMMERCIAL BETA TITANIUM ALLOY: Ti-10V-2Fe-3Al*

6.1 Introduction

Traditionally Ti alloys have been known for their high specific yield strengths, but rather poor strain hardenability and uniform elongation [7,14]. This has been well-established for both α/β Ti alloys such as Ti-6Al-4V as well as metastable β alloys, such as Ti-5Al-5V-5Mo-3Cr (with an α+β microstructure) [171,172]. Recently, a number of metastable β-Ti alloys have been developed that exhibit high strain hardenability and uniform elongation attributable to deformation or strain-induced twinning or martensite formation also referred to as twinning induced plasticity (TWIP) and/or transformation induced plasticity (TRIP), versus traditional deformation via slip [165,173–178]. As an example, the commercially available Ti-10V-2Fe-3Al (wt.%) (hereon referred to as Ti-10-2-3) alloy falls under the category of strain transformable β-Ti alloys exhibiting TRIP/TWIP effects [179]. Invariably, these strain-transformable β-Ti alloys suffer from rather low yield strengths. Similarly, low modulus β-Ti alloys used for biomedical applications also suffer from low yield strengths [112,171]. Therefore, there is a need for the compositional and microstructural design of Ti alloys with higher yield strength while maintaining their strain-transformable attributes. The other major advantages of using β-Ti alloys are their tunable nature, wherein, the microstructure and subsequently mechanical behavior can be altered by varying the thermo-mechanical processing. By controlling the secondary precipitate phases like omega or

* This chapter is partly reproduced from S.A. Mantri, M.S.K.K.Y. Nartu, S. Dasari, A. Sharma, P. Agrawal, R. Salloom, F. Sun, E. Ivanov, K. Cho, B. McWilliams, S.G. Srinivasan, N.B. Dahotre, F. Prima, R. Banerjee, Suppression and reactivation of transformation and twinning induced plasticity in laser powder bed fusion additively manufactured Ti-10V-2Fe-3Al, Addit. Manuf. 48 (2021) 102406, https://doi.org/https://doi.org/10.1016/j.addma.2021.102406, with permission from Elsevier.

alpha, within the parent β-matrix, including their shape, size, and morphology a wide range of mechanical properties can be achieved [112,180–182].

While metal additive manufacturing (AM) has been extensively used for processing α/β Ti alloys, such as Ti-6Al-4V, there are relatively fewer investigations on AM processing of metastable β Ti alloys which have been attracting some recent attention [183–187]. While Ti-6Al-4V is an excellent alloy for many applications, there is a need to explore new titanium alloy systems, especially β-Ti alloys, in order to exploit the unique advantages which AM offers over conventional casting techniques; such advantages include faster cooling rates and complex multiple heating/cooling cycles [74,188]. Faster cooling leads to higher solidification rates which can then be exploited to process alloys which have been traditionally difficult to cast into typical ingots due to segregation problems. These include a class of β-Ti alloys, more specifically systems containing β-eutectoid elements such as Fe and Cu, that lead to solute-segregation issues commonly referred to as the "beta fleck" problem [1,32,171]. Recent literature on this has shown that the higher cooling rates obtained via AM processing can successfully overcome this issue [124,125,186,189].

Conventionally processed Ti-10-2-3 alloy provides an excellent combination of deep hardenability, good strength and ductility, and fracture toughness relative to Ti-6Al-4V and has therefore been one of the most widely used β-titanium alloys in the aerospace industry [171]. There have been reports of micro-segregation due to the presence of Fe in this system, which could possibly lead to property variability. As mentioned before, the higher cooling rates accessible during AM processing is a potential solution to the problem of "beta fleck" and has been recently demonstrated [189–191]. Early work by Duerig et al [179] provided the groundwork in understanding the mechanical behavior and phase transformations of conventionally processed Ti-

10-2-3 alloy. The presence of orthorhombic stress induced martensite (SIM) was noted in their work, which has since been confirmed by other researchers [176,192]. More recent studies focused on understanding the various factors influencing the formation of the SIM in this alloy [193–195]. While there have been a few previous studies on AM processed Ti-10-2-3 [190,196], they are very limited in addressing transformation-induced plasticity. The present work on additive manufacturing of the Ti-10-2-3 alloy, focuses on the influence of laser additive processing on the evolution of the β+ω/β+α microstructures, their attendant impact on deformation behavior, and an approach to recover the TRIP/TWIP effects and strain hardenability in the AM processed alloys via a β-solution treatment. Additionally, the microstructure and mechanical properties of the conventionally manufactured counterparts, i.e., As-received and As-received + β-solutionized conditions, are investigated to compare and contrast with the additively manufactured Ti-10-2-3.

6.2 Experimental Procedure

6.2.1 As Received Alloy

The conventionally processed Ti-10-2-3 was obtained from ATI corporation (will be hereon referred to as "As-received (AR) condition") for comparing the microstructures and mechanical properties with the additively manufactured counterparts. Two bars of dimensions 20 mm length, 8 mm width, and about 3 mm height were sectioned from the material. One of the two bars was β-solution annealed at 900°C for 30 min and then quenched in water; this condition will be hereafter referred to as "AR + β-solutionized condition." Mini tensile specimens of 5 mm gauge length and 1 mm gauge width were machined using KENT USA (WSI-200) EDM from both the conditions (AR and AR + β-solutionized) and uniaxial tensile tests were performed at a strain rate of 10^{-3}/s. At least three tensile specimens were tested for each condition, and the median values of tensile strength and ductility are reported. Samples from these conditions, i.e., grip sections of

tensile specimens, were polished to an average surface finish of 0.02 μm for microstructural analysis. Imaging and Electron backscatter diffraction (EBSD) analysis was performed in an FEI-Quanta Nova-Nano SEM 230. OIM^{TM} software was used to produce the inverse pole figure (IPF) maps and Phase maps from the EBSD scans.

6.2.2 Laser Engineered Net Shaping ^{TM} (LENS)

An Optomec LENS-750 was used for fabricating Ti-10-2-3 on a Ti-64 seed plate. In order to eliminate the problem of compositional differences arising due to elemental powder blends, pre-alloyed, gas atomized Ti-10V-2Fe-3Al (wt. %) obtained from Tosoh SMD Inc. The average powder size for this process was between 15-45 um. A 1500 W Nd: YAG laser that produces near-infrared radiation at a wavelength of 1.064 μm was used for the deposition. Two different laser powers, i.e., 400 & 500 W, were used for the fabrication. The other processing parameters were unchanged: 0.5 mm laser beam on the sample surface; 12.7mm/s laser scan speed; 0.254 mm vertical layer spacing; 0.381 mm hatch width with 90° rotation in the hatch direction between layers. These combinations of laser parameters provided input energy densities of 62.99 J/mm^2 & 78.74 J/mm^2 to fabricate blocks of dimensions of 25.4 mm x25.4 mm x25.4 mm. The oxygen level in the glove box was maintained below ten ppm during the deposition of the alloys.

The deposited builds were then separated from the seed plate and subsequently sliced into two sections along the build direction using a KENT USA (WSI-200) electric discharge machine (EDM). One of the sections was utilized for machining specimens (perpendicular to the build direction) for tensile property measurements, and the other section was used for microstructural analysis. The dimensions of the tensile specimens were: gauge length ~ 5 mm, width ~ 1 mm, and thickness ~ 0.7–1 mm. Uniaxial tensile tests for both 400 and 500 W LENS processed Ti-10-2-3 were performed at a strain rate of 10^{-3}/s. At least three tensile specimens were tested for each

condition, the median values of tensile strength and ductility were reported. Imaging for the LENS processed Ti-10-2-3 samples was performed in an FEI-Quanta Nova-Nano SEM 230.

6.2.3 Selective Laser Melting

A powder bed fusion (PBF) system, AconityMIDI, equipped with a 1KW laser, was used to print an 18 mm* 18 mm*18 mm cube. The same pre-alloyed powders procured from TOSOH, SMD Inc. were utilized for the SLM fabrication of Ti-10-2-3. An island scan strategy was employed with a laser power of 150W and a scan speed of 800mm/sec, with a hatch width of 60 microns and layer thickness of 30 microns. A continuous flow of Ar (30 lpm) was deployed into the process chamber in order to maintain the O2 level below 10ppm.

Following the fabrication, the build was sectioned into two parts using KENT USA (WSI-200) EDM. One of the samples was solutionized at 900 ºC/30 min, and then water quenched. Phase analyses via X-ray diffraction were done using a Rigaku Ultima III X-ray diffractometer for the samples, both before and after the deformation. An FEI Nova NanoSEM, coupled with an Energy Dispersive Spectroscopy (EDS) and a Hikari Super Electron Backscattered Diffraction (EBSD) detector, was used for scanning electron microscopy and composition analyses. Site-specific samples for TEM analyses were prepared using an FEI Nova NanoLab 200^{TM} focused ion beam (FIB). Transmission electron microscopy (TEM) was carried out in an FEI Tecnai F20-FEG TEM operated at 200 kV. EM-based OIM - PED was carried out using a NanoMEGAS system. The parameters were set at C2 aperture of 30 µm, the spot size of around 2 nm (spot size of 8 on the FEI system), camera length of 135 mm and step size of 10 nm. The data acquired using TOPSPIN 3.0 software was analyzed by ACOM software. In addition, nanometer-scale compositional analysis of the same samples was done using a 5000XS Camera LEAP 3D atom probe tomography (APT) operated at 30K with a pulse fraction of 20% and a detection rate of 0.5 in Laser mode.

Tensile specimens were extracted from both the as-fabricated (AF) and solutionized (AF + β-solutionized) plates, perpendicular to the build direction. The tensile tests were performed under uniaxial tension at a strain of 10^{-3}/sec. A custom-built mini-tensile machine with an LVDT (linear variable displacement transformer) extensometer was employed for strain measurements. The tensile samples had a gauge length of 5mm and cross-section of 1.25mm*1.25mm. For each condition, a total of three specimens were strained to failure, following which fracture analyses were performed on the deformed surfaces.

6.3 Results and Discussion

6.3.1 Microstructure and Mechanical Properties of Conventionally Processed Ti-10-2-3 Alloy

The low magnification and high magnification SEM backscatter images from the As-received (AR) and As-received + β-solutionized (AR+ β-soln) conditions are presented in Figure. 6.1 (a & b) and (c & d), respectively. The As-received (AR) condition exhibits a dual-phase α+β microstructure (Fig. 6.1 (a) and (b)), with two different morphologies for the alpha precipitates (equiaxed and lath-like). However, the wavy and irregular α/β interfaces (outlined with a yellow circle in Figure 6.1(b)) instead of straight interfaces possibly indicate that the lath-like morphology in the coarser precipitates is an outcome of coarsening followed by coalescence of the equiaxed alpha precipitates. The dissolution of the alpha precipitates, i.e., a single-phase (β) microstructure, can be observed after β–solutionizing heat treatment, as shown in Figure 6.1(c) and (d).

The engineering stress versus plastic strain curves for the AR and AR+ β-soln conditions are shown in Figure 6.2. The as-received (AR) condition exhibits a YS of 960 MPa, significantly higher than 500 MPa revealed by the As-received + β-solutionized (AR+ β-soln) condition. The remarkably higher YS observed in the AR condition compared to the AR+ β-soln condition could

be mainly due to the presence of α precipitates (within the β matrix) in the former condition.

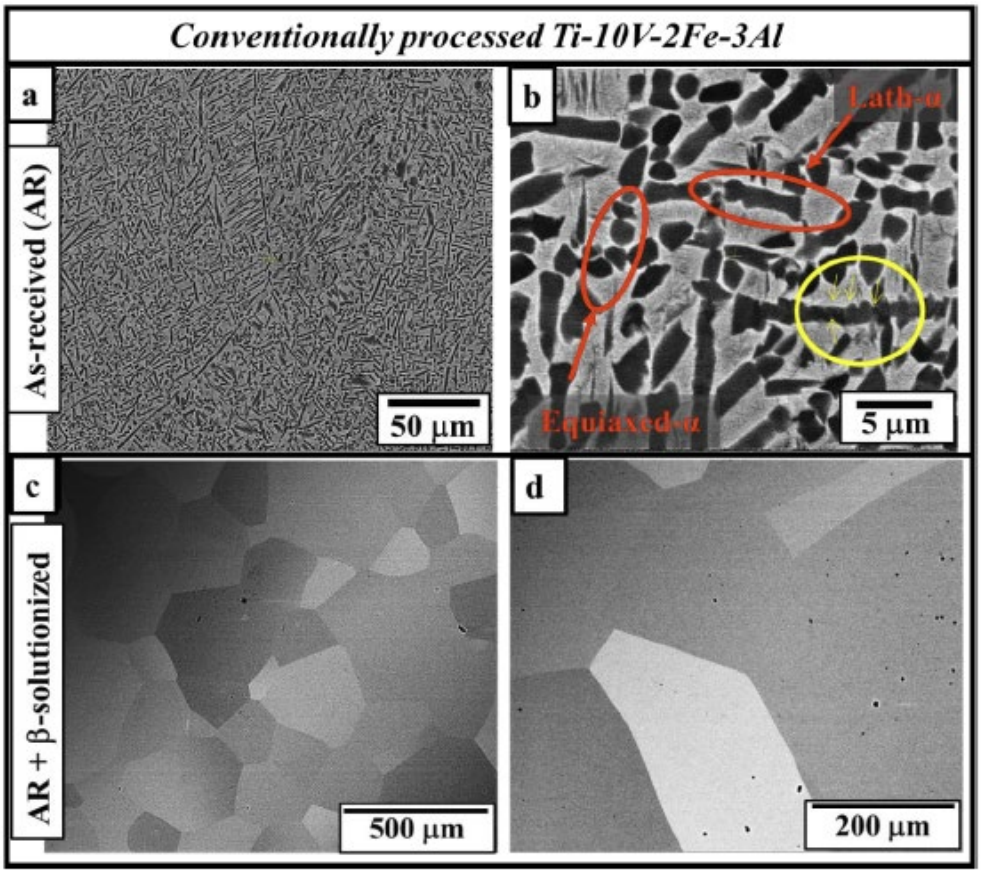

Figure 6.1: The Low and High magnification SEM backscatter images for (a,b) As-received (AR) and (c,d) As-received and b-solutionized (AR+ b-soln) Ti-10-2-3

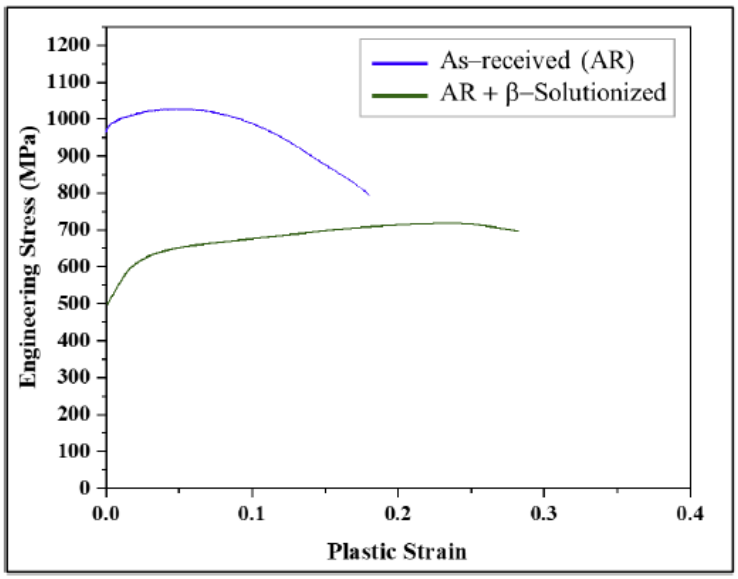

Figure 6.2: Engineering stress versus plastic strain curves for conventionally processed Ti-10-2-3

This could also be why the significantly lower ductility (~17%) was observed in the AR condition. Further, the AR+ β-soln condition exhibits a noticeably higher strain hardening, σ_{UTS} - σ_{YS} of 220 MPa, compared to 75 MPa shown by the AR condition. The discrepancy in the strain hardening behavior between the two conditions is analyzed by investigating the post-tensile-deformation microstructures. EBSD analysis was performed on the gauge sections of the tensile samples; the IPF and corresponding phase maps obtained for AR and AR+ β-soln conditions are represented in Figure 6.3 (a & b) and (c & d), respectively. While there was no indication of stress-induced martensite (SIM, α") [197,198] formation in the AR condition (Fig. 6.3(b)), there is a substantial formation of SIM (α") in the AR+ β-soln condition (Fig. 6.3(d)), based on these phase maps. This observation is not unusual since Ti-10-2-3 with a single β phase is expected to exhibit stress-induced martensitic transformation and TRIP effects, based on multiple previous reports on conventionally processed alloys [179,199,200].

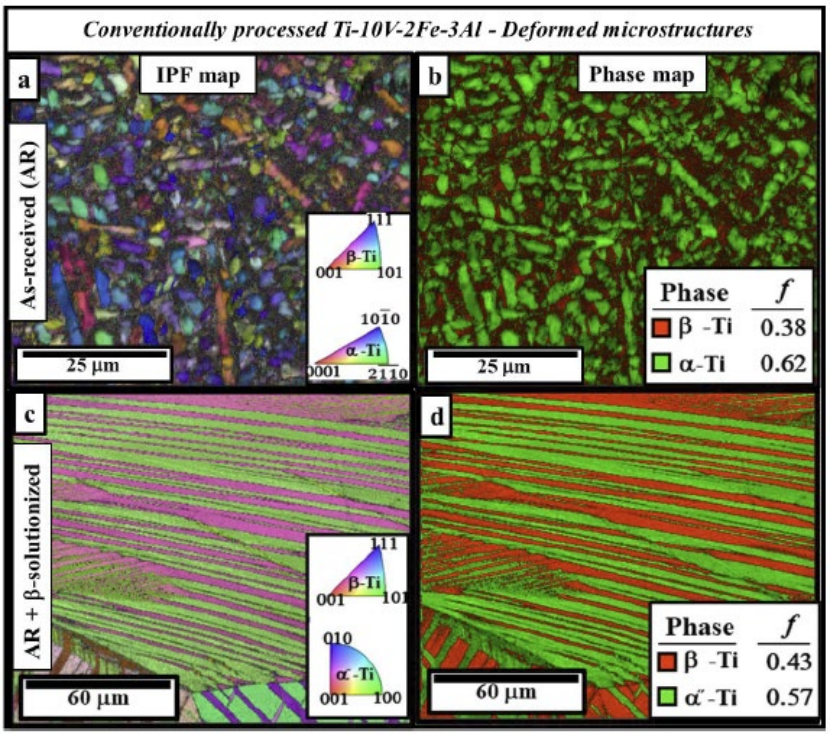

Figure 6.3: The IPF and corresponding phase maps obtained for (a,b) As-received (AR) and (c,d) As-received + b-solutionized (AR +b-soln) conditions of conventionally processed Ti-10-2-3

6.3.2 Microstructure and Mechanical Properties of LENS Processed Ti-10-2-3 Alloy

The low and high magnification SEM backscatter images from the 400 W and 500 W conditions of the LENS processed Ti-10-2-3 are presented in Figure 6.4 (a & b) and (c & d), respectively. Both the conditions exhibit fine-scale α precipitates along the β–grain boundaries and also within the β–grain interiors. The α precipitates in the 400 W sample appear to be substantially coarser than 500 W condition. However, irrespective of the laser power employed, the LENS processed Ti-10-2-3 exhibited significantly finer (α) precipitates than the conventionally processed, As-received (AR) condition (Fig. 6.1 (b)). Further, the LENS processed conditions exhibited true lath/plate-like morphology for the α precipitates, while the As-received (AR) condition exhibited equiaxed morphology.

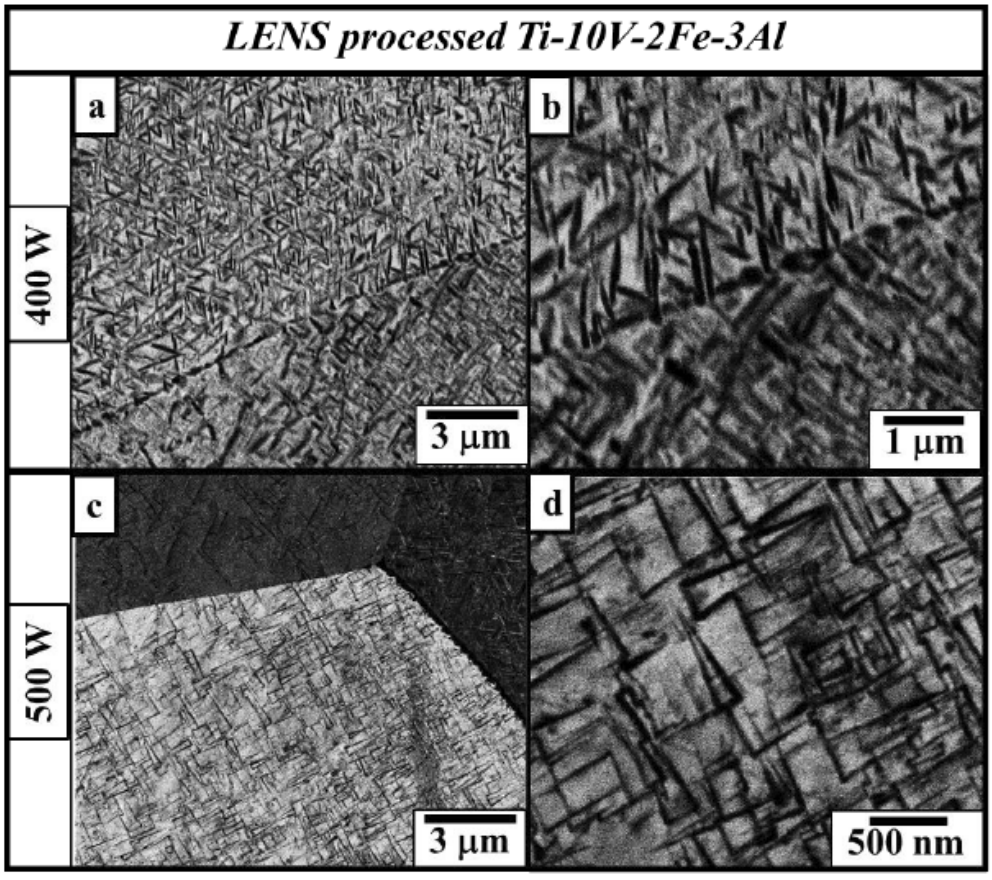

Figure 6.4: The Low and High magnification SEM backscatter images for (a,b) 400 W and (c,d) 500 W conditions of LENS processed Ti-10-2-3

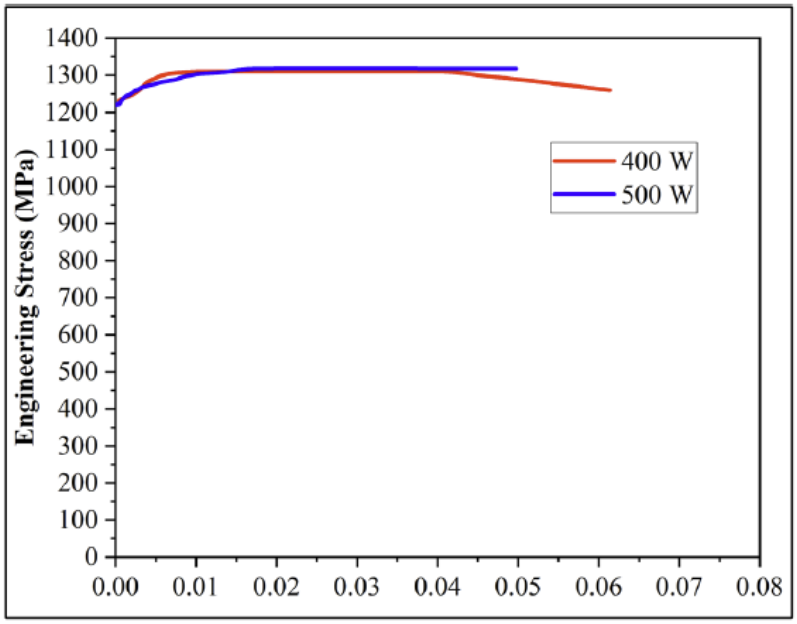

Figure 6.5: Engineering stress versus plastic strain curves for LENS processed Ti-10-2-3

The engineering stress versus plastic strain curves for the 400 W and 500 W conditions of the LENS processed Ti-10-2-3 are shown in Figure 6.5. Both the conditions exhibit similar values for the YS (~1220 MPa) despite the significant differences in the size scale of the α precipitates (Fig. 6.4). Figure 6.4 (b) and (d) are analyzed using ImageJ^{TM} software (shown in Appendix B) for the area fraction of the α precipitates. The α phase/area fraction was estimated to be ~59% in the 400 W condition and ~38% in the 500 W condition. It is generally believed that an increase in the phase fraction of secondary phases would increase the YS of any alloy (Precipitation Strengthening) [201,202]. The size scale of the precipitates follows the exact opposite trend [203]. Therefore, the possible enhancement in the YS in the 400 W condition due to the increase in phase fraction of α precipitates (to ~59% compared to ~38% in 500 W) is compensated by the increase in the size scale of the same precipitates. Besides, the slightly lower ductility observed in the 500 W condition (~5.3%) compared to the 400 W condition (~6.5%) could be due to the finer and sharper secondary (α) phase present in the former condition that acts as stress-concentration sites

during uniaxial tensile testing. Besides, the LENS processed Ti-10-2-3 owing to the finer α precipitates, exhibited significantly higher YS (~1220 MPa, Fig. 6.5) than the conventionally processed Ti-10-2-3, i.e., As-received (AR) condition (960 MPa, Fig. 6.2). It is worth mentioning that the LENS processed Ti-10-2-3 exhibited dual-phase α+β microstructures resulting in lower strain hardening values, σ_{UTS} - σ_{YS} of ~90 MPa, which is nearly identical to the As-received (AR) condition (~75 MPa). The lower observed strain hardening values and the EBSD analysis on the post deformation microstructures for the AR condition (Fig. 6.3) possibly indicate that neither of the LENS processed conditions deformed via TRIP/TWIP during the uniaxial tensile deformation.

6.3.3 Microstructure and Mechanical Properties of SLM Processed Ti-10-2-3 Alloy

The initial microstructures of the as-SLM fabricated (AF) samples are shown in Fig 6.6(a) and (b), corresponding to EBSD inverse pole figure (IPF) + image quality (IQ) and kernel average misorientation (KAM) plots from in-plane sections of the samples. Sectioning has been carried out perpendicular to the build axis for these in-plane sections. The in-plane view was chosen since the mechanical testing was carried out with the tensile axis lying in-plane. Arrows indicating the tensile testing direction have also been shown in the EBSD IPF maps. The starting condition of the AF sample shows single-phase β grains, which are square in shape with ~75 μm sides, in this two-dimensional view. The morphology of the grains can be attributed to the island scan strategy used during the deposition, as reported in previous studies [204,205]. While the island scan strategy has been recommended for its ability to lower the residual stresses in the system during the PBF process, the KAM maps indicate a significant amount of retained residual stresses [47,58]. Tensile mechanical testing was carried out on this condition, and the results are shown in Fig 6.6(c). The AF sample showed a very high value of yield strength (YS), ~850MPa, but virtually no ductility. It should be noted that three tensile samples were tested, and Fig 6.6(c) shows a

representative engineering stress-strain plot. Following the tensile testing, the surface of the tensile samples clearly exhibited slip lines corresponding to very limited plastic deformation, as revealed by SEM images (Fig 6.6(d)). There was no indication of stress-induced martensite (SIM, α") [178,198] formation in the deformed AF Ti-10-2-3 samples, based on these SEM images. This observation appeared to be unusual since Ti-10-2-3 with a single β phase is expected to exhibit stress-induced martensitic transformation and TRIP effects, based on multiple previous reports on conventionally processed alloys [179,199,200]. Therefore, to understand the deformation behavior and the lack of formation of SIM in AF Ti-10-2-3, further analysis of this sample were carried out via both TEM and Atom Probe Tomography (APT).

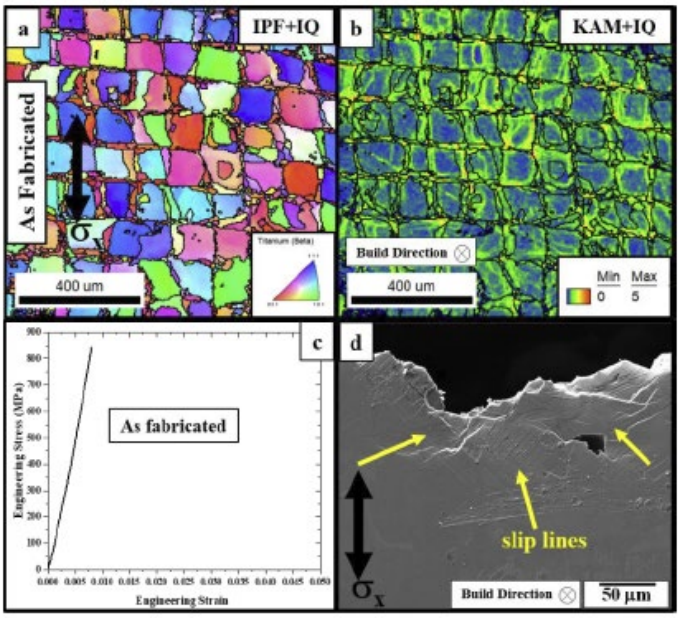

Figure 6.6: Starting microstructures of the As-fabricated sample shown via EBSD IPF (a) and KAM maps (b), (c) Engineering stress vs engineering plastic strain plot of the AF sample, (d) deformed surface of the AF sample showing slip lines.

Fig 6.7 (a) shows the dark field TEM (dark-field) image of the sample obtained from the grip section of one of the tensile specimens prepared from the AF alloy. The [011]β SADP(inset) clearly exhibits additional reflections arising from the ω phase at 1/3 and 2/3 {112}β positions. These ω reflections are an outcome of the orientation relationship between the ω (space group:

P6/mmm) and β (space group: Im-3m) phases: [11-20]ω || [011]β and [0001]ω || [111]β (Banerjee and Williams 2013). Fig 6.7(b) shows the raw Al and V ion maps from an APT reconstruction from the AF sample, clearly showing nanometer-scale pockets depleted in both these elements. These V and Al depleted pockets are indicative of isothermal ω precipitates since while the α phase rejects V and is enriched in Al, the ω phase rejects out both Al and V. The 8 at. %V- isosurface was constructed in the APT reconstruction to more clearly delineate the ω precipitates. A proximity histogram (or proxigram) analysis was carried out to quantify elemental partitioning across ω/β interfaces. The proxigram, shown in Fig 6.7(d), revealed that these ω precipitates are depleted in V, Fe, and Al. The V content within ω precipitates is ~4 at. %, while the surrounding β matrix is enriched, ~12 at. % or 13.5 wt. %.

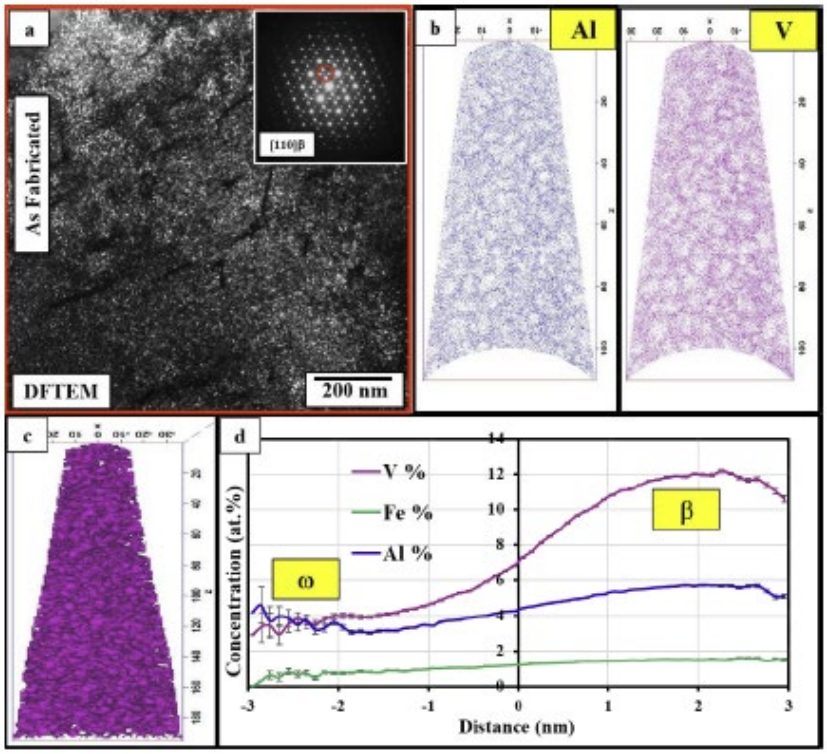

Figure 6.7: As-fabricated sample (a) DFTEM showing ω precipitates, inset shows the [011]β SADP from which DFTEM was obtained, (b) raw ion maps of Al and V showing pockets of ω precipitates, (c) V-isosurface and the proximity histogram (d) showing the compositional changes between ω/β phases.

Fig 6.8 also shows another region within the same TEM sample and another APT reconstruction from the AF Ti-10-2-3 sample. The dark-field TEM in Fig 6.8 (a) shows the presence of very fine scale α precipitates within this sample. This is also confirmed by the presence of reflections at ½ {211}β position in the [113]β SADP (inset). While ω reflections are also present in the SADP, the dark-field TEM was recorded using only the α reflection. In contrast, a higher magnification dark-field TEM images encompassing all the reflections (ω at 1/3 and 2/3 {211}β and α at ½{211]β) is shown in Fig 6.8(b). The inset shows the same [113]β SADP as shown in Fig 6.8(a). The ω particles are about 2-5 nm in diameter and exhibit a near-spherical morphology, while the α precipitates exhibit a lath or plate-like morphology with the long axis being ~40-50nm. APT ion maps in Fig 6.8(c) show both the ω and α precipitates. While the Al and V depleted pockets correspond to ω precipitates, the α lath is enriched in Al while being depleted in V, as marked in the Fig 6.8 (c). A 4.45 at. %V- isosurface further allowed quantifying the elemental partitioning across the α/β interface based on a proximity histogram (or proxigram) analysis. The calculated proxigram, shown in Fig 6.8(d), indicated that the α precipitate is depleted of Fe and V while being enriched in Al. The α precipitates are depleted in V (~ 1 at. % V), while the surrounding β-matrix is V-rich with ~ 10 at. %. These results establish that the ω precipitates in the AF condition of the Ti-10-2-3 alloy are no longer quenched-in or athermal ω precipitates, i.e., inheriting the composition of the parent β matrix (congruent with the β matrix). Rather, these are isothermal ω precipitates exhibiting a rejection of V, Fe, and Al. This change in the composition of ω precipitates leads to a corresponding change in the composition of the β matrix, especially leading to an increase in the V content, consequently increasing the β-phase stability of the matrix. These effects are bound to influence the deformation mechanisms and mechanical properties in this sample and will be discussed in more detail in subsequent sections [174,175,206].

Additionally, it should be noted that rejection of solute elements (V, Fe, Al) from the isothermal ω precipitates, most likely occurs during the multiple reheating cycles during the AM processing [207]. Therefore, the AF sample was compared with a β-solution annealed condition of the same sample, i.e., the as-fabricated sample annealed at 900 °C for 30mins followed by water quenching. This condition will be henceforth referred to as β-soln. This heat-treatment is also expected to alleviate the residual stresses in the system, arising from AM processing, and could potentially recrystallize the β grains in the microstructure [208]. The overall bulk composition obtained from the APT analysis is shown in Table 6.1.

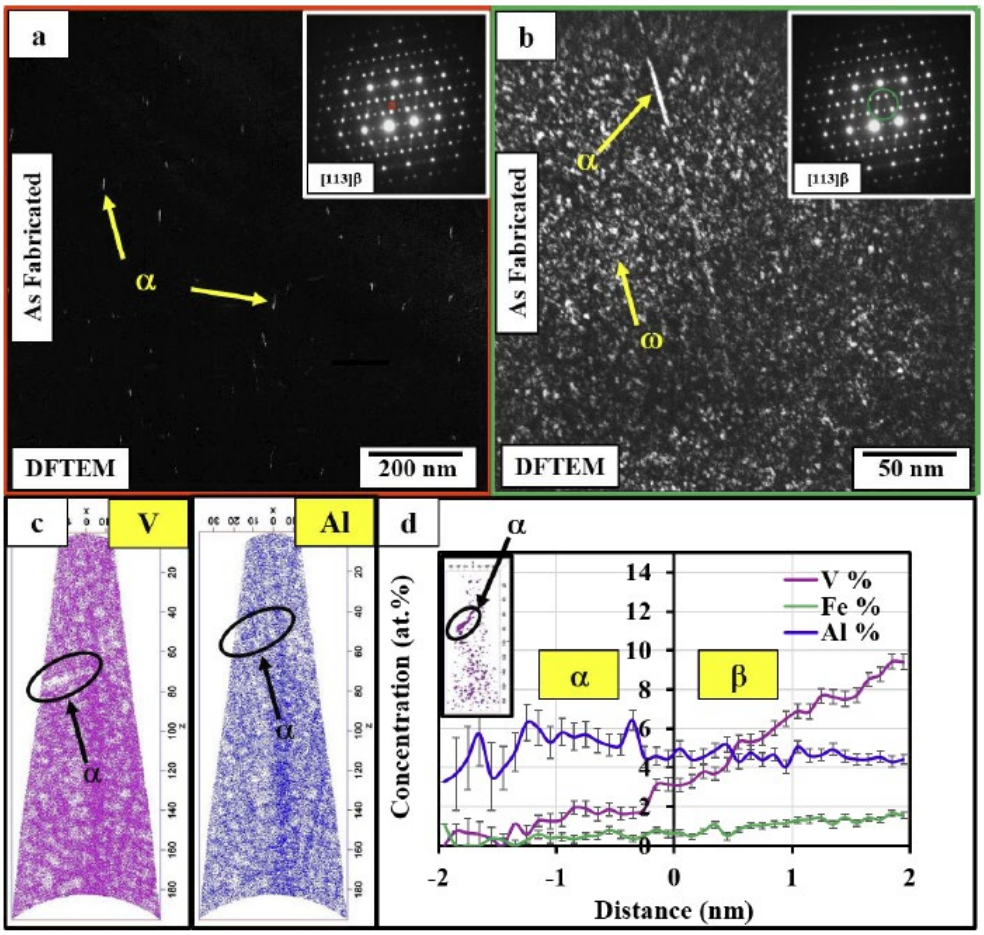

Figure 6.8: As-fabricated sample (a) DFTEM showing fine scale α precipitates, inset shows the [113]β SADP from which DFTEM was obtained, (b) DFTEM showing both ω precipitates and fine scale α precipitates, inset shows the [113]β SADP from which DFTEM was obtained, (c) raw ion maps of V and Al showing ω and α precipitates (d) V-isosurface and proximity histogram showing the compositional changes between α/β phases.

Table 6.1: Composition of the As-SLM fabricated (AF) Ti-10-2-3 alloy from Atom Probe Tomography

Element	Ti	V	Fe	Al	O
At. %	83.2	8.87	1.33	4.75	.63
Wt. %	85.7	9.72	1.6	2.76	.22

6.3.4 Reactivation of Transformation and Twinning Induced Plasticity in Additively Manufactured Ti-10-2-3 Alloy

6.3.4.1 Microstructure and Mechanical Properties of SLM Processed + β Solutionized Ti-10-2-3 Alloy

Similar to the AF condition, following the β-solutionizing, the in-plane microstructure of the sample was investigated. β-solutionizing of the as-fabricated alloy resulted in a significant change in the grain structure as observed in the EBSD IPF map shown in Fig 6.9(a). Along with an overall increase in the grain size, to ~350 microns, there is also a notable change in their morphology. The solutionizing treatment also worked in terms of relieving the residual stresses present in the as-fabricated condition, as can be seen in the KAM map in Fig 6.9(b). The [011]β SADP, shown in the inset, and the corresponding dark-field TEM image clearly reveal the presence of ω precipitates even after the β-solutionizing heat-treatment (Fig 6.9(c)). These observations are consistent with results reported in the literature on conventionally processed Ti-10-2-3 alloy [179,209]. Following the β-solutionizing, tensile testing was carried out on these samples. Similar to the case of the AF condition, three samples of the β-solutionized condition were tensile tested and the engineering stress-strain plot showing the values closest to the average are shown in Fig 6.10(a).

In contrast to the AF sample, the β-soln sample exhibits an excellent combination of strength, strain-hardenability, and ductility, especially for an AM processed β-Ti alloy. With YS ~500MPa and UTS ~1 GPa, the difference between UTS and YS is quite significant (~500 MPa),

with a 6% tensile strain-to-failure. Fig 6.10(b) puts in context the high strain-hardening (difference between UTS and YS) achieved in this alloy, compared to the other Ti alloys processed via AM.

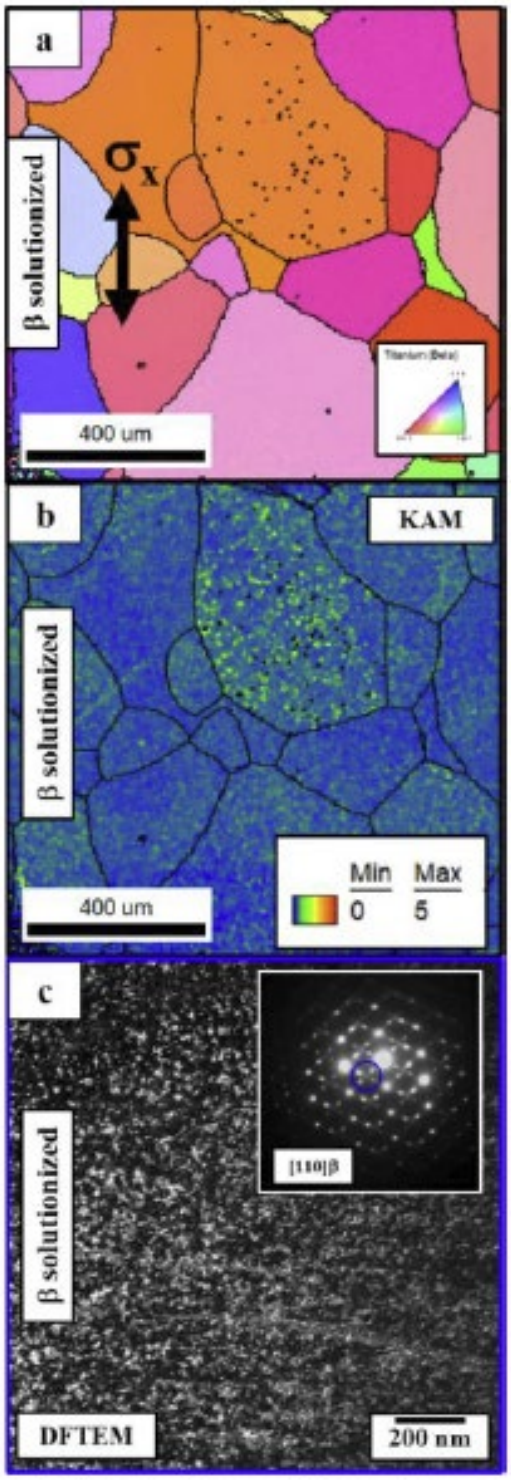

Figure 6.9: Starting microstructure of the β-solutionized sample, (a) EBSD IPF map, (b) KAM map, (c) DFTEM image showing ω-athermal and the SADP from where the DFTEM were captured.

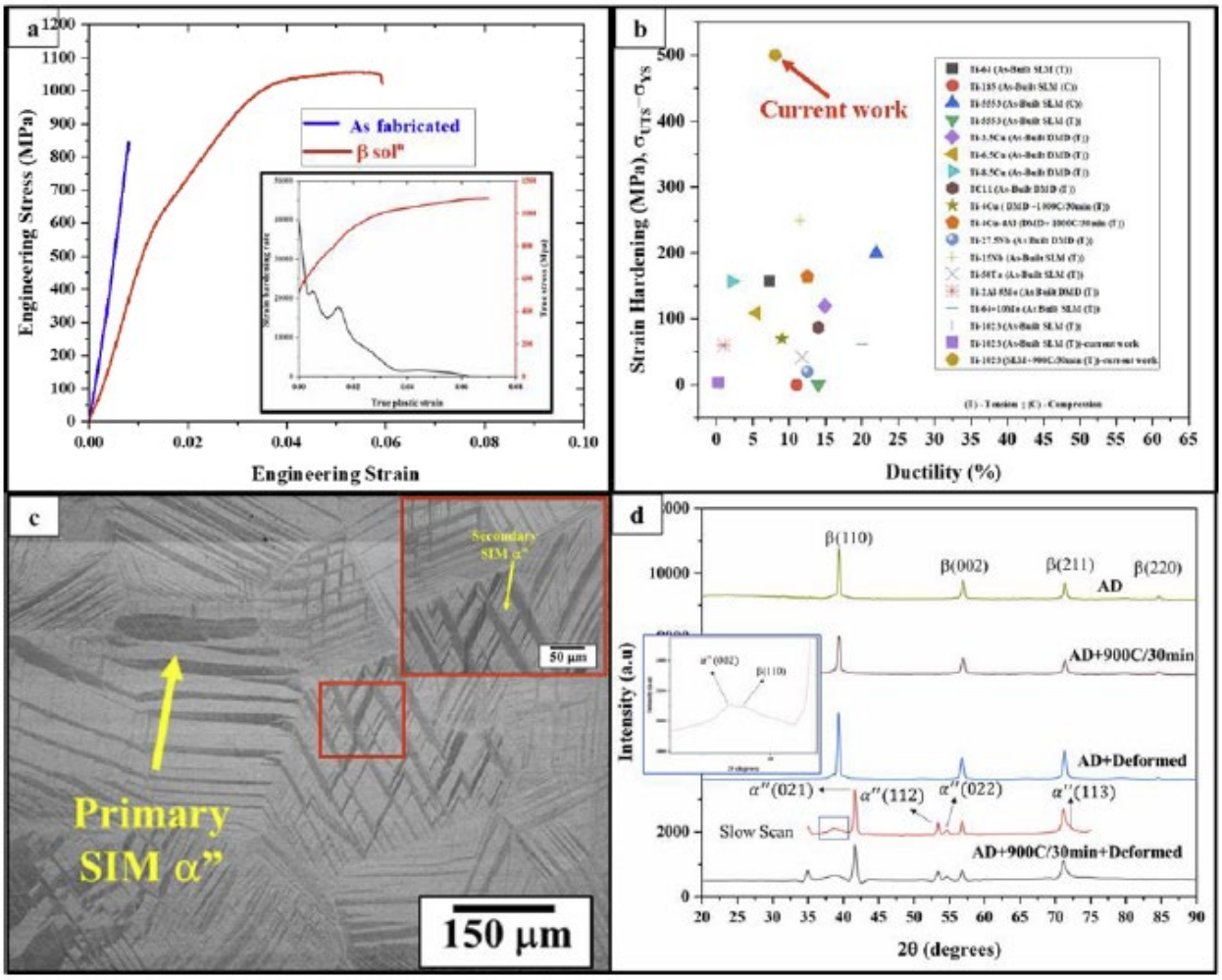

Figure 6.10: Engineering stress-strain curves of the β-soln conditions. Inset shows the true stress v true strain curve along with the corresponding strain-hardening rates of the β-soln sample, (b) Ashby plot comparing the strain hardening of the current alloy with other AM processed Ti-alloys, (c) SEM micrographs of the deformed surface showing SIM (α") across multiple length scales (d) XRD of the two conditions before and after deformation. Additional peaks of α" were noted in the β-soln condition post deformation.

As evident from this plot, the strain-hardening is more than double the nearest alloy. Ti-6Al-4V which is the most commonly used alloy for AM, shows a maximum strain-hardening of ~175MPa, compared to ~500MPa observed in the present case. The inset in Fig 6.10(a) shows the true stress – true strain tensile curve, and the corresponding work-hardening rate has a value of ~15000 MPa. While previous reports have talked about a high rate of work hardening in other β-Ti alloys [210], the values reported here are higher in comparison. Interestingly, the work-hardening plot also

exhibits clear humps as a function of true strain. These humps have been previously attributed to the TRIP/TWIP effect in β-Ti alloys [177,211] and warrant further investigation. Preliminary SEM imaging, Fig 6.10(c), of the deformed surface clearly shows the presence of stress-induced martensite (SIM (α")). It is interesting to note that the formation of α" occurs across multiple length scales. Within the primary network of α" plates, secondary α" plates are also seen, and these have been highlighted in Fig 6.10 (c) [212–214]. Fig 6.10(d) shows the XRD of both conditions, before and after deformation. Before deformation, both AF and β-soln conditions exhibited peaks from only single β phase. Post deformation, while there were no additional peaks observed for the AF sample, additional reflections, indicating the presence of the α" phase are evident in the β-soln condition. The presence of additional peaks of α" (112), α" (022) and α" (114) are marked in this XRD pattern. In order to understand the high value of strain-hardening observed in this condition, SEM-EBSD and TEM studies have been further carried out to investigate the deformation behavior of the β-soln sample.

Fig 6.11 shows the EBSD analysis, post deformation, of the β-soln sample. Fig 6.11(a) shows the schematic of the tensile sample and the locations selected for EBSD analysis. The IPF and phase maps from these locations are shown in the series, Figs 6.11(b)-(e). A significant change in the overall phase fraction of α" is observed in these different regions. This is possibly due to the orientation of the grains and the consequently the Schmid factor. Similar observations have been previously reported by Lilensten et al [215]. Multiple intersections of α" laths can be observed in the IPF images (marked with arrows) and at these intersections, significant shear displacements are visible, which are indicative of strain localization as discussed in previous reports [47]. Based on these analyses, two regions were further investigated in further detail, coupling EBSD at higher magnification and TEM analysis; (i) region which had 36% α" and (ii) region which has 93% α".

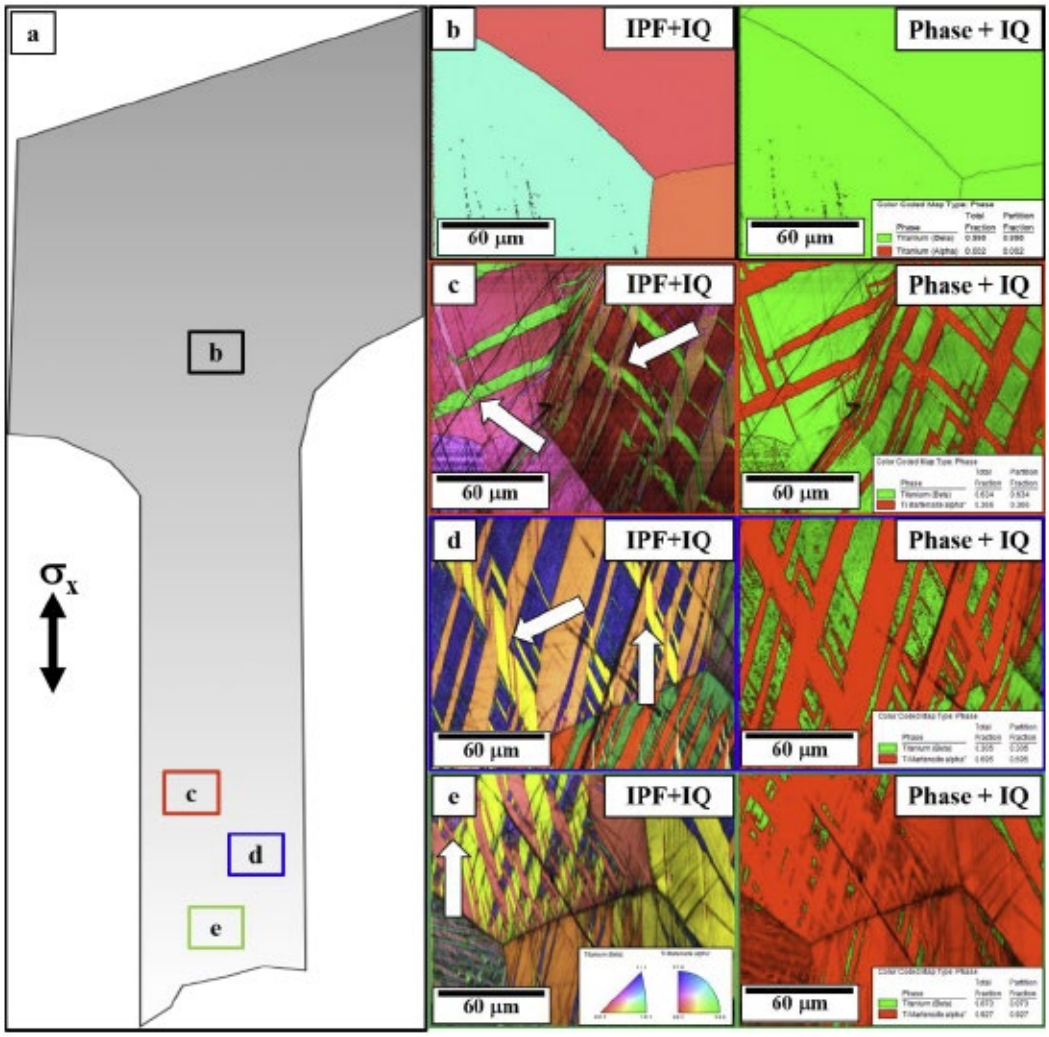

Figure 6.11: (a) schematic of the tensile sample post fracture, and corresponding EBSD maps ((b), (c), (d), (e)) from the different locations indicated on the schematic.

The EBSD IPF+IQ map and discrete pole figures in Figure 6.12 leads to more insights into the deformation behavior. Area of interest 1, shown in Figure 6.12(a), shows the intersection of two stress induced martensite laths. The discrete plots confirm the existence of the standard OR between β and α", i.e. {110}β // (001)α" [213]. It is also interesting to note that two distinct α" laths also have the standard twin relation of {111}α" as can be seen in the discrete plot labeled 3. Area of interest 2 shows the presence of twins inside the martensite lath. These are most probably transformation twins formed during the formation of stress-induced martensite laths [211,216] also share a {111}α" plane. These are generally labeled as type I twins [217].

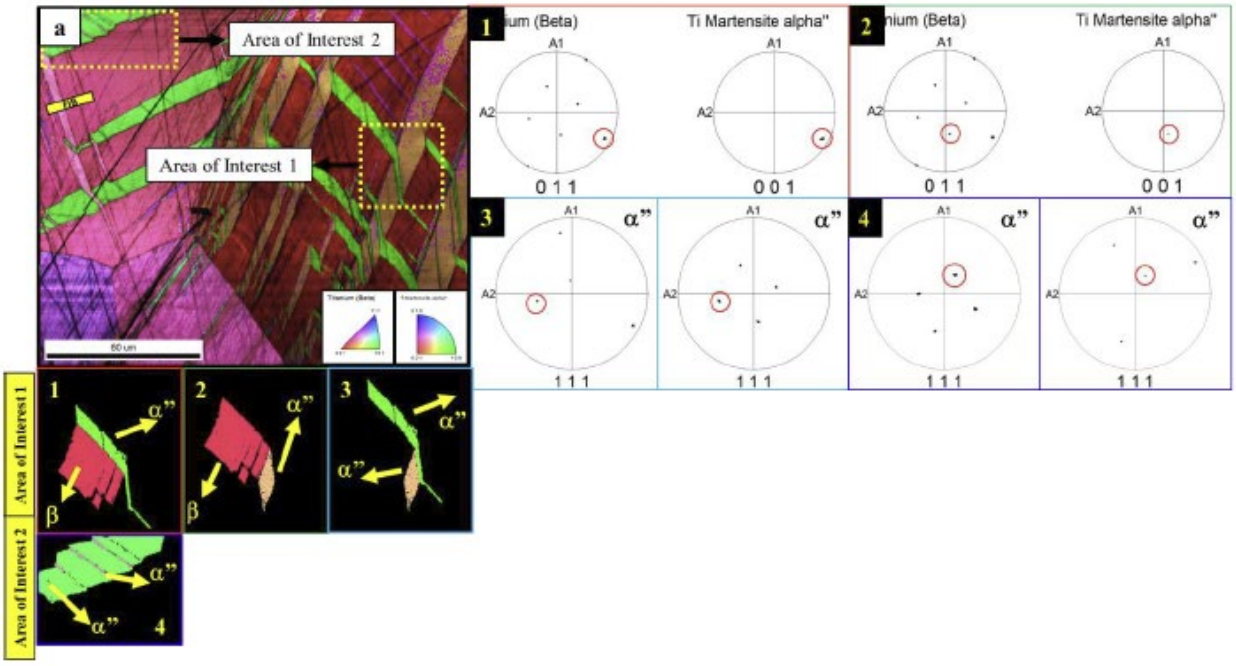

Figure 6.12: EBSD IPF+IQ maps of sample which had 37% α" showing two areas of interest and their corresponding discrete plots identifying orientation relationships.

The regions of the retained parent β matrix in this area of the tensile sample, corresponding to 36% of α" and 64% of β (shown in Fig. 6.11(c)), have been further investigated via site-specific TEM examination. An approximate area from where the FIB lift-out was extracted has been indicated with a box in Figure 6.12 and the bright-field TEM image of this TEM sample is shown in Fig 6.13(a). Two regions highlighted in this area have been further investigated and corresponding magnified images are shown in Figs 6.13(b) (Region 1) and 6.13(e) (Region 2) respectively. Region 1 shows the presence of a band, on which further conventional diffraction and precession electron diffraction (PED) analysis was carried out. The PED data shown in Fig 6.13(d) shows the IQ + IPF, and IQ + phase map. The phase map clearly indicates the presence of the α" phase within the β matrix. Even at this scale, multiple intersections of these α" laths can be noted. The diffraction patterns from the three different locations marked in Fig 6.13(d) are shown below. These were obtained using the Acom software after the data collection via the Topspin 3.0

software. As can be seen, the three diffraction patterns show the orientation relationship between the β matrix and α" laths, i.e. [113]β || [112]α". This was also confirmed by the conventional TEM selected area diffraction pattern, shown in Fig 6.12(c), recorded along the [113]β ZA. The additional spots in this diffraction pattern also confirm the presence of α". The retained β regions, highlighted by the orange box (Region 2), also exhibit interesting features, especially with respect to the ω precipitates. The shearing of these precipitates influences the deformation behavior and mechanical properties of this β-soln sample, as compared to the as-fabricated sample.

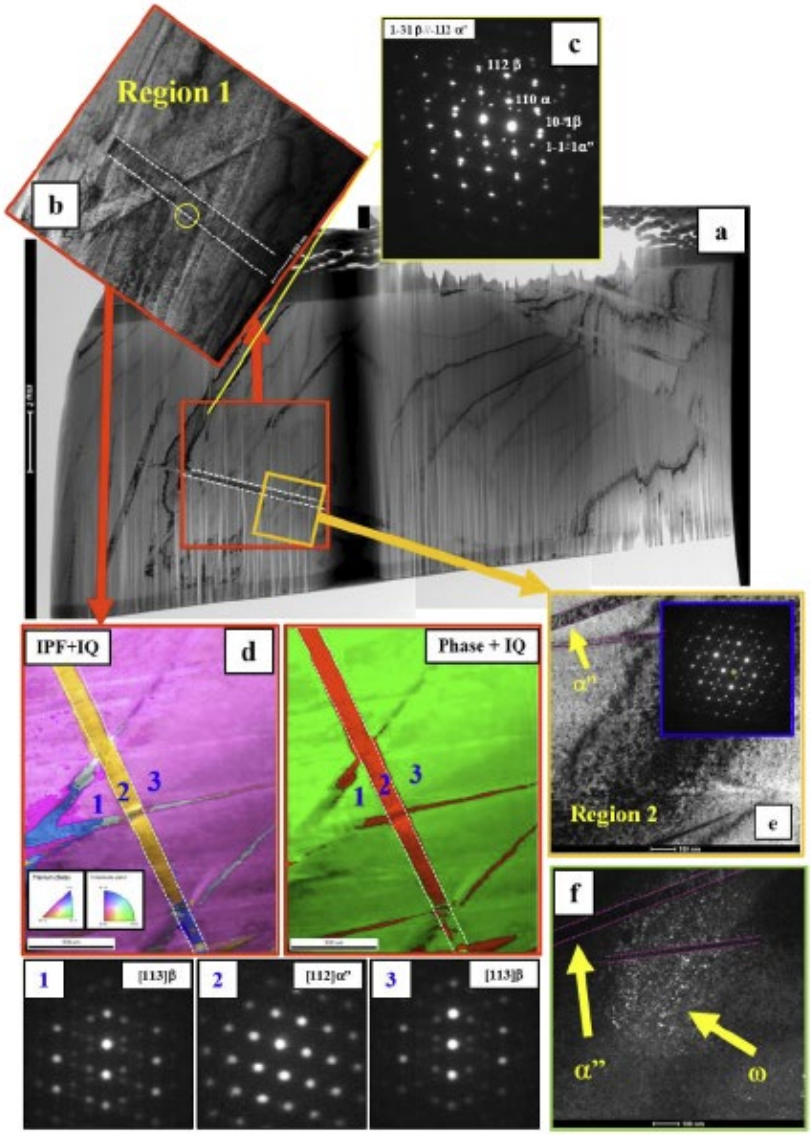

Figure 6.13: TEM analysis of the site-specific sample from region which had 37% α" in Fig 6.11.

The discrete pole figures corresponding to the different α" variants and the adjacent β matrix phase have been plotted in the figure. Similar to sample which had 36% α", the two areas of interest showed different variants of α" laths as well as internal twinning within these martensite laths. With respect to area of interest 1, the expected{001}α"//{011}β orientation relationship between the α" variants and the adjacent β matrix is noted, while also showing twin relation along {111}α" plane. With respect to area of interest 2, Figure 6.14(e) shows the pole figures for a thick α" lath and the internal twin present within this lath. These pole figures clearly establish that the that internal twinning is of the {111} type [209,217].

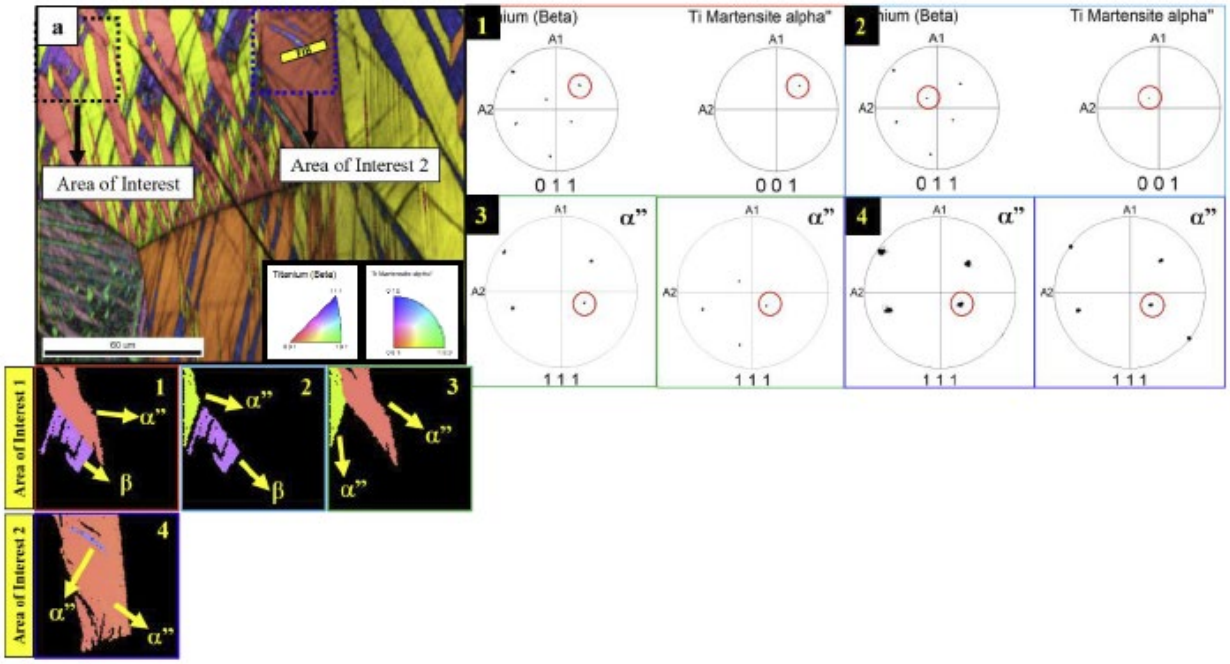

Figure 6.14: EBSD IPF+IQ maps of sample which had 93% α" showing two areas of interest and their corresponding discrete plots identifying orientation relationships.

TEM analysis was also carried out on a sample extracted from within the area of interest 2 as shown in Figure 6.14(a). As noted earlier, this region is closest to the fracture site, i.e., 93% α". This TEM sample (Fig 6.15(a)) predominantly comprised a single thick primary α" lath, which shows internal hierarchical features. Two specific regions have been highlighted in Figure 6.15(a).

Fig 6.15(b) corresponding to highlighted region in red, exhibits an internal twin within the primary α" lath. Furthermore, within this primary twin, there are finer scale secondary twins as shown in Figure 6.15(b). The corresponding selected area diffraction pattern from the lath, encompassing the twins, is shown in Fig 6.15(c) and confirms the primary twin orientation with additional spots corresponding to the internal secondary twinning. Interestingly, in the magnified view of the highlighted region in green, shown in Fig 6.15(e), a small patch of the parent β-matrix along with stress induced martensite laths was noted. The DFTEM images shown in Fig 6.15(e) and (f) are taken from the spots highlighted in Fig 6.15(d). The high strain-hardening observed in the AM fabricated plus β-soln Ti-10-2-3 alloy can be attributed to this hierarchical microstructure containing stress-induced martensite laths of different size scales coupled with hierarchical internal twinning within these α" laths [194,208].

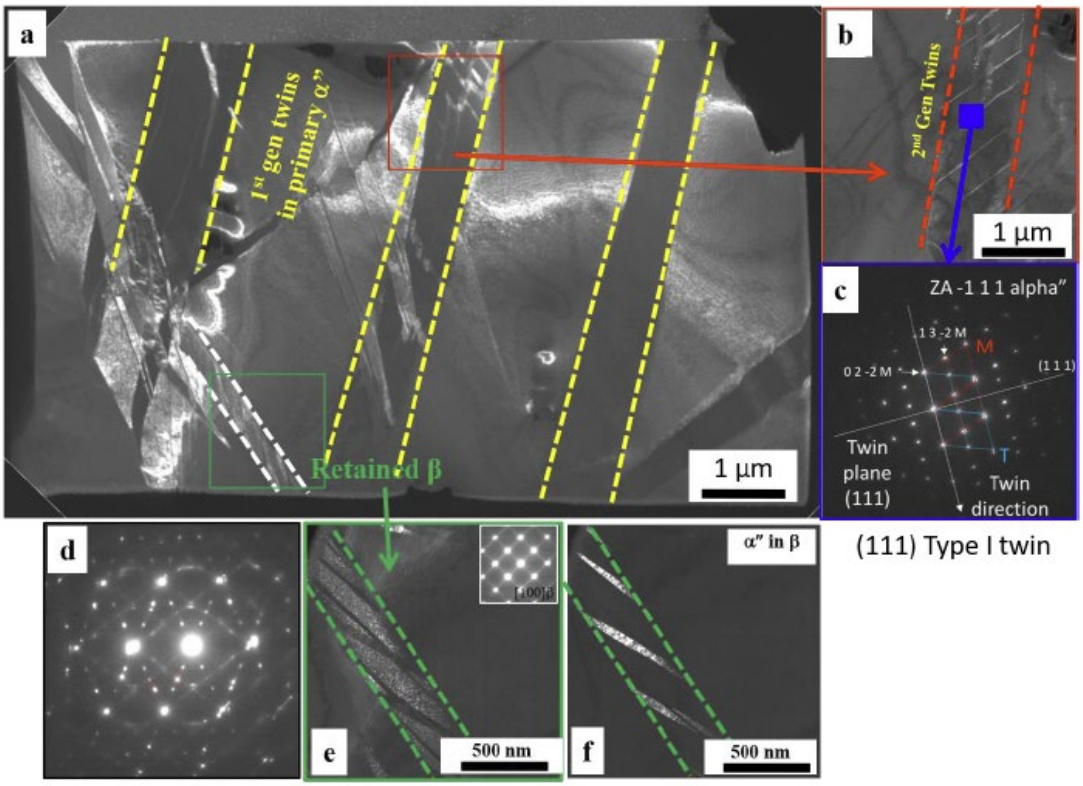

Figure 6.15: TEM analysis of the site-specific sample from region which had 93% α" in Fig 6.6. Hierarchical features including first and second generations twins formed within the stress induced martensite lath can be seen.

APT studies were also performed on the β-solutionized sample. The raw ion maps shown in Fig 6.16 (a-c) do not exhibit any discernible pockets devoid or enriched in any of the solute atoms. Additionally, frequency distribution analysis was performed on the raw data of the V ions and compared to a theoretical binomial distribution (representing a random distribution). The concentration of V was calculated in every 100 ion bins, and the V-rich section of the histogram frequency vs. V concentration is plotted in Figure 6.16(d). Additionally, the binomial distribution has also been shown in the same plot and both the distributions are almost identical. Therefore, APT could not detect composition partitioning in the β-solutionized condition. However, as shown in Figure 6.8(c), this microstructure consists of a very high number density of fine scale ω precipitates within the β matrix, and the APT results establish that these quenched-in precipitates are athermal ω precipitates which inherit the composition of the parent β matrix.

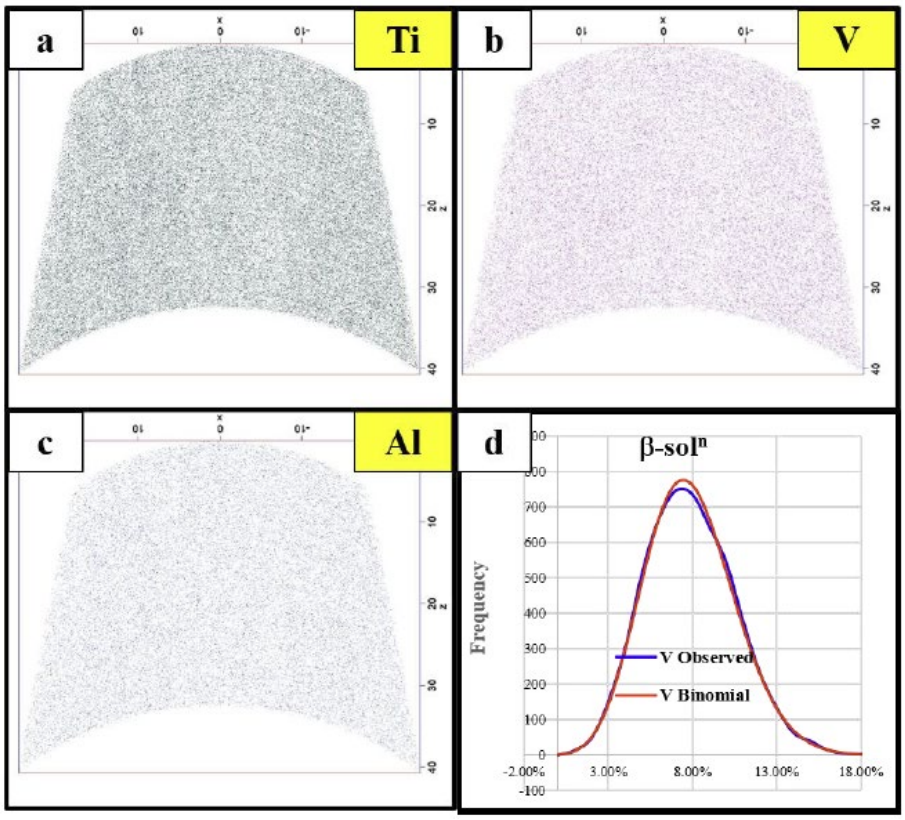

Figure 6.16: APT of β-soln sample, raw ion maps of (a) Ti, (b) V, and (c) Al does not show any partitioning, which is further corroborated by LBM plot (d)

6.3.4.2 Comparison of the Microstructure and Mechanical Properties of SLM Processed and SLM Processed + β–Solutionized Ti-10-2-3

The experimental observations indicate a substantial difference between the deformation behaviors of the AF and β-soln conditions of the SLM processed Ti-10-2-3 alloy, with exceptional strain hardening resulting from stress-induced martensite formation or TRIP effect in case of the latter condition. Possible reasons underlying this difference, based on previous reports in the literature, include differences in the grain size and morphology [218–221], and the chemical composition of the parent β matrix [60,125,174]. Previous reports on the Ti-10-2-3 and other metastable β-alloys, emphasize the effect of grain size on the triggering stress required for stress-induced martensite formation. This triggering stress has been reported to initially decrease with an increase in grain size, reaching a minimum value, and subsequently again increase with a further increase in grain size [219]. Comparing the AF and β-soln conditions in the present case, while the grain size increases from ~100 microns to ~350 microns, these grain sizes are too large to exhibit any significant difference in the triggering stress for the TRIP effect. The chemical composition of the β-phase is another important factor in determining the degree of metastability of the β phase and consequently the deformation behavior of β-Ti alloys [174,206]. With an increase in the β phase stability, the deformation behavior changes from TRIP to TWIP, and finally to dislocation slip. A previously reported investigation has shown that in case in a binary Ti-12Mo alloy, a change in the chemical composition of the parent β-matrix phase, due to Mo partitioning between the matrix and isothermal ω precipitates, leads to a change in the deformation behavior from TRIP/TWIP to slip [174,180,222]. Similar observations were also made by Lai et al. in their work on Ti–25Nb–0.7Ta–2Zr (at. %) alloy [206]. The SLM processed AF Ti-10-2-3 alloy, in the present study, undergoes multiple heating-cooling cycles during AM processing, which could potentially lead to a change in the chemical composition of the β matrix due to partitioning of alloying

elements between β and ω, thus causing the sample to deform via slip, and not via TRIP/TWIP.

The APT results indicate that while the β phase in case of the AF sample contains ~12at% V, after β-solutionizing the alloy contains ~9.3at% V. While this is a measurable difference in the chemical composition of the β-matrix, it is not sufficiently large to be solely responsible for changing the deformation behavior, unlike the previous report on the Ti-12Mo alloy [174]. Therefore, the role of the ω precipitates on the deformation behavior and mechanical properties needs to be considered. Based on the APT results (AF and β-soln), while the isothermal ω precipitates contain ~4at% V in case of the AF condition, the athermal ω precipitates contain ~9.3at% V in case of the β-soln condition.

There has been a substantial amount of discussion in the literature on the role of ω phase precipitates on the plasticity, deformation behavior, and tensile properties of titanium alloys. It has been well-established in many previous reports that athermal or quenched-in ω precipitates, which inherit the composition of the parent β matrix, are typically not detrimental to plastic behavior. Therefore, titanium alloys with such athermal ω precipitates are often quite ductile and exhibit good strain-hardenability [180,182,222]. Contrastingly, it has been reported that in cases where there is a compositional partitioning between the β and ω phases, referred to as isothermal ω precipitates, there is often an increase in yield strength, accompanied by a severe loss of ductility [174,206,223,224]. Despite these previously reported experimental observations, the underlying mechanism leading to such increase in yield strength, but accompanied with loss of ductility, is not well understood. Lai et al in a recent study on Ti-Nb-Zr-Ta alloys, indicates the role of Nb content on the shear modulus of ω precipitates, and subsequently the deformation behavior of the alloy [206]. We noticed a similar effect in the current system, wherein the densely distributed ω particles in the AF condition act as barriers for the transformation induced plasticity effect by

suppressing the martensite formation. A combination of that and the formation of the ω precipitates and some fine scale α precipitates due to the multiple reheating cycles, leads to an enrichment of the β-stabilizers in the parent β-matrix, subsequently causing the sample to deform via slip.

6.3.5 Influence of Laser Additive Processing on the Microstructure and Mechanical Properties of Ti-10-2-3 Alloy

The results presented in sections 6.3.2 and 6.3.3 indicate that the microstructure and mechanical properties of the LENS (DED) and SLM (PBF) processed Ti-10-2-3 are noticeably different. The LENS processed Ti-10-2-3 exhibited dual-phase (β+α) microstructure with fine-scale α precipitates homogeneously distributed within the β–matrix (Fig. 6.4). In contrast, the SLM processed Ti-10-2-3 showed dual-phase (β+ω) microstructures with ultrafine-scale hard isothermal-ω precipitates uniformly formed within the β-matrix (Fig. 6.7). Consequently, the uniaxial-tensile properties of these two differently processed alloys were also different. The LENS processed alloy shows remarkably higher YS and ductility than the SLM processed counterpart. However, both of these alloys show significantly lower strain hardening values, similar to conventionally processed, As-received (AR) Ti-10-2-3 alloy. Thus, neither additively manufactured alloys exhibited any signs of TRIP/TWIP under uniaxial tensile deformation. Although both LENS and SLM processes fall under the laser-based additive manufacturing category, they are fundamentally different. The former utilizes a dynamic powder-fed (via inert gas) system, while the latter uses a static powder-bed system to fabricate the alloys. Therefore, the radically different microstructures between LENS and SLM processed alloys could be mainly due to inherently different thermo-kinetics associated with the respective process.

Figure 6.17 summarizes the mechanical properties of various conditions investigated as a part of the current work. The YS and ductility are shown in the X and Y axes, respectively. At the

same time, the strain hardening values (difference between UTS and YS) are represented by the numbers listed (near the respective data points) in the plot.

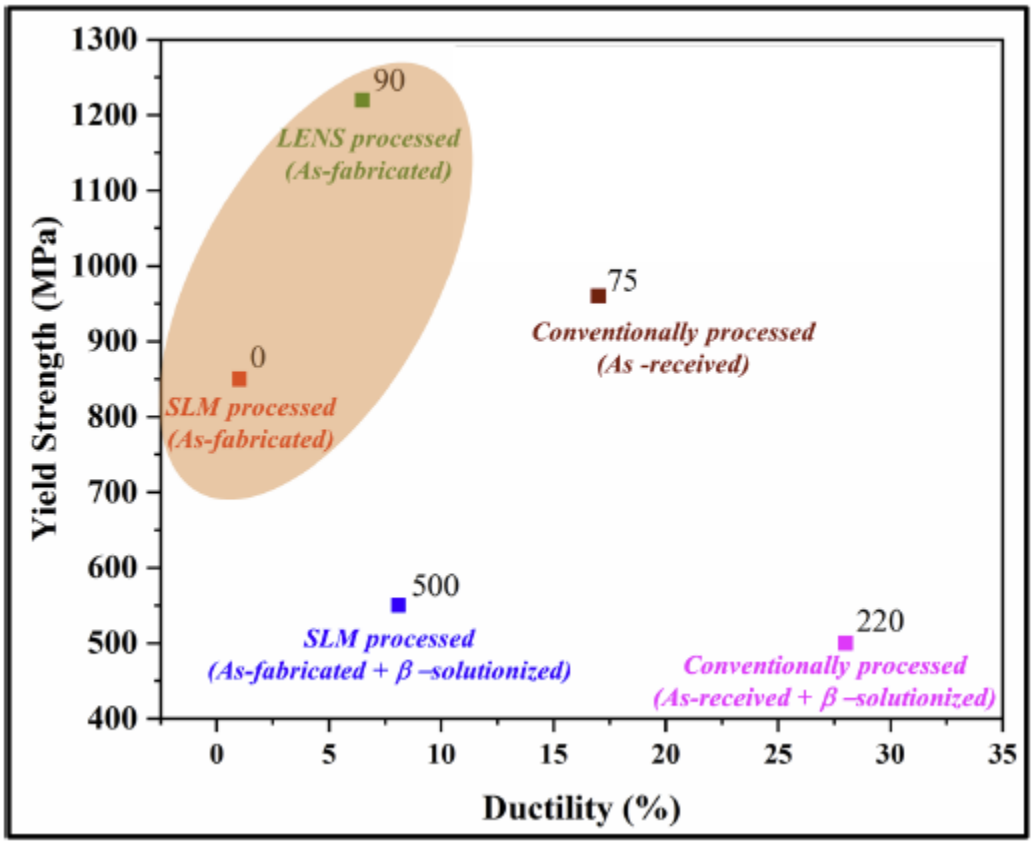

Figure 6.17: Summary of mechanical properties for Ti-10-2-3 fabricated via various manufacturing techniques

6.4 Conclusions

Summarizing, this chapter investigates the microstructure and mechanical properties of a commercial β-Ti alloy, Ti-10V-2Fe-3Al (wt. %), processed via two different additive manufacturing routes, SLM and LENS. In addition, the conventionally processed alloy is also investigated to compare and contrast with the additively manufactured Ti-10-2-3. The conventionally processed Ti-10-2-3 in the as-received state showed dual-phase (α+β) microstructures with two different kinds of α precipitates, i.e., coarser ones with equiaxed morphology and finer ones with lath-like morphology. The LENS processed alloy showed similar

microstructures but with only a single kind of lath-like α precipitates which are substantially more refined than the as-received alloy. Unlike the other two conditions, the SLM processed Ti-10-2-3 exhibits an entirely different microstructure: a dual-phase (β+ *isothermal* ω) microstructure.

Among the three conditions, the LENS processed showed the highest YS of ~ 1220 MPa, followed by conventional (~960 MPa) and SLM (~850 MPa). While the LENS and conventionally processed alloys showed reasonable tensile ductility, the SLM processed alloy showed virtually no ductility. Interestingly, after the SLM processed alloy was subjected to a β-solutionizing treatment, it exhibited substantial recovery of tensile ductility coupled with very high strain hardening (tensile strength minus yield strength ~500MPa) and a significantly high strain hardening rate ~15000. The extraordinarily high strain hardening rate in SLM processed + β-solutionized Ti-10-2-3 alloy can be attributed to relatively thick stress-induced martensitic α" laths/plates, exhibiting a hierarchical internally twinned microstructure, comprising multiple generations of deformation-induced twins. The recovery of the TRIP effect in this alloy after the β-solutionizing treatment can be attributed to the reversal from hard non-shearable isothermal ω precipitates in the as SLM processed condition, to softer shearable athermal ω precipitates in the β-solutionized state. Exploiting the TRIP effect in AM processed Ti alloys via process parameter optimization can substantially increase tensile strength and uniform ductility in this critical class of lightweight, high-strength engineering alloys.

CHAPTER 7

CONCLUSIONS AND FUTURE WORK

7.1 Conclusions

The growth of columnar grains and development <001>β texture along the build direction during fabrication is one of the significant challenges associated with the Additive Manufacturing of Ti alloys. One of the key objectives of this work is to understand this challenge associated with additive manufacturing. Nine different metastable β Ti-alloys were fabricated using Laser Engineered Net Shaping (LENS) process to understand the influence of various alloying elements on the evolution of columnar grains with <001> texture. The microstructural aspects such as grain morphology and texture in the build direction were investigated for all nine alloys. Ti-20V, Ti-12Mo, Ti-18 exhibited long columnar grains with significant <001>β texture in the build direction. TNZT and β-21S revealed mixed columnar-equiaxed grains with moderate <001>β texture. While Ti-18-0.5B, Ti-18-0.5C, Ti-18-0.5Si, and Ti-185 exhibited equiaxed grains with randomized texture along the build direction. The following analytical models based on the fundamentals of the solidification process were investigated to rationalize the experimental observations:

1. Growth restriction factor (GRF) Model: (a) Schmid and Fetzer's approach (reliable) and (b) Desnain's approach (rudimentary but extensively used)
2. Solidification Range aspect from the theory of homogenous nucleation (ΔT = liquidus temp. –solidus temp.)

The first approach investigated, i.e., the GRF model, was initially developed for conventional casting methods, and significant efforts have been focused on extending the concept of GRF to AM. The GRF model fails to interpret the grain growth behavior in the alloys considered in the present study. Alternatively, the second approach based on the solidification range of the alloys has been proposed for the first time to rationalize the observations. The larger solidification

ranges coupled with rapid cooling rates involved in the LENS process allow the alloy melt to attain higher levels of undercooling before the onset of nucleation (primary nucleation events, at fs=0), which increases the tendency to form an equiaxed microstructure with randomly textured grains.

The secondary objective of the work is to understand the microstructural evolution and microstructure-mechanical property relationships in additively manufactured commercial β-Ti alloys, Ti-1-8-5, and Ti-10-2-3. These alloys are used for high-strength applications in the aerospace industry, such as landing gears and fasteners. They contain eutectoid elements (Fe) and are prone to beta flecking, making them challenging to fabricate via conventional manufacturing techniques. The current LENS and SLM processing results show that locally higher solidification rates in AM can prevent the problem of beta flecking and potentially produce β titanium alloys with significantly enhanced mechanical properties over conventionally cast/forged counterparts. Detailed microstructural characterization was performed in each alloy to understand the microstructural evolution and their attendant impact on the deformation behavior. The influence of process parameters on the nature of second phase precipitation within the β matrix grains for Ti-1-8-5 alloy, α or ω, has also been rationalized using a multi-physics thermo-kinetic model that predicts the multiple heating-cooling cycles experienced by the layers during the LENS deposition.

Overall, the results indicate that Ti-1-8-5 and Ti-10-2-3 are promising β-Ti alloys for AM processing. Further, the results demonstrate the ability to tune the microstructure (secondary phase precipitation and grain size) via changes in the process parameters to achieve desirable mechanical properties, obviating the need for any secondary post-processing.

7.2 Future Work

The phase fraction of α phase in the LENS fabricated Ti-10-2-3 alloy was estimated to be ~59% in the 400 W condition and ~38% in the 500 W condition. Also, the size scale of the α

precipitates in the 500 W condition appeared to be substantially more refined than the 400 W condition. The future work relevant to this study is as follows:

1. Rationalizing the discrepancy in the phase fraction and size of the α precipitates between the two conditions (400 and 500 W) by simulating the multiple heating-cooling cycles experienced by the layers during the LENS deposition using the same COMSOL multi-physics thermo-kinetic model used for Ti-1-8-5.
2. Investigating the deformed microstructures of these conditions using TEM to understand the effect of size scale and phase fraction of the α precipitates on the observed mechanical properties.

Also, the results presented in chapter 4 explain the role of alloying elements on the evolution of columnar and equiaxed grains during the additive processing of beta titanium alloys. Coupling this understanding with the concept of beta phase stability prediction via parameters like bond order (Bo), the energy level of metal d-orbital (Md), Mo equivalency, etc., to design a novel beta titanium alloy with the desired microstructures for structural applications will be an interesting future study.

APPENDIX A

SUPPLEMENTARY FIGURE FOR CHAPTER 5

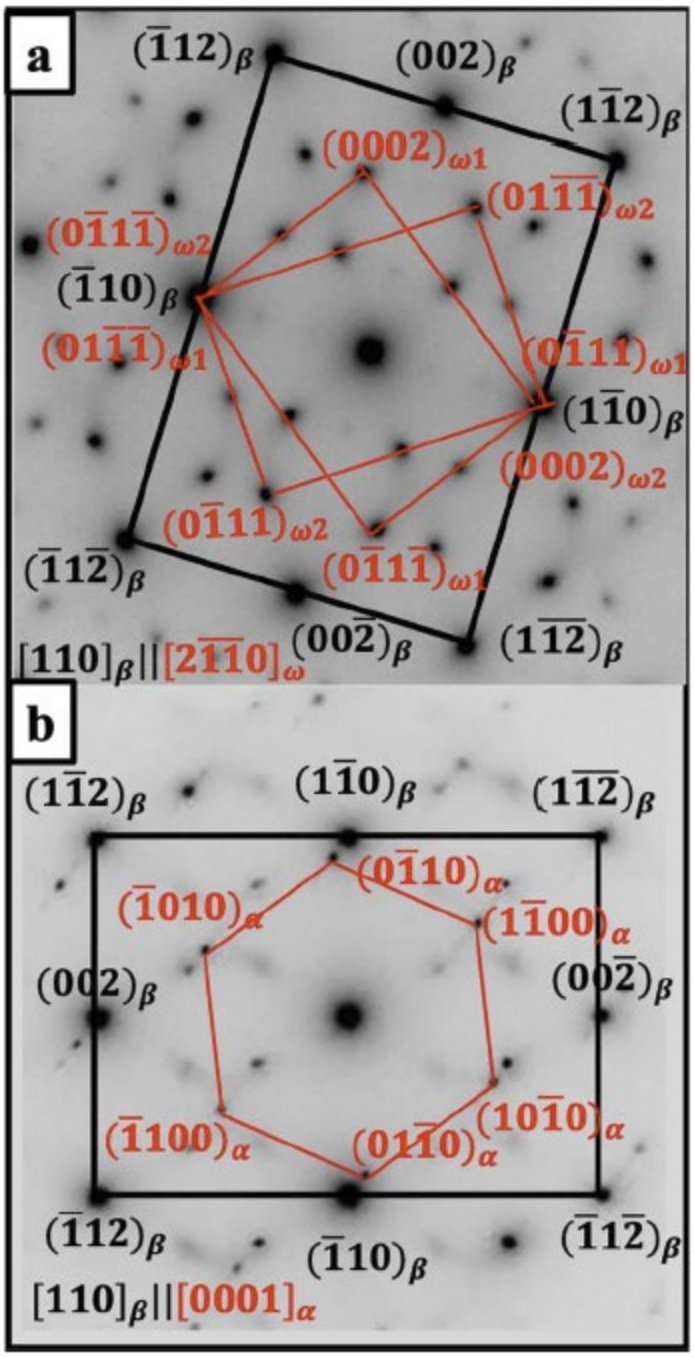

Diffraction patterns showing orientation relationship between (a) Beta matrix and Omega phase, $[110]_\beta||[2\bar{1}\bar{1}0]_\omega$ and (b) Beta matrix and alpha phase, $[101]_\beta||[0001]_\alpha$

APPENDIX B

SUPPLEMENTARY FIGURE FOR CHAPTER 6

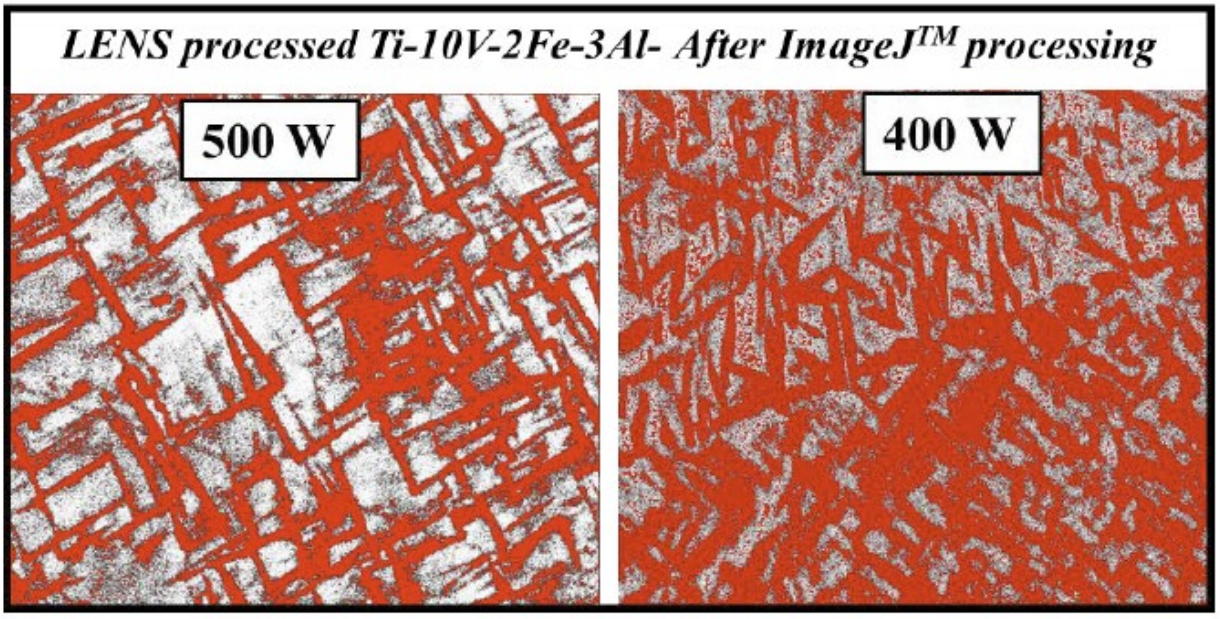

ImageJ™ processed SEM images highlighting the alpha precipitates in red, obtained from 500 W and 400 W conditions of the LENS fabricated Ti-10-2-3 alloy

REFERENCES

[1] G. Lütjering, J.C. Williams, Titanium, Springer Science & Business Media, 2007.

[2] O. Takeda, T. Ouchi, T.H. Okabe, Recent Progress in Titanium Extraction and Recycling, Metall. Mater. Trans. B. 51 (2020) 1315–1328. https://doi.org/10.1007/s11663-020-01898-6.

[3] H.D. Holland, R.L. Rudnick, K.K. Turekian, The Crust, Elsevier Science, 2005. https://books.google.com/books?id=QT52UZxDFwgC.

[4] O. Takeda, T.H. Okabe, Chapter 16 - Recycling of Ti, in: Z.Z. Fang, F.H. Froes, Y.B.T.-E.M. of T. Zhang (Eds.), Elsevier, 2020: pp. 363–387. https://doi.org/https://doi.org/10.1016/B978-0-12-817200-1.00016-8.

[5] S. Banerjee, P. Mukhopadhyay, Phase transformations: examples from titanium and zirconium alloys, Elsevier, 2010.

[6] The periodic table of the elements by WebElements, (n.d.). https://www.webelements.com/ (accessed November 2, 2021).

[7] G. Welsch, R. Boyer, E.W. Collings, Materials properties handbook: titanium alloys, ASM international, 1993.

[8] I. Weiss, S.L. Semiatin, Thermomechanical processing of beta titanium alloys—an overview, Mater. Sci. Eng. A. 243 (1998) 46–65. https://doi.org/https://doi.org/10.1016/S0921-5093(97)00783-1.

[9] C. Leyens, M. Peters, Titanium and titanium alloys: fundamentals and applications, Wiley Online Library, 2006.

[10] D. Banerjee, J.C. Williams, Perspectives on titanium science and technology, Acta Mater. 61 (2013) 844–879.

[11] P. Duwez, The martensite transformation temperature in titanium binary alloys., CALIFORNIA INST OF TECH PASADENA PHYSICAL METALLURGY LAB, 1952.

[12] M.J. Donachie, Titanium: a technical guide, ASM international, 2000.

[13] I. Weiss, S.L. Semiatin, Thermomechanical processing of alpha titanium alloys—an overview, Mater. Sci. Eng. A. 263 (1999) 243–256.

[14] D. Banerjee, J.C. Williams, Perspectives on titanium science and technology, Acta Mater. 61 (2013) 844–879. https://doi.org/10.1016/j.actamat.2012.10.043.

[15] D. De Fontaine, N.E. Paton, J.C. Williams, The omega phase transformation in titanium alloys as an example of displacement controlled reactions, Acta Metall. 19 (1971) 1153–1162. https://doi.org/10.1016/0001-6160(71)90047-2.

[16] J.M. Silcock, An X-ray examination of the to phase in TiV, TiMo and TiCr alloys, Acta Metall. 6 (1958) 481–493.

[17] J.A. Bagarjatskij, G.I. Nosova, T. V Tagunova, On the nature of the omega phase in quenched titanium alloys, Acta Crystallogr. 14 (1961) 1087–1088.

[18] J.C. Williams, B.S. Hickman, H.L. Marcus, The effect of omega phase on the mechanical properties of titanium alloys, Metall. Trans. 2 (1971) 1913–1919.

[19] B.S. Hickman, The formation of omega phase in titanium and zirconium alloys: A review, J. Mater. Sci. 4 (1969) 554–563.

[20] F.R. Brotzen, E.L. Harmon, A.R. Troiano, Decomposition of beta titanium, JOM. 7 (1955) 413–419.

[21] T.S. Kuan, R.R. Ahrens, S.L. Sass, The stress-induced omega phase transformation in Ti-V alloys, Metall. Trans. A. 6 (1975) 1767.

[22] J.C. Jamieson, Crystal structures of titanium, zirconium, and hafnium at high pressures, Science (80-.). 140 (1963) 72–73.

[23] S.L. Semiatin, V. Seetharaman, I. Weiss, The thermomechanical processing of alpha/beta titanium alloys, Jom. 49 (1997) 33–39.

[24] W.J. Evans, Optimising mechanical properties in alpha+ beta titanium alloys, Mater. Sci. Eng. A. 243 (1998) 89–96.

[25] J.A. Hall, Fatigue crack initiation in alpha-beta titanium alloys, Int. J. Fatigue. 19 (1997) 23–37.

[26] F.H. Froes, H.B. Bomberger, The beta titanium alloys, JOM. 37 (1985) 28–37.

[27] R.R. Boyer, Aerospace applications of beta titanium alloys, JOM. 46 (1994) 20–23. https://doi.org/10.1007/BF03220743.

[28] J.I. Qazi, H.J. Rack, B. Marquardt, High-strength metastable beta-titanium alloys for biomedical applications, JOM. 56 (2004) 49–51. https://doi.org/10.1007/s11837-004-0253-9.

[29] P.J. Bania, Beta titanium alloys and their role in the titanium industry, Jom. 46 (1994) 16–19.

[30] W.D. Zeng, Y.G. Zhou, Effect of beta flecks on mechanical properties of Ti-10V-2Fe-3Al alloy, Mater. Sci. Eng. A. 260 (1999) 203–211. https://doi.org/10.1016/s0921-5093(98)00954-x.

[31] A. Mitchell, A. Kawakami, S.L. Cockcroft, Beta fleck and segregation in titanium alloy ingots, High Temp. Mater. Process. 25 (2006) 337–349.

[32] W. Zeng, Y. Zhou, H. Yu, Effect of Beta Flecks on Low-Cycle Fatigue Properties of Ti-10V-2Fe-3Al, J. Mater. Eng. Perform. 9 (2000) 222–227. https://doi.org/10.1361/105994900770346187.

[33] C.H. Ng, M.J. Bermingham, M.S. Dargusch, Eliminating segregation defects during additive manufacturing of high strength β-titanium alloys, Addit. Manuf. 39 (2021) 101855. https://doi.org/https://doi.org/10.1016/j.addma.2021.101855.

[34] W.J. Sames, F.A. List, S. Pannala, R.R. Dehoff, S.S. Babu, The metallurgy and processing science of metal additive manufacturing, Int. Mater. Rev. 61 (2016) 315–360. https://doi.org/10.1080/09506608.2015.1116649.

[35] J.C. Nelson, N.K. Vail, J.W. Barlow, J.J. Beaman, D.L. Bourell, H.L. Marcus, Selective laser sintering of polymer-coated silicon carbide powders, Ind. Eng. Chem. Res. 34 (1995) 1641–1651.

[36] J.J. Beaman, J.W. Barlow, D.L. Bourell, R.H. Crawford, H.L. Marcus, K.P. McAlea, Solid freeform fabrication: a new direction in manufacturing, Kluwer Acad. Publ. Norwell, MA. 2061 (1997) 25–49.

[37] I.A. Manriquez-Frayre, D.L. Bourell, Selective Laser Sintering of Binary Metallic Powder, in: 1990 Int. Solid Free. Fabr. Symp., 1990. http://hdl.handle.net/2152/64245%0A (accessed April 26, 2021).

[38] E.M. Sachs, J.S. Haggerty, M.J. Cima, P.A. Williams, Three-dimensional printing techniques, (1993).

[39] S.N. Laboratories, Creating a Complex Metal Part in a Day is Goal of Commercial Consortium, (1997).

[40] C. Atwood, M. Griffith, L. Harwell, E. Schlienger, M. Ensz, J. Smugeresky, T. Romero, D. Greene, D. Reckaway, Laser engineered net shaping (LENS^{TM}): A tool for direct fabrication of metal parts, in: Int. Congr. Appl. Lasers Electro-Optics, Laser Institute of America, 2018: pp. E1–E7. https://doi.org/10.2351/1.5059147.

[41] T. Himmer, T. Nakagawa, M. Anzai, Lamination of metal sheets, Comput. Ind. 39 (1999) 27–33.

[42] B. Mueller, D. Kochan, Laminated object manufacturing for rapid tooling and patternmaking in foundry industry, Comput. Ind. 39 (1999) 47–53.

[43] B. Xu, X. Wu, J. Lei, F. Luo, F. Gong, C. Du, X. Sun, S. Ruan, Research on micro-electric resistance slip welding of copper electrode during the fabrication of 3D metal micro-mold, J. Mater. Process. Technol. 213 (2013) 2174–2183.

[44] D.R. White, Ultrasonic consolidation of aluminum tooling, Adv. Mater. Process. 161 (2003) 64–66.

[45] Standard Terminology for Additive Manufacturing Technologies, (n.d.).

[46] H.-S. Park, D.-S. Nguyen, Study on flaking behavior in Selective Laser Melting process, Procedia CIRP. 63 (2017) 569–572.

[47] W.J. Sames, F.A. List, S. Pannala, R.R. Dehoff, S.S. Babu, The metallurgy and processing science of metal additive manufacturing, Int. Mater. Rev. 61 (2016) 315–360. https://doi.org/10.1080/09506608.2015.1116649.

[48] R. Grylls, Laser Engineered Net Shapes: Laser Engineered Net Shaping is an additive manufacturing process that makes fully dense metal parts and repairs delicate components, Adv. Mater. Process. 161 (2003) 45–48.

[49] A. Dass, A. Moridi, State of the Art in Directed Energy Deposition: From Additive Manufacturing to Materials Design, Coatings . 9 (2019). https://doi.org/10.3390/coatings9070418.

[50] A. Saboori, A. Aversa, G. Marchese, S. Biamino, M. Lombardi, P. Fino, Application of directed energy deposition-based additive manufacturing in repair, Appl. Sci. 9 (2019) 3316.

[51] C. Schneider-Maunoury, L. Weiss, P. Acquier, D. Boisselier, P. Laheurte, Functionally graded Ti6Al4V-Mo alloy manufactured with DED-CLAD ® process, Addit. Manuf. 17 (2017) 55–66. https://doi.org/10.1016/j.addma.2017.07.008.

[52] D. Mahmoud, M. Elbestawi, Lattice Structures and Functionally Graded Materials Applications in Additive Manufacturing of Orthopedic Implants: A Review, J. Manuf. Mater. Process. 1 (2017) 13. https://doi.org/10.3390/jmmp1020013.

[53] A. Bandyopadhyay, B. V Krishna, W. Xue, S. Bose, Application of Laser Engineered Net Shaping (LENS) to manufacture porous and functionally graded structures for load bearing implants, J. Mater. Sci. Mater. Med. 20 (2008) 29. https://doi.org/10.1007/s10856-008-3478-2.

[54] B. Saleh, J. Jiang, R. Fathi, T. Al-hababi, Q. Xu, L. Wang, D. Song, A. Ma, 30 Years of functionally graded materials: An overview of manufacturing methods, Applications and Future Challenges, Compos. Part B Eng. 201 (2020) 108376. https://doi.org/https://doi.org/10.1016/j.compositesb.2020.108376.

[55] Y.-J. Liang, X.-J. Tian, Y.-Y. Zhu, J. Li, H.-M. Wang, Compositional variation and microstructural evolution in laser additive manufactured Ti/Ti–6Al–2Zr–1Mo–1V graded structural material, Mater. Sci. Eng. A. 599 (2014) 242–246.

[56] D.D. Lima, S.A. Mantri, C. V Mikler, R. Contieri, C.J. Yannetta, K.N. Campo, E.S. Lopes, M.J. Styles, T. Borkar, R. Caram, R. Banerjee, Laser additive processing of a functionally graded internal fracture fixation plate, Mater. Des. 130 (2017) 8–15. https://doi.org/https://doi.org/10.1016/j.matdes.2017.05.034.

[57] V. Chaudhary, N.M. Sai Kiran Kumar Yadav, S.A. Mantri, S. Dasari, A. Jagetia, R. V Ramanujan, R. Banerjee, Additive manufacturing of functionally graded Co–Fe and Ni–Fe magnetic materials, J. Alloys Compd. 823 (2020) 153817. https://doi.org/https://doi.org/10.1016/j.jallcom.2020.153817.

[58] T. DebRoy, H.L. Wei, J.S. Zuback, T. Mukherjee, J.W. Elmer, J.O. Milewski, A.M. Beese, A. Wilson-Heid, A. De, W. Zhang, Additive manufacturing of metallic components – Process, structure and properties, Prog. Mater. Sci. 92 (2018) 112–224. https://doi.org/10.1016/j.pmatsci.2017.10.001.

[59] M.S.K.K.Y. Nartu, D. Flannery, S. Mazumder, S.A. Mantri, S.S. Joshi, A. V. Ayyagari, B. McWilliams, K. Cho, N.B. Dahotre, R. Banerjee, Influence of Process Parameters on Mechanical and Corrosion Behavior of DED-Processed Biomedical Ti-35Nb-7Zr-5Ta Alloy, JOM. (2021) 1–9. https://doi.org/10.1007/s11837-021-04675-1.

[60] S.A. Mantri, T. Alam, Y. Zheng, J.C. Williams, R. Banerjee, Influence of post deposition annealing on microstructure and properties of laser additively manufactured titanium copper alloys, Addit. Manuf. 32 (2020) 101067. https://doi.org/https://doi.org/10.1016/j.addma.2020.101067.

[61] S.A. Mantri, R. Banerjee, Microstructure and micro-texture evolution of additively manufactured β-Ti alloys, Addit. Manuf. 23 (2018) 86–98. https://doi.org/https://doi.org/10.1016/j.addma.2018.07.013.

[62] H. Galarraga, D.A. Lados, R.R. Dehoff, M.M. Kirka, P. Nandwana, Effects of the microstructure and porosity on properties of Ti-6Al-4V ELI alloy fabricated by electron beam melting (EBM), Addit. Manuf. 10 (2016) 47–57. https://doi.org/10.1016/J.ADDMA.2016.02.003.

[63] A.A. Antonysamy, J. Meyer, P.B. Prangnell, Effect of build geometry on the β-grain structure and texture in additive manufacture of Ti6Al4V by selective electron beam melting, Mater. Charact. 84 (2013) 153–168. https://doi.org/10.1016/J.MATCHAR.2013.07.012.

[64] J.J. Valencia, P.N. Quested, Thermophysical Properties, Met. Process Simul. 22B (2010) 0. https://doi.org/10.31399/asm.hb.v22b.a0005523.

[65] L. Wang, S. Felicelli, Process modeling in laser deposition of multilayer SS410 steel, J. Manuf. Sci. Eng. Trans. ASME. 129 (2007) 1028–1034. https://doi.org/10.1115/1.2738962.

[66] M.S.K.K.Y. Nartu, T. Alam, S. Dasari, S.A. Mantri, S. Gorsse, H. Siller, N. Dahotre, R. Banerjee, Enhanced tensile yield strength in laser additively manufactured Al0.3CoCrFeNi high entropy alloy, Materialia. 9 (2020) 100522. https://doi.org/https://doi.org/10.1016/j.mtla.2019.100522.

[67] M.S.K.K.Y. Nartu, A. Jagetia, V. Chaudhary, S.A. Mantri, E. Ivanov, N.B. Dahotre, R. V Ramanujan, R. Banerjee, Magnetic and mechanical properties of an additively

manufactured equiatomic CoFeNi complex concentrated alloy, Scr. Mater. 187 (2020) 30–36. https://doi.org/https://doi.org/10.1016/j.scriptamat.2020.05.063.

[68] M.S.K.K.Y. Nartu, S. Dasari, A. Sharma, S.A. Mantri, S. Sharma, M. V. Pantawane, B. McWilliams, K. Cho, N.B. Dahotre, R. Banerjee, Omega versus alpha precipitation mediated by process parameters in additively manufactured high strength Ti–1Al–8V–5Fe alloy and its impact on mechanical properties, Mater. Sci. Eng. A. (2021) 141627. https://doi.org/10.1016/j.msea.2021.141627.

[69] V. Chaudhary, S.A. Mantri, R. V. Ramanujan, R. Banerjee, Additive manufacturing of magnetic materials, Prog. Mater. Sci. 114 (2020) 100688. https://doi.org/10.1016/j.pmatsci.2020.100688.

[70] G. Muvvala, D. Patra Karmakar, A.K. Nath, Online monitoring of thermo-cycles and its correlation with microstructure in laser cladding of nickel based super alloy, Opt. Lasers Eng. 88 (2017) 139–152. https://doi.org/10.1016/J.OPTLASENG.2016.08.005.

[71] J.E. Craig, T. Wakeman, R. Grylls, J. Bullen, Online Imaging Pyrometer for Laser Deposition Processing, Sensors, Sampling, Simul. Process Control. (2011) 103–110. https://doi.org/10.1002/9781118061800.CH12.

[72] L. Wang, S. Felicelli, Y. Gooroochurn, P.T. Wang, M.F. Horstemeyer, Optimization of the LENS® process for steady molten pool size, Mater. Sci. Eng. A. 474 (2008) 148–156. https://doi.org/10.1016/J.MSEA.2007.04.119.

[73] M.S.K.K.Y. Nartu, S.A. Mantri, M. V. Pantawane, Y.H. Ho, B. McWilliams, K. Cho, N.B. Dahotre, R. Banerjee, In situ reactions during direct laser deposition of Ti-B4C composites, Scr. Mater. 183 (2020) 28–32. https://doi.org/10.1016/j.scriptamat.2020.03.021.

[74] W.J. Sames, F.A. List, S. Pannala, R.R. Dehoff, S.S. Babu, The metallurgy and processing science of metal additive manufacturing, Int. Mater. Rev. 61 (2016) 315–360. https://doi.org/10.1080/09506608.2015.1116649.

[75] M. Bermingham, D. StJohn, M. Easton, L. Yuan, M. Dargusch, Revealing the Mechanisms of Grain Nucleation and Formation During Additive Manufacturing, JOM 2020 723. 72 (2020) 1065–1073. https://doi.org/10.1007/S11837-020-04019-5.

[76] M.A. Martorano, C. Beckermann, C.-A. Gandin, A solutal interaction mechanism for the columnar-to-equiaxed transition in alloy solidification, Metall. Mater. Trans. A 2003 348. 34 (2003) 1657–1674. https://doi.org/10.1007/S11661-003-0311-X.

[77] W.D. Griffiths, D.G. McCartney, The effect of electromagnetic stirring on macrostructure and macrosegregation in the aluminium alloy 7150, Mater. Sci. Eng. A. 222 (1997) 140–148. https://doi.org/10.1016/S0921-5093(96)10527-X.

[78] C.Y. Wang, C. Beckermann, Prediction of Columnar to Equiaxed Transition during Diffusion-Controlled Dendritic Alloy Solidification, (n.d.).

[79] J.A. Spittle, M.R. Tadayon, Observations on the numerical prediction of the columnar to equiaxed grain transition in castings, Http://Dx.Doi.Org/10.1080/09534962.1994.11819170. 7 (2016) 123–126. https://doi.org/10.1080/09534962.1994.11819170.

[80] Y. Chen, S. Zhang, H. Song, M. Cheng, H. Li, J. Liu, Sudden transition from columnar to equiaxed grain of cast copper induced by rare earth microalloying, Mater. Des. 91 (2016) 314–320. https://doi.org/10.1016/J.MATDES.2015.11.083.

[81] J.A. Spittle, Columnar to equiaxed grain transition in as solidified alloys, Http://Dx.Doi.Org/10.1179/174328006X102493. 51 (2013) 247–269. https://doi.org/10.1179/174328006X102493.

[82] H.B. Dong, P.D. Lee, Simulation of the columnar-to-equiaxed transition in directionally solidified Al–Cu alloys, Acta Mater. 53 (2005) 659–668. https://doi.org/10.1016/J.ACTAMAT.2004.10.019.

[83] O. Satbhai, S. Roy, S. Ghosh, A parametric multi-scale, multiphysics numerical investigation in a casting process for Al-Si alloy and a macroscopic approach for prediction of ECT and CET events, Appl. Therm. Eng. 113 (2017) 386–412. https://doi.org/10.1016/J.APPLTHERMALENG.2016.11.003.

[84] D.H. Stjohn, M. Qian, M.A. Easton, P. Cao, The Interdependence Theory: The relationship between grain formation and nucleant selection, Acta Mater. 59 (2011) 4907–4921. https://doi.org/10.1016/J.ACTAMAT.2011.04.035.

[85] J.W. Rutter, B. Chalmers, A PRISMATIC SUBSTRUCTURE FORMED DURING SOLIDIFICATION OF METALS, Can. J. Phys. 31 (1953) 15–39. https://doi.org/10.1139/P53-003.

[86] W.A. Tiller, K.A. Jackson, J.W. Rutter, B. Chalmers, The redistribution of solute atoms during the solidification of metals, Acta Metall. 1 (1953) 428–437. https://doi.org/10.1016/0001-6160(53)90126-6.

[87] A.L. Greer, A.M. Bunn, A. Tronche, P. V. Evans, D.J. Bristow, Modelling of inoculation of metallic melts: application to grain refinement of aluminium by Al–Ti–B, Acta Mater. 48 (2000) 2823–2835. https://doi.org/10.1016/S1359-6454(00)00094-X.

[88] M.A. Easton, D.H. Stjohn, A model of grain refinement incorporating alloy constitution and potency of heterogeneous nucleant particles, Acta Mater. 49 (2001) 1867–1878. https://doi.org/10.1016/S1359-6454(00)00368-2.

[89] I. Maxwell, A. Hellawell, A simple model for grain refinement during solidification, Acta Metall. 23 (1975) 229–237. https://doi.org/10.1016/0001-6160(75)90188-1.

[90] J.A. Spittle, S. Sadli, Effect of alloy variables on grain refinement of binary aluminium alloys with Al–Ti–B, Http://Dx.Doi.Org/10.1179/Mst.1995.11.6.533. 11 (2013) 533–537. https://doi.org/10.1179/MST.1995.11.6.533.

[91] L.A. Tarshis, J.L. Walker, J.W. Rutter, Experiments on the solidification structure of alloy castings, Metall. Trans. 1971 29. 2 (1971) 2589–2597. https://doi.org/10.1007/BF02814899.

[92] M. Easton, D. StJohn, Grain refinement of aluminum alloys: Part II. Confirmation of, and a mechanism for, the solute paradigm, Metall. Mater. Trans. A 1999 306. 30 (1999) 1625–1633. https://doi.org/10.1007/S11661-999-0099-4.

[93] A.L. Greer, Grain refinement of alloys by inoculation of melts, Philos. Trans. R. Soc. London. Ser. A Math. Phys. Eng. Sci. 361 (2003) 479–495. https://doi.org/10.1098/RSTA.2002.1147.

[94] M. Easton, D. StJohn, An analysis of the relationship between grain size, solute content, and the potency and number density of nucleant particles, Metall. Mater. Trans. A 2005 367. 36 (2005) 1911–1920. https://doi.org/10.1007/S11661-005-0054-Y.

[95] M. Qian, J. Ma, Heterogeneous nucleation on convex spherical substrate surfaces: A rigorous thermodynamic formulation of Fletcher's classical model and the new perspectives derived, J. Chem. Phys. 130 (2009) 214709. https://doi.org/10.1063/1.3146810.

[96] M. Qian, P. Cao, M.A. Easton, S.D. McDonald, D.H. StJohn, An analytical model for constitutional supercooling-driven grain formation and grain size prediction, Acta Mater. 58 (2010) 3262–3270. https://doi.org/10.1016/J.ACTAMAT.2010.01.052.

[97] M. Easton, D. StJohn, An analysis of the relationship between grain size, solute content, and the potency and number density of nucleant particles, Metall. Mater. Trans. A 2005 367. 36 (2005) 1911–1920. https://doi.org/10.1007/S11661-005-0054-Y.

[98] A.L. Greer, Grain refinement of alloys by inoculation of melts, Philos. Trans. R. Soc. London. Ser. A Math. Phys. Eng. Sci. 361 (2003) 479–495. https://doi.org/10.1098/RSTA.2002.1147.

[99] P. Desnain, Y. Fautrelle, J.L. Meyer, J.P. Riquet, F. Durand, Prediction of equiaxed grain density in multicomponent alloys, stirred electromagnetically, Acta Metall. Mater. 38 (1990) 1513–1523. https://doi.org/10.1016/0956-7151(90)90119-2.

[100] T.E. Quested, A.T. Dinsdale, A.L. Greer, Thermodynamic modelling of growth-restriction effects in aluminium alloys, Acta Mater. 53 (2005) 1323–1334. https://doi.org/10.1016/J.ACTAMAT.2004.11.024.

[101] R. Schmid-Fetzer, A. Kozlov, Thermodynamic aspects of grain growth restriction in multicomponent alloy solidification, Acta Mater. 59 (2011) 6133–6144. https://doi.org/10.1016/J.ACTAMAT.2011.06.026.

[102] S.A. Mantri, T. Alam, D. Choudhuri, C.J. Yannetta, C. V. Mikler, P.C. Collins, R. Banerjee, The effect of boron on the grain size and texture in additively manufactured β-

Ti alloys, J. Mater. Sci. 2017 5220. 52 (2017) 12455–12466. https://doi.org/10.1007/S10853-017-1371-4.

[103] M.Y. Mendoza, P. Samimi, D.A. Brice, B.W. Martin, M.R. Rolchigo, R. LeSar, P.C. Collins, Microstructures and Grain Refinement of Additive-Manufactured Ti-xW Alloys, Metall. Mater. Trans. A 2017 487. 48 (2017) 3594–3605. https://doi.org/10.1007/S11661-017-4117-7.

[104] M. Bermingham, D. StJohn, M. Easton, L. Yuan, M. Dargusch, Revealing the Mechanisms of Grain Nucleation and Formation During Additive Manufacturing, JOM 2020 723. 72 (2020) 1065–1073. https://doi.org/10.1007/S11837-020-04019-5.

[105] D. Zhang, D. Qiu, M.A. Gibson, Y. Zheng, H.L. Fraser, D.H. StJohn, M.A. Easton, Additive manufacturing of ultrafine-grained high-strength titanium alloys, Nat. 2019 5767785. 576 (2019) 91–95. https://doi.org/10.1038/s41586-019-1783-1.

[106] D. Zhang, A. Prasad, M.J. Bermingham, C.J. Todaro, M.J. Benoit, M.N. Patel, D. Qiu, D.H. StJohn, M. Qian, M.A. Easton, Grain Refinement of Alloys in Fusion-Based Additive Manufacturing Processes, Metall. Mater. Trans. A 2020 519. 51 (2020) 4341–4359. https://doi.org/10.1007/S11661-020-05880-4.

[107] A. Prasad, L. Yuan, P. Lee, M. Patel, D. Qiu, M. Easton, D. StJohn, Towards understanding grain nucleation under Additive Manufacturing solidification conditions, Acta Mater. 195 (2020) 392–403. https://doi.org/10.1016/J.ACTAMAT.2020.05.012.

[108] D.A. Porter, K.E. Easterling, M. Sherif, Phase transformations in metals and alloys (Revised Reprint), CRC press, 2009.

[109] R.P. Kolli, A. Devaraj, A review of metastable beta titanium alloys, Metals (Basel). 8 (2018) 1–41. https://doi.org/10.3390/met8070506.

[110] P. Laheurte, F. Prima, A. Eberhardt, T. Gloriant, M. Wary, E. Patoor, Mechanical properties of low modulus β titanium alloys designed from the electronic approach, J. Mech. Behav. Biomed. Mater. 3 (2010) 565–573. https://doi.org/https://doi.org/10.1016/j.jmbbm.2010.07.001.

[111] D. Kuroda, M. Niinomi, M. Morinaga, Y. Kato, T. Yashiro, Design and mechanical properties of new β type titanium alloys for implant materials, Mater. Sci. Eng. A. 243 (1998) 244–249. https://doi.org/https://doi.org/10.1016/S0921-5093(97)00808-3.

[112] O.M. Ivasishin, P.E. Markovsky, Y.V. Matviychuk, S.L. Semiatin, C.H. Ward, S. Fox, A comparative study of the mechanical properties of high-strength β-titanium alloys, J. Alloys Compd. 457 (2008) 296–309. https://doi.org/https://doi.org/10.1016/j.jallcom.2007.03.070.

[113] F.H. Froes, Titanium: physical metallurgy, processing, and applications, ASM international, 2015.

[114] The Use of β Titanium Alloys in the Aerospace Industry, J. Mater. Eng. Perform. 22 (2013) 2916–2920. https://doi.org/10.1007/s11665-013-0728-3.

[115] R.R. Boyer, R.D. Briggs, The use of β titanium alloys in the aerospace industry, in: J. Mater. Eng. Perform., Springer, 2005: pp. 681–685. https://doi.org/10.1361/105994905X75448.

[116] A. Mitchell, A. Kawakami, S.L. Cockcroft, Segregation in titanium alloy ingots, High Temp. Mater. Process. 26 (2007) 59–78.

[117] S.R. Seagle, K.O. Yu, S. Giangiordano, Considerations in processing titanium, Mater. Sci. Eng. A. 263 (1999) 237–242. https://doi.org/https://doi.org/10.1016/S0921-5093(98)01154-X.

[118] A. Mitchell, Melting, casting and forging problems in titanium alloys, Mater. Sci. Eng. A. 243 (1998) 257–262. https://doi.org/https://doi.org/10.1016/S0921-5093(97)00810-1.

[119] C.C. Chen, R.R. Boyer, PRACTICAL CONSIDERATIONS FOR MANUFACTURING HIGH-STRENGTH TI-10V-2Fe-3Al ALLOY FORGINGS., J Met. 31 (1979) 33–39. https://doi.org/10.1007/bf03354533.

[120] C.H. Ng, M.J. Bermingham, M.S. Dargusch, Eliminating segregation defects during additive manufacturing of high strength β-titanium alloys, Addit. Manuf. 39 (2021) 101855. https://doi.org/10.1016/j.addma.2021.101855.

[121] C.E. Shamblen, Minimizing beta flecks in the ti-17 alloy, Metall. Mater. Trans. B Process Metall. Mater. Process. Sci. 28 (1997) 899–903. https://doi.org/10.1007/s11663-997-0017-3.

[122] V. V Joshi, C. Lavender, V. Moxon, V. Duz, E. Nyberg, K.S. Weil, Development of Ti-6Al-4V and Ti-1Al-8V-5Fe alloys using low-cost TiH 2 powder feedstock, J. Mater. Eng. Perform. 22 (2013) 995–1003.

[123] A. Devaraj, V. V Joshi, A. Srivastava, S. Manandhar, V. Moxson, V.A. Duz, C. Lavender, A low-cost hierarchical nanostructured beta-titanium alloy with high strength, Nat. Commun. 7 (2016) 11176.

[124] H. Azizi, H. Zurob, B. Bose, S. Reza Ghiaasiaan, X. Wang, S. Coulson, V. Duz, A.B. Phillion, Additive manufacturing of a novel Ti-Al-V-Fe alloy using selective laser melting, Addit. Manuf. 21 (2018) 529–535. https://doi.org/https://doi.org/10.1016/j.addma.2018.04.006.

[125] D. Zhang, D. Qiu, M.A. Gibson, Y. Zheng, H.L. Fraser, D.H. StJohn, M.A. Easton, Additive manufacturing of ultrafine-grained high-strength titanium alloys, Nature. 576 (2019) 91–95. https://doi.org/10.1038/s41586-019-1783-1.

[126] F.H. Froes, Titanium powder Metallurgy-Products, Met. Powder Rep. 42 (1987) 676–686.

[127] W.E. Frazier, Metal additive manufacturing: a review, J. Mater. Eng. Perform. 23 (2014) 1917–1928.

[128] M. Simonelli, Y.Y. Tse, C. Tuck, On the Texture Formation of Selective Laser Melted Ti-6Al-4V, Metall. Mater. Trans. A. 45 (2014) 2863–2872. https://doi.org/10.1007/s11661-014-2218-0.

[129] T.M. Butler, C.A. Brice, W.A. Tayon, S.L. Semiatin, A.L. Pilchak, Evolution of Texture from a Single Crystal Ti-6Al-4V Substrate During Electron Beam Directed Energy Deposition, Metall. Mater. Trans. A. 48 (2017) 4441–4446. https://doi.org/10.1007/s11661-017-4219-2.

[130] N. Sridharan, A. Chaudhary, P. Nandwana, S.S. Babu, Texture Evolution During Laser Direct Metal Deposition of Ti-6Al-4V, JOM. 68 (2016) 772–777. https://doi.org/10.1007/s11837-015-1797-6.

[131] L. Thijs, F. Verhaeghe, T. Craeghs, J. Van Humbeeck, J.-P. Kruth, A study of the microstructural evolution during selective laser melting of Ti–6Al–4V, Acta Mater. 58 (2010) 3303–3312.

[132] Y. Chew, G. Bi, Z.G. Zhu, F. Ng, F. Weng, S.B. Liu, M.L.S. Nai, B.Y. Lee, Microstructure and Enhanced Strength of Laser Aided Additive Manufactured CoCrFeNiMn High Entropy Alloy, Mater. Sci. Eng. A. 744 (2018). https://doi.org/10.1016/j.msea.2018.12.005.

[133] S.M. Thompson, L. Bian, N. Shamsaei, A. Yadollahi, An overview of Direct Laser Deposition for additive manufacturing; Part I: Transport phenomena, modeling and diagnostics, Addit. Manuf. 8 (2015) 36–62.

[134] N. Shamsaei, A. Yadollahi, L. Bian, S.M. Thompson, An overview of Direct Laser Deposition for additive manufacturing; Part II: Mechanical behavior, process parameter optimization and control, Addit. Manuf. 8 (2015) 12–35.

[135] D.D. Gu, W. Meiners, K. Wissenbach, R. Poprawe, Laser additive manufacturing of metallic components: materials, processes and mechanisms, Int. Mater. Rev. 57 (2012) 133–164.

[136] T. Wang, Y.Y. Zhu, S.Q. Zhang, H.B. Tang, H.M. Wang, Grain morphology evolution behavior of titanium alloy components during laser melting deposition additive manufacturing, J. Alloys Compd. 632 (2015) 505–513.

[137] L. Ladani, J. Razmi, S.F. Choudhury, Mechanical anisotropy and strain rate dependency behavior of Ti6Al4V produced using E-beam additive fabrication, J. Eng. Mater. Technol. Trans. ASME. 136 (2014). https://doi.org/10.1115/1.4027729.

[138] L. Ladani, Local and Global Mechanical Behavior and Microstructure of Ti6Al4V Parts Built Using Electron Beam Melting Technology, Metall. Mater. Trans. A Phys. Metall. Mater. Sci. 46 (2015) 3835–3841. https://doi.org/10.1007/s11661-015-2965-6.

[139] P.C. Collins, D.A. Brice, P. Samimi, I. Ghamarian, H.L. Fraser, Microstructural control of additively manufactured metallic materials, Annu. Rev. Mater. Res. 46 (2016) 63–91.

[140] X. Wu, R. Sharman, J. Mei, W. Voice, Microstructure and properties of a laser fabricated burn-resistant Ti alloy, Mater. Des. 25 (2004) 103–109.

[141] S.A. Mantri, T. Alam, D. Choudhuri, C.J. Yannetta, C. V Mikler, P.C. Collins, R. Banerjee, The effect of boron on the grain size and texture in additively manufactured β-Ti alloys, J. Mater. Sci. 52 (2017) 12455–12466. https://doi.org/10.1007/s10853-017-1371-4.

[142] S. Nag, S. Samuel, A. Puthucode, R. Banerjee, Characterization of novel borides in Ti–Nb–Zr–Ta+2B metal-matrix composites, Mater. Charact. 60 (2009) 106–113. https://doi.org/https://doi.org/10.1016/j.matchar.2008.07.011.

[143] Y.-Y. Zhu, H.-B. Tang, Z. Li, C. Xu, B. He, Solidification behavior and grain morphology of laser additive manufacturing titanium alloys, J. Alloys Compd. 777 (2019) 712–716. https://doi.org/https://doi.org/10.1016/j.jallcom.2018.11.055.

[144] W. Kurz, C. Bezencon, M. Gäumann, Columnar to equiaxed transition in solidification processing, Sci. Technol. Adv. Mater. 2 (2001) 185.

[145] M. Gäumann, C. Bezencon, P. Canalis, W. Kurz, Single-crystal laser deposition of superalloys: processing–microstructure maps, Acta Mater. 49 (2001) 1051–1062.

[146] Y. Zhu, D. Liu, X. Tian, H. Tang, H. Wang, Characterization of microstructure and mechanical properties of laser melting deposited Ti–6.5 Al–3.5 Mo–1.5 Zr–0.3 Si titanium alloy, Mater. Des. 56 (2014) 445–453.

[147] C.M. Liu, X.J. Tian, H.B. Tang, H.M. Wang, Microstructural characterization of laser melting deposited Ti–5Al-5Mo–5V–1Cr–1Fe near β titanium alloy, J. Alloys Compd. 572 (2013) 17–24.

[148] Y. Zhu, C. Bo, H. Tang, X. Cheng, H. Wang, L.I. Jia, Influence of heat treatments on microstructure and mechanical properties of laser additive manufacturing Ti-5Al-2Sn-2Zr-4Mo-4Cr titanium alloy, Trans. Nonferrous Met. Soc. China. 28 (2018) 36–46.

[149] C. Qiu, G.A. Ravi, M.M. Attallah, Microstructural control during direct laser deposition of a β-titanium alloy, Mater. Des. 81 (2015) 21–30.

[150] J. Romano, L. Ladani, M. Sadowski, Laser Additive Melting and Solidification of Inconel 718: Finite Element Simulation and Experiment, JOM. 68 (2016) 967–977. https://doi.org/10.1007/s11837-015-1765-1.

[151] L. Ladani, J. Romano, W. Brindley, S. Burlatsky, Effective liquid conductivity for improved simulation of thermal transport in laser beam melting powder bed technology, Addit. Manuf. 14 (2017) 13–23. https://doi.org/10.1016/j.addma.2016.12.004.

[152] V. Manvatkar, A. De, T. DebRoy, Spatial variation of melt pool geometry, peak temperature and solidification parameters during laser assisted additive manufacturing process, Mater. Sci. Technol. (United Kingdom). 31 (2015) 924–930. https://doi.org/10.1179/1743284714Y.0000000701.

[153] V. Manvatkar, A. De, T. Debroy, Heat transfer and material flow during laser assisted multi-layer additive manufacturing, J. Appl. Phys. 116 (2014) 64904. https://doi.org/10.1063/1.4896751.

[154] S. Sharma, V. Mandal, S.A. Ramakrishna, J. Ramkumar, Numerical simulation of melt hydrodynamics induced hole blockage in Quasi-CW fiber laser micro-drilling of TiAl6V4, J. Mater. Process. Technol. 262 (2018) 131–148. https://doi.org/10.1016/j.jmatprotec.2018.06.038.

[155] Z. Gan, G. Yu, X. He, S. Li, Numerical simulation of thermal behavior and multicomponent mass transfer in direct laser deposition of Co-base alloy on steel, Int. J. Heat Mass Transf. 104 (2017) 28–38. https://doi.org/10.1016/j.ijheatmasstransfer.2016.08.049.

[156] Z. Gan, H. Liu, S. Li, X. He, G. Yu, Modeling of thermal behavior and mass transport in multi-layer laser additive manufacturing of Ni-based alloy on cast iron, Int. J. Heat Mass Transf. 111 (2017) 709–722. https://doi.org/10.1016/j.ijheatmasstransfer.2017.04.055.

[157] P. Michaleris, Modeling metal deposition in heat transfer analyses of additive manufacturing processes, Finite Elem. Anal. Des. 86 (2014) 51–60. https://doi.org/10.1016/j.finel.2014.04.003.

[158] M. V Pantawane, Y.-H. Ho, S.S. Joshi, N.B. Dahotre, Computational Assessment of Thermokinetics and Associated Microstructural Evolution in Laser Powder Bed Fusion Manufacturing of Ti6Al4V Alloy, Sci. Rep. 10 (2020) 7579. https://doi.org/10.1038/s41598-020-63281-4.

[159] N.B.D. Mangesh V.Pantawane, Shashank Sharma, Sriswaroop Dasari, Srinivas Aditya Mantri, Abhishek Sharma, Rajarshi Banerjee, Srikumar Banerjee, Spatial variation of Thermokinetics and associated microstructural evolution in laser surface engineered IN718: precursor for additive manufacturing, Metall. Mater. Trans. A. (2021). https://doi.org/10.1007/s11661-021-06227-3.

[160] M. V. Pantawane, S. Sharma, A. Sharma, S. Dasari, S. Banerjee, R. Banerjee, N.B. Dahotre, Coarsening of Martensite with Multiple Generations of Twins in Laser Additively Manufactured Ti6Al4V, Acta Mater. (2021) 116954. https://doi.org/10.1016/j.actamat.2021.116954.

[161] S. Nag, A. Devaraj, R. Srinivasan, R.E.A. Williams, N. Gupta, G.B. Viswanathan, J.S. Tiley, S. Banerjee, S.G. Srinivasan, H.L. Fraser, R. Banerjee, Novel Mixed-Mode Phase Transition Involving a Composition-Dependent Displacive Component, Phys. Rev. Lett. 106 (2011) 245701. https://doi.org/10.1103/PhysRevLett.106.245701.

[162] A. Devaraj, S. Nag, R. Srinivasan, R.E.A. Williams, S. Banerjee, R. Banerjee, H.L. Fraser, Experimental evidence of concurrent compositional and structural instabilities leading to ω precipitation in titanium-molybdenum alloys, Acta Mater. 60 (2012) 596–609. https://doi.org/10.1016/j.actamat.2011.10.008.

[163] D. Choudhuri, Y. Zheng, T. Alam, R. Shi, M. Hendrickson, S. Banerjee, Y. Wang, S.G. Srinivasan, H. Fraser, R. Banerjee, Coupled experimental and computational investigation of omega phase evolution in a high misfit titanium-vanadium alloy, Acta Mater. 130 (2017) 215–228. https://doi.org/https://doi.org/10.1016/j.actamat.2017.03.047.

[164] J.C. Williams, D. de Fontaine, N.E. Paton, The ω-phase as an example of an unusual shear transformation, Metall. Trans. 4 (1973) 2701–2708. https://doi.org/10.1007/BF02644570.

[165] M.J. Lai, T. Li, D. Raabe, ω phase acts as a switch between dislocation channeling and joint twinning- and transformation-induced plasticity in a metastable β titanium alloy, Acta Mater. 151 (2018) 67–77. https://doi.org/10.1016/j.actamat.2018.03.053.

[166] Y. Zheng, R.E.A. Williams, D. Wang, R. Shi, S. Nag, P. Kami, J.M. Sosa, R. Banerjee, Y. Wang, H.L. Fraser, Role of ω phase in the formation of extremely refined intragranular α precipitates in metastable β-titanium alloys, Acta Mater. 103 (2016) 850–858. https://doi.org/10.1016/j.actamat.2015.11.020.

[167] Y. Zheng, D. Choudhuri, T. Alam, R.E.A. Williams, R. Banerjee, H.L. Fraser, The role of cuboidal ω precipitates on α precipitation in a Ti-20V alloy, Scr. Mater. 123 (2016) 81–85. https://doi.org/10.1016/j.scriptamat.2016.06.004.

[168] R. Shi, Y. Zheng, R. Banerjee, H.L. Fraser, Y. Wang, ω-Assisted α nucleation in a metastable β titanium alloy, Scr. Mater. 171 (2019) 62–66. https://doi.org/10.1016/j.scriptamat.2019.06.020.

[169] T. Li, D. Kent, G. Sha, H. Liu, S.G. Fries, A. V. Ceguerra, M.S. Dargusch, J.M. Cairney, Nucleation driving force for ω-assisted formation of α and associated ω morphology in β-Ti alloys, Scr. Mater. 155 (2018) 149–154. https://doi.org/10.1016/j.scriptamat.2018.06.039.

[170] O.C. Hellman, J.A. Vandenbroucke, J. Rüsing, D. Isheim, D.N. Seidman, Analysis of three-dimensional atom-probe data by the proximity histogram, Microsc. Microanal. 6 (2000) 437–444. https://doi.org/10.1007/s100050010051.

[171] J.D. Cotton, R.D. Briggs, R.R. Boyer, S. Tamirisakandala, P. Russo, N. Shchetnikov, J.C. Fanning, State of the Art in Beta Titanium Alloys for Airframe Applications, JOM 2015 676. 67 (2015) 1281–1303. https://doi.org/10.1007/S11837-015-1442-4.

[172] O.M. Ivasishin, P.E. Markovsky, Y. V. Matviychuk, S.L. Semiatin, C.H. Ward, S. Fox, A comparative study of the mechanical properties of high-strength β-titanium alloys, J. Alloys Compd. 457 (2008) 296–309. https://doi.org/10.1016/J.JALLCOM.2007.03.070.

[173] F. Sun, J.Y. Zhang, M. Marteleur, T. Gloriant, P. Vermaut, D. Laillé, P. Castany, C. Curfs, P.J. Jacques, F. Prima, Investigation of early stage deformation mechanisms in a metastable β titanium alloy showing combined twinning-induced plasticity and transformation-induced plasticity effects, Acta Mater. 61 (2013) 6406–6417. https://doi.org/10.1016/J.ACTAMAT.2013.07.019.

[174] S.A. Mantri, D. Choudhuri, T. Alam, V. Ageh, F. Sun, F. Prima, R. Banerjee, Change in the deformation mode resulting from beta-omega compositional partitioning in a TiMo alloy: Room versus elevated temperature, Scr. Mater. 130 (2017) 69–73. https://doi.org/10.1016/J.SCRIPTAMAT.2016.11.013.

[175] W. Wang, X. Zhang, J. Sun, Phase stability and tensile behavior of metastable β Ti-V-Fe and Ti-V-Fe-Al alloys, Mater. Charact. 142 (2018) 398–405. https://doi.org/10.1016/J.MATCHAR.2018.06.008.

[176] Q.Y. Sun, S.J. Song, R.H. Zhu, H.C. Gu, Toughening of titanium alloys by twinning and martensite transformation, J. Mater. Sci. 2002 3712. 37 (2002) 2543–2547. https://doi.org/10.1023/A:1015456026919.

[177] J. Gao, Y. Huang, D. Guan, A.J. Knowles, L. Ma, D. Dye, W.M. Rainforth, Deformation mechanisms in a metastable beta titanium twinning induced plasticity alloy with high yield strength and high strain hardening rate, Acta Mater. 152 (2018) 301–314. https://doi.org/10.1016/J.ACTAMAT.2018.04.035.

[178] N. Chen, H. Kou, Z. Wu, F. Qiang, C. Wang, J. Li, J.M. Molina-Aldareguia, Stress-induced α″ martensitic phase transformation and martensitic twinning in a metastable β titanium alloy, J. Alloys Compd. 859 (2021) 157809. https://doi.org/10.1016/J.JALLCOM.2020.157809.

[179] T.W. Duerig, G.T. Terlinde, J.C. Williams, Phase transformations and tensile properties of Ti-10V-2Fe-3AI, Metall. Trans. A 1980 1112. 11 (2013) 1987–1998. https://doi.org/10.1007/BF02655118.

[180] F. Sun, J.Y. Zhang, P. Vermaut, D. Choudhuri, T. Alam, S.A. Mantri, P. Svec, T. Gloriant, P.J. Jacques, R. Banerjee, F. Prima, Strengthening strategy for a ductile metastable β-titanium alloy using low-temperature aging, Http://Mc.Manuscriptcentral.Com/Tmrl. 5 (2017) 547–553. https://doi.org/10.1080/21663831.2017.1350211.

[181] S.A. Mantri, D. Choudhuri, T. Alam, G.B. Viswanathan, J.M. Sosa, H.L. Fraser, R. Banerjee, Tuning the scale of α precipitates in β-titanium alloys for achieving high strength, Scr. Mater. 154 (2018) 139–144. https://doi.org/10.1016/J.SCRIPTAMAT.2018.05.040.

[182] M.J. Lai, T. Li, F.K. Yan, J.S. Li, D. Raabe, Revisiting ω phase embrittlement in metastable β titanium alloys: Role of elemental partitioning, Scr. Mater. 193 (2021) 38–42. https://doi.org/10.1016/J.SCRIPTAMAT.2020.10.031.

[183] P.A. Kobryn, S.L. Semiatin, The laser additive manufacture of Ti-6Al-4V, JOM 2000 539. 53 (2001) 40–42. https://doi.org/10.1007/S11837-001-0068-X.

[184] L. Thijs, F. Verhaeghe, T. Craeghs, J. Van Humbeeck, J.P. Kruth, A study of the microstructural evolution during selective laser melting of Ti–6Al–4V, Acta Mater. 58 (2010) 3303–3312. https://doi.org/10.1016/J.ACTAMAT.2010.02.004.

[185] M. Simonelli, Y.Y. Tse, C. Tuck, Effect of the build orientation on the mechanical properties and fracture modes of SLM Ti–6Al–4V, Mater. Sci. Eng. A. 616 (2014) 1–11. https://doi.org/10.1016/J.MSEA.2014.07.086.

[186] H. Schwab, F. Palm, U. Kühn, J. Eckert, Microstructure and mechanical properties of the near-beta titanium alloy Ti-5553 processed by selective laser melting, Mater. Des. 105 (2016) 75–80. https://doi.org/10.1016/J.MATDES.2016.04.103.

[187] M.J. Bermingham, D. Kent, B. Pace, J.M. Cairney, M.S. Dargusch, High strength heat-treatable β-titanium alloy for additive manufacturing, Mater. Sci. Eng. A. 791 (2020) 139646. https://doi.org/10.1016/J.MSEA.2020.139646.

[188] T. DebRoy, H.L. Wei, J.S. Zuback, T. Mukherjee, J.W. Elmer, J.O. Milewski, A.M. Beese, A. Wilson-Heid, A. De, W. Zhang, Additive manufacturing of metallic components – Process, structure and properties, Prog. Mater. Sci. 92 (2018) 112–224. https://doi.org/10.1016/J.PMATSCI.2017.10.001.

[189] S.A. Mantri, T. Alam, Y. Zheng, J.C. Williams, R. Banerjee, Influence of post deposition annealing on microstructure and properties of laser additively manufactured titanium copper alloys, Addit. Manuf. 32 (2020) 101067. https://doi.org/10.1016/J.ADDMA.2020.101067.

[190] Z. Li, J. Li, Y. Zhu, X. Tian, H. Wang, Variant selection in laser melting deposited α + β titanium alloy, J. Alloys Compd. 661 (2016) 126–135. https://doi.org/10.1016/J.JALLCOM.2015.11.172.

[191] D. Zhang, D. Qiu, M.A. Gibson, Y. Zheng, H.L. Fraser, D.H. StJohn, M.A. Easton, Additive manufacturing of ultrafine-grained high-strength titanium alloys, Nat. 2019 5767785. 576 (2019) 91–95. https://doi.org/10.1038/s41586-019-1783-1.

[192] S. Neelakantan, D.S. Martin, P.E.J. Rivera-Díaz-del-Castillo, S. van der Zwaag, Plasticity induced transformation in a metastable β Ti-1023 alloy by controlled heat treatments, Http://Dx.Doi.Org/10.1179/174328408X385773. 25 (2013) 1351–1358. https://doi.org/10.1179/174328408X385773.

[193] Y. Danard, R. Poulain, M. Garcia, R. Guillou, D. Thiaudière, S. Mantri, R. Banerjee, F. Sun, F. Prima, Microstructure design and in-situ investigation of TRIP/TWIP effects in a forged dual-phase Ti–10V–2Fe–3Al alloy, Materialia. 8 (2019) 100507. https://doi.org/10.1016/J.MTLA.2019.100507.

[194] T. Akanuma, H. Matsumoto, S. Sato, A. Chiba, I. Inagaki, Y. Shirai, T. Maeda, Enhancement of athermal α″ martensitic transformation in Ti–10V–2Fe–3Al alloy due to high-speed hot deformation, Scr. Mater. 67 (2012) 21–24. https://doi.org/10.1016/J.SCRIPTAMAT.2012.03.011.

[195] L. Qi, X. Qiao, L. Huang, X. Huang, X. Zhao, Effect of structural stability on the stress induced martensitic transformation in Ti-10V-2Fe-3Al alloy, Mater. Sci. Eng. A. 756 (2019) 381–388. https://doi.org/10.1016/J.MSEA.2019.04.058.

[196] C. Qiu, Q. Liu, Multi-scale microstructural development and mechanical properties of a selectively laser melted beta titanium alloy, Addit. Manuf. 30 (2019) 100893. https://doi.org/10.1016/J.ADDMA.2019.100893.

[197] X. Ma, Z. Chen, L. Xiao, S. Luo, W. Lu, Stress-induced martensitic transformation in a β-solution treated Ti–10V–2Fe–3Al alloy during compressive deformation, Mater. Sci. Eng. A. 801 (2021) 140404. https://doi.org/10.1016/J.MSEA.2020.140404.

[198] X. Ma, Z. Chen, L. Xiao, W. Lu, S. Luo, Y. Mi, Compressive deformation of a metastable β titanium alloy undergoing a stress-induced martensitic transformation: The role of β grain size, Mater. Sci. Eng. A. 794 (2020) 139919. https://doi.org/10.1016/J.MSEA.2020.139919.

[199] T.W. Duerig, J. Albrecht, D. Richter, P. Fischer, Formation and reversion of stress induced martensite in Ti-10V-2Fe-3Al, Acta Metall. 30 (1982) 2161–2172. https://doi.org/10.1016/0001-6160(82)90137-7.

[200] A. Bhattacharjee, S. Bhargava, V.K. Varma, S. V. Kamat, A.K. Gogia, Effect of β grain size on stress induced martensitic transformation in β solution treated Ti–10V–2Fe–3Al alloy, Scr. Mater. 53 (2005) 195–200. https://doi.org/10.1016/J.SCRIPTAMAT.2005.03.039.

[201] A.W. Zhu, J. Chen, E.A. Starke Jr, Precipitation strengthening of stress-aged Al–xCu alloys, Acta Mater. 48 (2000) 2239–2246.

[202] X. Wang, J.D. Embury, W.J. Poole, S. Esmaeili, D.J. Lloyd, Precipitation strengthening of the aluminum alloy AA6111, Metall. Mater. Trans. A. 34 (2003) 2913–2924.

[203] T. Gladman, Precipitation hardening in metals, Mater. Sci. Technol. 15 (1999) 30–36. https://doi.org/10.1179/026708399773002782.

[204] L.N. Carter, C. Martin, P.J. Withers, M.M. Attallah, The influence of the laser scan strategy on grain structure and cracking behaviour in SLM powder-bed fabricated nickel superalloy, J. Alloys Compd. 615 (2014) 338–347. https://doi.org/https://doi.org/10.1016/j.jallcom.2014.06.172.

[205] T. Nagase, T. Hori, M. Todai, S.-H. Sun, T. Nakano, Additive manufacturing of dense components in beta-titanium alloys with crystallographic texture from a mixture of pure

metallic element powders, Mater. Des. 173 (2019) 107771. https://doi.org/https://doi.org/10.1016/j.matdes.2019.107771.

[206] M.J. Lai, T. Li, D. Raabe, ω phase acts as a switch between dislocation channeling and joint twinning- and transformation-induced plasticity in a metastable β titanium alloy, Acta Mater. 151 (2018) 67–77. https://doi.org/10.1016/J.ACTAMAT.2018.03.053.

[207] M.S.K.K.Y. Nartu, S. Dasari, A. Sharma, S.A. Mantri, S. Sharma, M. V. Pantawane, B. McWilliams, K. Cho, N.B. Dahotre, R. Banerjee, Omega versus alpha precipitation mediated by process parameters in additively manufactured high strength Ti–1Al–8V–5Fe alloy and its impact on mechanical properties, Mater. Sci. Eng. A. 821 (2021) 141627. https://doi.org/10.1016/J.MSEA.2021.141627.

[208] C. Li, J. Chen, Y.J. Ren, W. Li, J.J. He, J.H. Chen, Effect of solution heat treatment on the stress-induced martensite transformation in two new titanium alloys, J. Alloys Compd. 641 (2015) 192–200. https://doi.org/https://doi.org/10.1016/j.jallcom.2015.04.070.

[209] W. Chen, J. Zhang, S. Cao, Y. Pan, M. Huang, Q. Hu, Q. Sun, L. Xiao, J. Sun, Strong deformation anisotropies of ω-precipitates and strengthening mechanisms in Ti-10V-2Fe-3Al alloy micropillars: Precipitates shearing vs precipitates disordering, Acta Mater. 117 (2016) 68–80. https://doi.org/https://doi.org/10.1016/j.actamat.2016.06.065.

[210] Y. Fu, W. Xiao, D. Kent, M.S. Dargusch, J. Wang, X. Zhao, C. Ma, Ultrahigh strain hardening in a transformation-induced plasticity and twinning-induced plasticity titanium alloy, Scr. Mater. 187 (2020) 285–290. https://doi.org/https://doi.org/10.1016/j.scriptamat.2020.06.029.

[211] E. Bertrand, P. Castany, Y. Yang, E. Menou, T. Gloriant, Deformation twinning in the full-α″ martensitic Ti–25Ta–20Nb shape memory alloy, Acta Mater. 105 (2016) 94–103. https://doi.org/https://doi.org/10.1016/j.actamat.2015.12.001.

[212] P. Castany, Y. Yang, E. Bertrand, T. Gloriant, Reversion of a Parent ${130}{⟨310⟩}_{{\ensuremath{\alpha}}^{\ensuremath{'}\ensuremath{'}}}$ Martensitic Twinning System at the Origin of ${332}{⟨113⟩}_{\ensuremath{\beta}}$ Twins Observed in Metastable $\ensuremath{\beta}$ Titanium Alloys, Phys. Rev. Lett. 117 (2016) 245501. https://doi.org/10.1103/PhysRevLett.117.245501.

[213] Y. Yang, P. Castany, Y.L. Hao, T. Gloriant, Plastic deformation via hierarchical nano-sized martensitic twinning in the metastable β Ti-24Nb-4Zr-8Sn alloy, Acta Mater. 194 (2020) 27–39. https://doi.org/https://doi.org/10.1016/j.actamat.2020.04.021.

[214] S.A. Mantri, F. Sun, D. Choudhuri, T. Alam, B. Gwalani, F. Prima, R. Banerjee, Deformation Induced Hierarchical Twinning Coupled with Omega Transformation in a Metastable β-Ti Alloy, Sci. Rep. 9 (2019) 1334. https://doi.org/10.1038/s41598-018-37865-0.

[215] L. Lilensten, Y. Danard, C. Brozek, S. Mantri, P. Castany, T. Gloriant, P. Vermaut, F. Sun, R. Banerjee, F. Prima, On the heterogeneous nature of deformation in a strain-transformable beta metastable Ti-V-Cr-Al alloy, Acta Mater. 162 (2019) 268–276. https://doi.org/https://doi.org/10.1016/j.actamat.2018.10.003.

[216] Y.W. Chai, H.Y. Kim, H. Hosoda, S. Miyazaki, Self-accommodation in Ti–Nb shape memory alloys, Acta Mater. 57 (2009) 4054–4064. https://doi.org/https://doi.org/10.1016/j.actamat.2009.04.051.

[217] X. Ji, I. Gutierrez-Urrutia, S. Emura, T. Liu, T. Hara, X. Min, D. Ping, K. Tsuchiya, Twinning behavior of orthorhombic-α" martensite in a Ti-7.5Mo alloy, Sci. Technol. Adv. Mater. 20 (2019) 401–411. https://doi.org/10.1080/14686996.2019.1600201.

[218] Y.T. Zhu, X.Z. Liao, X.L. Wu, J. Narayan, Grain size effect on deformation twinning and detwinning, J. Mater. Sci. 48 (2013) 4467–4475. https://doi.org/10.1007/s10853-013-7140-0.

[219] A. Paradkar, S. V Kamat, A.K. Gogia, B.P. Kashyap, Trigger Stress for Stress-Induced Martensitic Transformation during Tensile Deformation in Ti-Al-Nb Alloys: Effect of Grain Size, Metall. Mater. Trans. A. 39 (2008) 551–558. https://doi.org/10.1007/s11661-007-9432-y.

[220] S. Sadeghpour, S.M. Abbasi, M. Morakabati, Deformation-induced martensitic transformation in a new metastable β titanium alloy, J. Alloys Compd. 650 (2015) 22–29. https://doi.org/https://doi.org/10.1016/j.jallcom.2015.07.263.

[221] M.-H. Cai, C.-Y. Lee, Y.-K. Lee, Effect of grain size on tensile properties of fine-grained metastable β titanium alloys fabricated by stress-induced martensite and its reverse transformations, Scr. Mater. 66 (2012) 606–609. https://doi.org/https://doi.org/10.1016/j.scriptamat.2012.01.015.

[222] B. Ellyson, J. Klemm-Toole, K. Clarke, R. Field, M. Kaufman, A. Clarke, Tuning the strength and ductility balance of a TRIP titanium alloy, Scr. Mater. 194 (2021) 113641. https://doi.org/https://doi.org/10.1016/j.scriptamat.2020.113641.

[223] S. Banerjee, U.M. Naik, Plastic instability in an omega forming Ti-15% Mo alloy, Acta Mater. 44 (1996) 3667–3677. https://doi.org/https://doi.org/10.1016/1359-6454(96)00012-2.

[224] S.A. Mantri, D. Choudhuri, A. Behera, M. Hendrickson, T. Alam, R. Banerjee, Role of isothermal omega phase precipitation on the mechanical behavior of a Ti-Mo-Al-Nb alloy, Mater. Sci. Eng. A. 767 (2019) 138397. https://doi.org/https://doi.org/10.1016/j.msea.2019.138397.